Alma Mater Studiorum – Università di Bologna

DOTTORATO DI RICERCA IN

Fisica

Ciclo XXX

Settore Concorsuale: 02/B1__________

Settore Scientifico Disciplinare: FIS/03____________

TITOLO TESI

Highlighting Charge Transfer Phenomena in Photo-catalytic Compounds Using Optical and X-ray Techniques

Presentata da: Giacomo Rossi

Coordinatore Dottorato **Supervisore**

Prof. Silvia Arcelli **Prof. Federico Boscherini**

Esame finale anno 2018

Per aspera ad astra

SUMMARY

ACKNOWLEDGEMENTS

Before discussing the results achieved during these last three years, I would like to thank all the people that I had the pleasure to work with. Among them, Professor Federico Boscherini is the person that mostly deserves my acknowledgements. He patiently followed all the steps of my PhD scholarship, teaching me how to perform research with an impact that matters. As well, I would like to thank Professor Luca Pasquini and all the PhD students in Bologna for the great support they gave me in these three years during which I learnt the fundamental value of teamwork. I would like to thank all the co-workers in Bologna not only for the precious teachings they gave me, but also and above all for the wonderful experiences we lived together.

I want also to thank all the coworkers from other institutions for the fundamental help they gave me, making possible the achievement of this important milestone in my educational and professional career. I want to mention the ISM group in Rome and the group of Professor Miotello in Trento for the contribution they gave in the characterization of the systems described below. Last, but not least, I want to thank Professor Majed Chergui and his research group for sharing their knowledge on dynamic phenomena during the amazing period that I spent in Lausanne.

ABSTRACT

The best way to obtain significant results in science is to combine sophisticated experimental techniques and innovative samples. The aim of this thesis is to report an operative method to be used for the characterization of charge transfer phenomena in photo-active samples. This kind of analysis is extremely important for the doped TiO_2 samples analyzed. These doped systems are promising photo-catalysts for hydrogen production from water splitting and pollutants degradation. Doping is an efficient method to decrease the energy needed to trigger the excitation of the photo-catalyst, otherwise possible only in the UV range. Identifying the role of dopants when the sample is excited is a mandatory step to understand the effects of dopants on the photo-catalytic properties of the systems. Both X-ray and optical techniques were used to characterize the samples and to follow those charge transfer phenomena induced by a visible excitation. Exploiting the unique characteristics of X Ray Absorption Fine Structure (XAFS) it was possible to determine the local structure of dopants inside the TiO_2 matrix. With a differential illumination High Resolution Fluorescence Detected (HERFD) XAFS experiment an atomistic description of the light-induced charge transfer phenomena in V-doped TiO_2 systems was obtained. The same physical process was also indirectly highlighted using optical ultrafast transient absorption spectroscopy. With this technique the inter-band transitions triggered by a visible light excitation were followed in real time. The combination of the two kinds of techniques made possible a complete description of the role of V dopants that, injecting charge carriers, lower the energy needed to trigger the photo-generation and surface trapping of charge carriers fundamental for the photo-catalytic processes.

REPORT OF ACTIVITIES

During my PhD scholarship I was mainly involved in projects focused on the application of sophisticated spectroscopic techniques to characterize a series of photo-active samples for energetic and environmental applications. In these three years I mainly learnt how to analyze XAFS spectra and obtain information about the local structure of single atomic species in a crystal structure. During the first year of my scholarship, I carried on the project started during my master thesis on metal phtalocyanines. The analysis of both EXAFS and XANES regions were performed using state of the art ab initio codes to simulate the near edge structure. All the results about this study were published in reference 1. The main project that I followed, however was focused on V and V-N co-doped TiO_2 samples. The studies performed on these systems are the subject of my PhD thesis. To determine the local structure of the two dopants inside the TiO_2 matrix two measurements sessions were performed. The first one, needed to measure the K edge absorption spectra of V and Ti cations was performed at the BM23 beamline of the ESRF in Grenoble (France). Soft X Ray measurements at N K edge, instead, were performed at the Bear beamline of the Italian synchrotron Elettra in Trieste (Italy). I analyzed all the XANES spectra collected comparing them with the theoretical ones simulated with FDMNES starting from models of the doped systems that I relaxed using Quantum ESPRESSO. The results obtained were published in references 2 and 3. After these first structural characterizations a differential illumination HERFD XANES experiment was performed in order to highlight charge transfer phenomena induced by a visible excitation of V-doped TiO_2 samples. The measurements were collected using the RIXS spectrometer of the ID26 beamline at the ESRF in Grenoble (France). Analyzing the measured differential spectra, it was possible to identify a clear charge exchange between V dopants and Ti cations. These results are already published in reference 4. At the same time, together with the ISM group in Rome I performed optical transient absorption spectroscopy measurements in order to follow the time evolution of inter-band transitions in doped and undoped TiO_2 samples in order to detect the effects of V doping. The results obtained are still unpublished.

During my PhD scholarship I spent six months at the EPFL (Switzerland), working in the group of Professor Majed Chergui. There, I performed ultrafast transient absorption spectroscopy measurements on Au-TiO_2 systems. The results of this study are still unpublished. During this period, however I was also involved in a time resolved XAFS experiment at the micro XAS beamline of the SLS synchrotron in Villigen (Switzerland). The aim of the experiment was to follow in real time charge exchange phenomena appearing after UV irradiation in inorganic perovskites samples for photovoltaic applications. The results of this experiment are reported in reference 5.

During the PhD scholarship I attended the school organized by the Italian Synchrotron Light Society (SILS) in Grado. During the first two years I also attended the following courses at the University of Bologna:

- Fisica dei Sistemi a Molti Corpi (Physics of Many-Body Sysems)
- Dispositivi e Materiali per la Fotonica (Devices and Materials for Photonics)

I participated also to several prestigious conferences and meetings presenting posters or oral contribution. Below the complete list is reported:

- 24th Congress and general assembly of the International Union of Crystallography, Hyderabad (India), August 2017. (oral contribution)
- European XFEL users' meeting and DESY photon science users' meeting 2017, Hamburg (Germany), January 2017 (poster).
- Material.it 2016, Catania (Italiy), December 2016. (oral contribution).
- Meeting of the Italian society of Synchrotron Light, Bari (Italy), September 2016 (oral contribution).
- European XFEL users' meeting and DESY photon science users' meeting 2016, Hamburg (Germany), January 2016 (poster).
- 16th International Conference on X-ray Absorption Fine Structure, Karlsruhe (Germany), August 2015 (poster).

LIST OF PUBLICATIONS

T. Baran, M. Fracchia, A. Vertova, E. Achilli, A. Naldoni, F. Malara, G. Rossi, S. Rondinini, P. Ghigna, A. Minguzzi and F. D'Acapito. "Operando and Time-Resolved X-Ray Absorption Spectroscopy for the Study of Photoelectrode Architectures." *Electrochimica Acta* 207 (2016): 16-21.

G. Rossi, M. Calizzi, V. Di Cintio, S. Magkos, L. Amidani, L. Pasquini, and F. Boscherini. "Local Structure of V Dopants in TiO2 Nanoparticles: X-ray Absorption Spectroscopy, Including Ab-Initio and Full Potential Simulations." *The Journal of Physical Chemistry C* 120.14 (2016): 7457-7466.

G. Rossi, F. d'Acapito, L. Amidani, F. Boscherini and M. Pedio. "Local environment of metal ions in phthalocyanines: K-edge X-ray absorption spectra." *Physical Chemistry Chemical Physics* 18.34 (2016): 23686-23694.

F. G. Santomauro, J. Grilj, L. Mewes, G. Nedelcu, S. Yakunin, T. Rossi, G. Capano, A. Al Haddad, J. Budarz, D. Kinschel, D. S. Ferreira, G. Rossi, M. Gutierrez Tovar, D. Grolimund, V. Samson, M. Nachtegaal, G. Smolentsev, M. V. Kovalenko, and M. Chergui. "Localized holes and delocalized electrons in photoexcited inorganic perovskites: Watching each atomic actor by picosecond X-ray absorption spectroscopy." *Structural Dynamics* 4.4 (2017): 044002.

G. Rossi, M. Calizzi, L. Amidani, A. Migliori, F. Boscherini and L. Pasquini. "Element-specific channels for the photoexcitation of V-doped TiO_2 nanoparticles." *Physical Review B* 96.4 (2017): 045303.

Z. El Koura, G. Rossi, M. Calizzi, L. Amidani, L. Pasquini, A. Miotello and F. Boscherini. "XANES study of Vanadium and Nitrogen dopants in photocatalytic TiO_2 thin films." *Physical Chemistry Chemical Physics*, 2017.

INTRODUCTION

A complete description of a physical phenomenon can be obtained only with a wise combination of advanced techniques. The experimental procedure itself is fundamental for the achievement of high impact results. In this thesis a deep analysis of different doped photo-catalytic compounds is reported focusing on the experimental techniques employed. The aim was to find the right procedure to observe and describe the effects of dopants on the host structure including those photo-induced charge transfer that are fundamental for photo-catalysis. In order to combine extremely good spatial and time resolutions both X ray and optical techniques were implied.

There are only a few techniques able to describe the local environment of low concentrated dopants in a host matrix. Among them, X-ray Absorption Fine Structure (XAFS)[6] is one of the most studied. Its unique characteristics like chemical selectivity are extremely important in several branches of material science. Several evolutions of this technique were developed in recent years thanks also to the improved brightness of synchrotron radiation sources. New and powerful experimental techniques like high energy resolution fluorescence detected (HERFD) XAFS[7] are now possible. The main advantage of this technique obtained combining X ray absorption and emission is the possibility to filter the fluorescence photons coming from the sample, selecting only those with an energy in a very narrow range. Below it will be clear that this peculiarity was extremely important for the characterization of the studied systems. The HERFD experiment described in this thesis is a further evolution designed to highlight the effects of a visible excitation on the atomic species composing the photo-catalyst. Using an exciting laser, it was possible to perform differential illumination measurements highlighting those changes induced in the local environment of dopants and host matrix cations.

X-ray techniques are surely the best candidates for an atomic description of functional materials, but in some cases, this is not the only information needed. Dealing with photo-active samples, optical measurements are also fundamental. Pump and probe experiments in this energy range are extremely powerful tools for the detection of inter-band transitions. Combining these results with those obtained in the X-ray experiments it is possible to obtain a comprehensive overview on the physical phenomena triggered by the visible excitation.

The studied photo-catalysts were V and V-N co-doped TiO_2 systems. TiO_2 is nowadays one of the most studied photo-catalysts for water splitting and decontamination.[8,9] TiO_2 is bio-compatible, abundant and not expensive. Those are three fundamental characteristics for large scale applications of this photo-catalyst. On the other hand, its efficiency is limited because its photo-catalytic properties can only be activated with UV radiation. The aim for the future is to find suitable solutions to increase the efficiency in the visible range. Among the various studied solutions doping is one of the most promising. It has been demonstrated that doping with transition metals and/or N is an efficient method to increase the absorption of TiO_2 in the visible range and consequently its photo-catalytic efficiency.[10] Some of the samples studied in this thesis were already tested highlighting an enhancement of the photo-catalytic efficiency due to the dopants incorporation.

1 METHODS

1.1 EXPERIMENTAL TECHNIQUES

In this section, the set of experimental techniques used to analyze several photo-active samples will be described. The aim is to give to the reader instruments to understand the final chapters were the experimental results are shown. For each technique, the exploited physical concepts and the potential applications will be highlighted.

All the described methods are part of the more general category of absorption spectroscopies. Some of them, like Resonant Inelastic X-Ray Scattering (RIXS) are innovative techniques obtained combining absorption and emission spectroscopies. The base of all absorption spectroscopy techniques is the study of variation of the absorption coefficient μ as a function of the incident photon energy. In general, when a radiation beam passes through a physical medium there is an attenuation that follows the Lambert-Beer's law expressed in eq. 1.1, where I indicates the beam intensity, x the sample thickness and I_0 the impinging beam intensity.

$$I(x,E) = I_0 e^{-\mu(E)x} \tag{1.1}$$

The absorption coefficient can be defined using equation 1.2 where ρ_i are the element densities and σ_i are sum of the scattering and absorption cross sections.

$$\mu = \sum_i \sigma_i \rho_i \tag{1.2}$$

Changing the energy of the incident photons it is possible to trigger different phenomena. For example, using visible radiation it is possible to activate inter-band transitions while for higher energies in the X-Ray regime it is possible to excite the electrons from the core levels. This wide range of physical phenomena reflected in the absorption coefficient lead to the development of several different experimental techniques, each one focused on the detection of specific photo-induced dynamics or processes.

1.1.1 X RAY ABSORPTION FINE STRUCTURE (XAFS)

Among the various techniques based on X-Rays, absorption spectroscopy is one of the few that can provide information about the local environment surrounding a selected element. Chemical selectivity is fundamental for several studies, especially when doped materials are involved. For low dopant concentrations, standard techniques like X Ray diffraction (XRD) cannot provide any information about the structural changes induced by the doping process and above all, no information can be obtained about the chemical and electronic environment surrounding the dopants.

XAFS as well as the other absorption spectroscopies is based on the study of the absorption coefficient μ. In the X-rays regime, the scattering cross section is several orders of magnitude lower than the absorption one. For this reason, μ can be considered directly proportional to the absorption cross section. In general, for wide energy intervals the behavior of the absorption coefficient can be approximated using eq. 1.3 where Z is the atomic number of the target atom, m its mass, d the sample density and E the photon energy.[11]

$$\mu(E) \approx \frac{dZ^4}{mE^3} \tag{1.3}$$

This trend can be considered only an approximation because of the presence of several discontinuities, the absorption edges, appearing when the photon energy becomes high enough to trigger electronic transitions from one of the core levels to the continuum. When this happens, there is a clear enhancement of the number of absorbed photons and a consequent fast rising of the absorption coefficient. In Figure 1.1 the typical shape of an absorption edge of Vanadium is shown. This feature appears when the energy needed to trigger the excitation of the K shell electrons is reached. The most interesting detail in this image, however is not the discontinuity itself, but the series of oscillations appearing in the energy range above the edge. These features of the absorption spectrum are called X Ray Absorption Fine Structure (XAFS). In the next paragraphs, it will be shown how from XAFS it is possible to obtain a significant quantity of information about the local structure and chemical environment surrounding the absorbing atom.

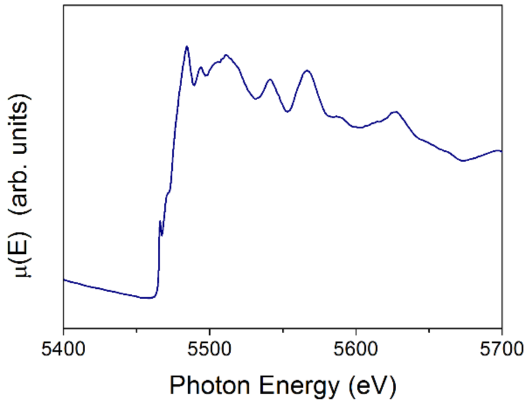

Figure 1.1: Typical X-ray absorption spectrum: the case of metallic V at the V K edge

1.1.1.1 THE ORIGIN OF XAFS AND THE EXAFS FORMULA

The modern interpretation of XAFS is mainly based on the physical mechanism described in the '70s by Stern, Sayers and Lytle.[6] They elaborated an original model that correlated oscillations in the region from 100 to 1000 eV above the absorption edge usually called Extended X-Ray absorption Fine Structure (EXAFS), to the local structure surrounding the absorbing atom. The oscillating features on the section of the absorption spectrum extending around the absorption edge (from 0 to 50-100 eV above the edge) were called X Ray Absorption Near Edge Structure (XANES) or Near Edge X-Ray Absorption Fine Structure (NEXAFS). Later it will be clear that the physical phenomenon behind the origin of both EXAFS and XANES is the same, but thanks to several approximations which can be made the description of the former one is simpler. For this reason, efficient methods for *ab-initio* simulation of XANES spectra appeared only in these last few years, thanks also to the constant improvement of computer performance power. Another very important region of the absorption spectrum is the pre-edge. Features appearing at energies below the main absorption edges are related to transitions of the core electrons to unoccupied bound levels. For this reason, the pre-edge region is fundamental to understand the chemical environment around the absorber.

XAFS is nowadays a well-established technique and the physics mechanism behind it is well described in several books and articles.[6,11–17] From a phenomenological point of view the origin of XAFS is an interference phenomenon. In Figure 1.2 a schematic description of the mechanism mentioned above is reported. First, X-ray photons interact with the core electrons of the absorbing atom. It is good to remember that it is possible to tune the X-ray wavelength to excite the core electrons of a single atomic species. In the case shown in Figure 1.2, the energy is tuned to excite only the core electrons of the element labelled in green. If the photon energy is greater than the binding energy the core electrons can propagate as waves through the crystal structure until they reach the surrounding atoms where they are scattered. The superposition of the propagating and scattered electron wave-functions generates an interference pattern that changes the probability to excite the core electron of the absorber atom with other incoming X-ray photons. These small but visible changes are reflected in the absorption spectrum and the resulting effect is the X ray absorption fine structure.

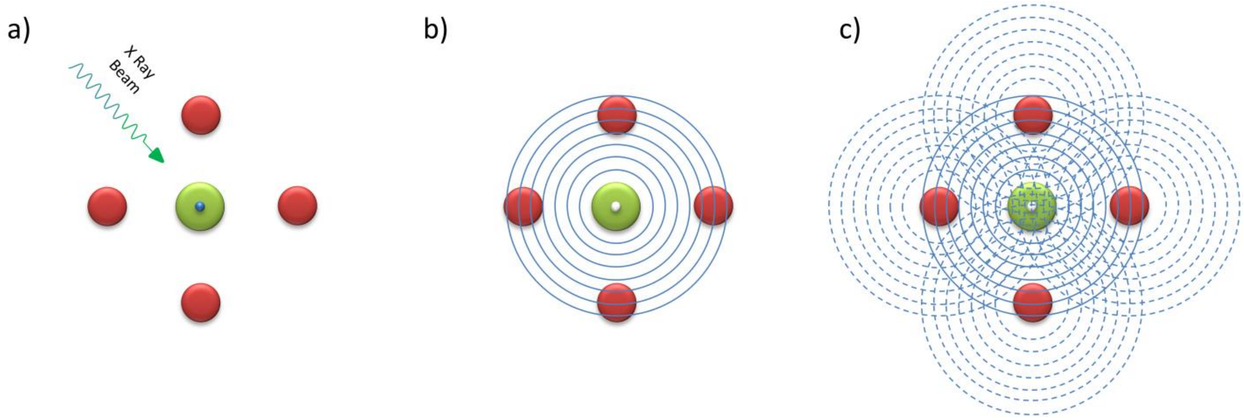

Figure 1.2: Phenomenological origin of XAFS. a) the X ray beam excites one of the core electrons of the green atom. b) the excited photoelectron starts propagating as a wave until it reaches the atoms surrounding the absorber. c) The propagating electron wave is scattered creating an interference pattern that is extended also in the center of the absorber atom where core electrons are located. This interference process gives rise to modulations of the absorption coefficient.

This phenomenological introduction is very useful to follow the steps of the more rigorous and quantitative description that will lead to the calculation of the standard EXAFS formula. Before starting, it is useful to define rigorously EXAFS. If $\mu(E)$ is the recorded absorption spectrum, $\mu_0(E)$ the spectrum that the absorber atom will produce if isolated (no surrounding atomic structure that means no oscillations) and $\Delta\mu_0$ the amplitude of the discontinuity jump near the absorption edge, XAFS is defined using eq. 1.4.

$$\chi(E) = \frac{\mu(E) - \mu_0(E)}{\Delta\mu_0} \qquad 1.4$$

The first approximation needed to easily carry on the calculations is the one electron approximation. It means that only one of the electrons in the core levels interacts with the incoming photon. Before the excitation this electron is in its orbital indicated as $|\psi_i\rangle$ characterized by a certain energy E_i. When the X-ray photon with energy $E_{ph} = \hbar\omega$ arrives, it is absorbed by the electron that undergoes to a transition to a final state $|\psi_f\rangle$ characterized by a final energy $E_f = E_i + \hbar\omega$. The transition rate w_{fi}, directly proportional to the absorption cross section and consequently to the absorption coefficient, can be calculated using Fermi's golden rule expressed in eq. 1.5 where $|M_{fi}|$, the transition matrix element is the quantity defined in equation 1.6 and $\rho(E_f)$, the density of final states. In eq. 1.6, V_{int} represents the interaction Hamiltonian associated to the electron-photon interaction.

$$w_{fi} = \frac{2\pi}{\hbar}|M_{fi}|^2\rho(E_f) \qquad 1.5$$

$$M_{fi} = \langle\psi_f|V_{int}|\psi_i\rangle = \int \psi_f^*(\boldsymbol{x})V_{int}(\boldsymbol{x},\boldsymbol{t})\psi_i(\boldsymbol{x})d^3\boldsymbol{x} \qquad 1.6$$

It will be soon clear that the physical origin of XAFS is mainly related to the matrix element M_{fi}. To estimate the integral in eq. (1.6) it is necessary to evaluate the ground and excited electronic states $|\psi_i\rangle$ and $|\psi_f\rangle$ and the interaction potential V_{int} that, as indicated, is time dependent. The starting point of this calculation is the Hamiltonian of a single electron in the Coulomb atomic potential (eq. 1.7).

$$H = \frac{\boldsymbol{p}^2}{2m} + V(\boldsymbol{r}) \qquad 1.7$$

The final state $|\psi_f\rangle$ can be evaluated finding the eigenstates of the Hamiltonian obtained perturbing 1.7 to take in account the electro-magnetic field of the X-ray photon. This can be done using the minimal coupling formalism. All the calculations are performed using a semi-classical approach considering a classical description of the electro-magnetic wave acting on quantic atoms. The Hamiltonian 1.7 is modified using transformations 1.8, where $\boldsymbol{A}(\boldsymbol{r},t)$ and $\phi(\boldsymbol{r},t)$ are respectively the vector and scalar electromagnetic potentials.

$$\begin{aligned} \boldsymbol{p} &\rightarrow \boldsymbol{p} - q\boldsymbol{A}(\boldsymbol{r},t) \\ V(\boldsymbol{r}) &\rightarrow V + q\phi(\boldsymbol{r},t) \end{aligned} \qquad 1.8$$

The resulting Hamiltonian is shown in equation 1.9. The generic charge q is substituted by the electron charge -e.

$$H = \frac{1}{2m}\left(\boldsymbol{p} + e\boldsymbol{A}(\boldsymbol{r},t)\right)^2 + V(\boldsymbol{r}) - e\phi(\boldsymbol{r},t) \qquad 1.9$$

Since X-rays can be described as propagating waves it is possible to apply the radiation gauge (eq. 1.10)

$$\phi = 0 \qquad \nabla \cdot \boldsymbol{A}(\boldsymbol{r}, t) = 0 \tag{1.10}$$

The first reasonable approximation is to consider a monochromatic X-Ray beam. This implies that the vector potential can be expressed in the easiest approximation as a propagating plane wave as shown in eq. 1.11

$$\boldsymbol{A}(\boldsymbol{r}, t) = \boldsymbol{A}_0 e^{i(\boldsymbol{k}\cdot\boldsymbol{r} - \omega t)} + c.c. \tag{1.11}$$

The scalar product $\boldsymbol{k} \cdot \boldsymbol{r}$, considering core electrons is enough small to expand in series the exponential as shown in equation 1.12

$$e^{i\boldsymbol{k}\cdot\boldsymbol{r}} = 1 + i\boldsymbol{k} \cdot \boldsymbol{r} - \frac{(\boldsymbol{k} \cdot \boldsymbol{r})^2}{2!} + \cdots \cong 1 \tag{1.12}$$

This series can mostly be truncated at the first order, this is the electric dipole approximation. Sometimes also the second order term is relevant, especially in the pre-edge and XANES regions, where quadrupole contributions are not always negligible. In this approach, it can be shown that the perturbed Hamiltonian can be approximated as shown below:

$$H = \frac{\boldsymbol{p}^2}{2m} + V(\boldsymbol{r}) - e\boldsymbol{r} \cdot \boldsymbol{E}(t) = H_0 - (\boldsymbol{r} \cdot \hat{\eta})\, E(t) \tag{1.13}$$

The perturbing potential is therefore proportional to the scalar product between the position vector $\boldsymbol{r}$ and the electric field polarization $\hat{\eta}$. Substituting this in equation 1.5 and considering the direct proportionality between w_{fi} and μ it is possible to obtain equation 1.14 in which the wave-functions of the N-1 non-interacting electrons are included. Since only linearly polarized X-rays are used in this work $\hat{\eta}$ is constant.

$$\mu(\omega) \propto \left|\langle \Psi_f^{N-1} \psi_f | \hat{\eta} \cdot \boldsymbol{r} | \psi_i \Psi_i^{N-1} \rangle\right|^2 \rho(E_f) \tag{1.14}$$

The contribution of the non-interacting electrons, factorizing the starting and final wavefunctions, can be considered as a multiplicative parameter called S_0^2 defined in equation 1.15. The value of this factor if the other electrons are not absorbing is 1.

$$S_0^2 = \left|\langle \Psi_f^{N-1} | \Psi_i^{N-1} \rangle\right|^2 \cong 1 \tag{1.15}$$

Substituting 1.15 in 1.14 the absorption coefficient equation becomes 1.16

$$\mu(\omega) \propto S_0^2 \left|\langle \psi_f | \hat{\eta} \cdot \boldsymbol{r} | \psi_i \rangle\right|^2 \rho(E_f) \tag{1.16}$$

The dependence of the absorption coefficient from the energy of the incoming X-Ray photon is all described in equation 1.16. The origin of the XAFS oscillations must be related to changes in the final state $|\psi_f\rangle$, since no oscillating part is introduced by the interaction potential.

The ground state $|\psi_i\rangle$ neglecting electron-electron interactions can be calculated as eigenstate of the Hamiltonian 1.7, but the final state $|\psi_f\rangle$ can be very hard to calculate. In the easiest case the core electron is excited to one of the unoccupied bound levels so, $|\psi_f\rangle$, can be described as an atomic orbital, like the ground state. These transitions obey to a series of laws called selection rules. For symmetry reasons, the matrix element and consequently the transition probability are 0 for all the transitions between bound levels that do not follow equations 1.17, where l and m are the electronic orbital angular momentum and its projection on the z axis.

$$\Delta l = \pm 1 \qquad \Delta m = 0 \tag{1.17}$$

When the electron transition is from one of the core levels to the continuum the final state calculation is not trivial. For high energy photo-electrons some reasonable approximations can be made leading to the standard EXAFS formula. The first step to simplify calculations, is to redefine all the quantities in the previous formulas as functions of the electron wave-vector $\boldsymbol{k}$ the modulus of which is defined in a free electron approximation, in equation 1.18, where m_e is the electron mass, E_0, the absolute value of its binding energy and E the incident photon energy.

$$k = \sqrt{\frac{2m_e}{\hbar}(E - E_0)} \tag{1.18}$$

The final state for the excited core electrons, if the photon energy is enough to promote the transition to the continuum is an outgoing wave with energy $E_f = E + E_i$. In case of a non-isolated atom, a small perturbative contribution due to scattered photoelectrons must be added to the propagating wave. The absorption coefficient can always be evaluated using 1.16, but in this last case the final state $|\psi_f\rangle$ is defined as shown in equation 1.19 where $|\psi_f^0\rangle$ is the unperturbed final state of an isolated atom and Δ the small perturbation due to the backscattered electrons.

$$|\psi_f\rangle = (1 + \Delta)\,|\psi_f^0\rangle \tag{1.19}$$

Substituting equation 1.19 in the XAFS definition (equation 1.4) and neglecting all the terms containing Δ^2 it is possibl0e to write the explicit form of the XAFS equation (eq. 1.20)

$$\chi(k) = \frac{\mu(k) - \mu_0(k)}{\mu_0(k)} = 2\ \mathrm{Re}\,\{\Delta\} \tag{1.20}$$

A way to calculate Δ and consequently $\chi(k)$ is based on the muffin-tin approximation. This kind of approximation is quite good if the photo-electron propagating outside the atom has enough energy to not be affected by the non-spherical shape of the real atomic potential. This happens only in the EXAFS region, so for the interpretation of XANES in many cases this model is not accurate enough and it is necessary to use the full atomic potential that however is more complex and computationally demanding. The muffin tin model, assumes a low range Coulomb potential centered in the various atomic sites surrounded by an inter-atomic region where the potential is constant (null for easier calculations). In Figure 1.3 a cartoon picture of such a potential is shown. With the roman numbers I, II and III are indicated three main regions that will be very useful for the evaluation of the final state $|\psi_f\rangle$ in a single scattering approximation.

The simple derivation illustrated in the following lines has the aim of showing the physical origin of the oscillating behavior of $\chi(k)$. The $|\psi_f^0\rangle$ wavefunction in region I can be very complex, but since the absorption coefficient is related to the matrix element between the final state and the localized core level only the behavior at r around 0 is relevant. Because of the selection rules the final state will have an angular momentum $l = 1$ if the starting core level is the 1s. The radial part of this p orbital can be described using the spherical Bessel function j_1 shown in equation 1.21

$$j_1(kr) = \frac{\sin(kr)}{kr} - \frac{\cos(kr)}{(kr)^2} \qquad 1.21$$

The behavior of j_1 near the origin can be approximated with $kr/3$ that is the limit for small r values of 1.21.

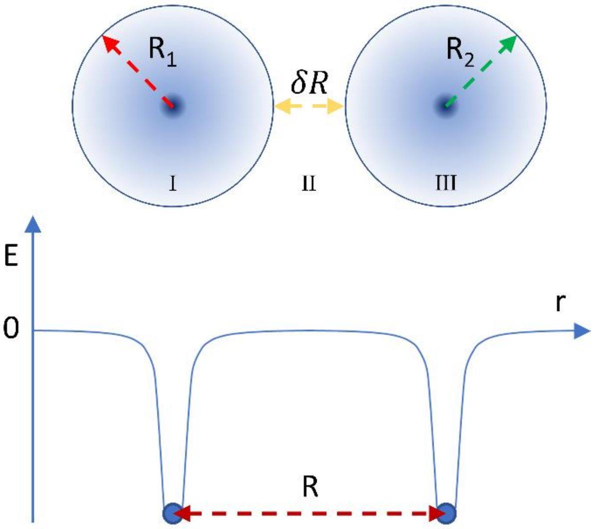

Figure 1.3: Schematic description of the Muffin thin potential. The Coulomb Potential is limited in the two spherical regions I and III, while in region II is null.

In region II the radial part of the wavefunction will be described as the superposition of an incoming and an outgoing wave as shown in equation 1.31

$$\psi_{II}(r) = \frac{1}{kr}\left[e^{-i\left(kr-\frac{\pi}{2}\right)} + \Phi' e^{i\left(kr-\frac{\pi}{2}\right)}\right] \qquad 1.22$$

The term Φ' must match $\psi_I(r)$ and $\psi_{II}(r)$, because no discontinuity can appear at the interface between region I and II. Since in the transition between region I and II the probability to find the propagating electron must be conserved the coefficient Φ' must have a unit modulus. This means that this parameter act as a dephasing coefficient. Without scattering atoms surrounding the absorber equation 1.31 is simplified to a propagating wave. Considering also the angular dependence, the representation in spherical coordinates of the unperturbed wavefunction $\left|\psi_f^0\right\rangle$ can be written as

$$\langle r,\theta,\phi|\psi_f^0\rangle = \psi_{II}^0(\boldsymbol{r}) = \frac{\sqrt{3}}{4\pi}\cos\theta\,\frac{1}{kr}\Phi e^{ikr} \qquad 1.23$$

where Φ is equal to $-i\Phi'$.

The scattered wavefunction generating the incoming wave in equation 1.22 can be derived using a standard formalism with the reasonable assumption of a point like scattering atom. Defining $\boldsymbol{r}_j$ as the interatomic vector, $\psi_{sc}(\boldsymbol{r})$ can be written as:

$$\psi_{sc}(\boldsymbol{r}) = \psi_{II}(\boldsymbol{r})f(k,r_j,\alpha)\frac{e^{ik|\boldsymbol{r}-\boldsymbol{r}_j|}}{k|\boldsymbol{r}-\boldsymbol{r}_j|} \qquad 1.24$$

where $f(k,r_j,\alpha)$ is the scattering amplitude depending on the momentum k, the distance r_j and the scattering angle α. To better understand the situation in Figure 1.4 a simple sketch is shown.

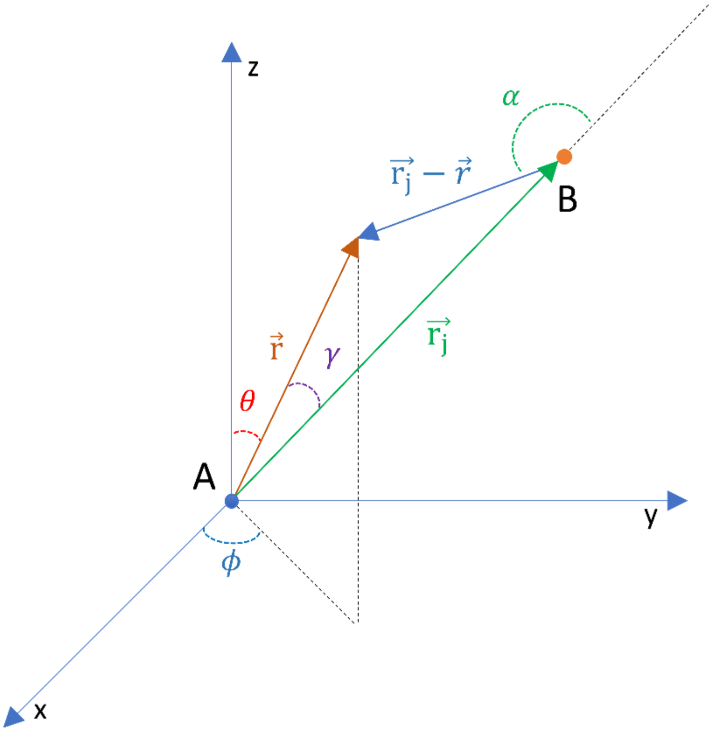

Figure 1.4: Schematic description of the single scattering phenomenon. A and B are respectively the Absorber and the scattering atom

The last multiplicative term in the r.h.s of equation 1.24 is the typical expression of a spherical wave centered in B. Since only the part of the scattered wave with the same angular dependence and the same limit for $r \to 0$ as the unperturbed wavefunction $|\psi_f^0\rangle$ will gives rise to relevant contributions generating the fine structure, the strategy is to calculate a factor C such that:

$$\lim_{r\to 0}\psi_{sc}(\boldsymbol{r}) = \frac{C\sqrt{3}}{4\pi}\cos\theta\frac{kr}{3}\Phi \tag{1.25}$$

For small $\boldsymbol{r}$ values the quantity $\left|\boldsymbol{r}-\boldsymbol{r_j}\right|$ can be approximated as shown in equation 1.26

$$\left|\boldsymbol{r}-\boldsymbol{r_j}\right| \approx r_j - r\cos\gamma \tag{1.26}$$

The spherical wave term for small r and $kr_j \gg 1$ becomes:

$$\frac{e^{ik|r-r_j|}}{k\left|\boldsymbol{r}-\boldsymbol{r_j}\right|} \approx \frac{e^{ikr_j}}{kr_j}\left[1+\left(\frac{1}{kr_j}-i\right)kr\cos\gamma\right] \approx \frac{e^{ikr_j}}{kr_j}\left[1-ikr\cos\gamma\right] \tag{1.27}$$

Writing $\cos\gamma$ as a function of θ and θ_j it is possible to identify the portion of scattered wavefunction having the behavior described in equation 1.25. The value of the C factor obtained at the end of the calculation is reported in equation 1.28.

$$C(k,r_j,\theta_j) = -3i\frac{e^{2ikr_j}}{k^2r_j^2}\cos^2\theta_j\, f(k,r_j,\pi) \tag{1.28}$$

To take in account the effects of the absorbers' potential on the scattered wave, C must be multiplied by a phase shift term $e^{2i\delta_1}$. For small r values (where the starting core levels are localized) the final wavefunction obtained adding the outgoing unperturbed wavefunction and the incoming scattered wave is described in equation 1.29 from which it is possible to derive the value of the Δ factor defined in equation 1.19.

$$\left|\psi_f\right\rangle = \left(1+Ce^{2i\delta_1}\right)\left|\psi_f^0\right\rangle = (1+\Delta)\left|\psi_f^0\right\rangle \tag{1.29}$$

The fine structure $\chi(k)$ can be easily derived substituting the value of Δ in equation 1.20 obtaining:

$$\chi(k) = 2\,\mathrm{Re}\,\{\Delta\} = 3\cos^2\theta_j\,\mathrm{Im}\left\{\frac{e^{2ikr_j}}{k^2r_j^2}f(k,r_j,\pi)e^{i2\delta_1}\right\} \tag{1.30}$$

Approximating the wave impinging on the scattering atom as a plane wave it is possible to remove the dependence of the scattering amplitude from r_j and express f as shown in equation 1.31.

$$f = |f(k,\pi)|e^{i\phi} \tag{1.31}$$

With approximation 1.31 it is possible to write the standard EXAFS formula (equation 1.32)

$$\chi(k) = \frac{3\cos^2\theta_j}{k^2r^2}|f(k,\pi)|\sin\left[2kr_j+\phi+2\delta_1\right] \tag{1.32}$$

For randomly oriented powder samples or amorphous materials the average value of $3\cos^2\theta_j$ is equal to 1, so the fine structure does not depend anymore on the angle θ_j.

The generalization of equation 1.38 to the case of several nearest neighbors is immediate and it is given by the summation of all the contributions coming from the atoms at distance R_i obtaining equation 1.33, where N_i indicates the degeneracy of the i^{th} single scattering path. The dephasing contributions are resumed for simplicity in the $\phi_i(k)$ terms.

$$\chi(k) = \sum_i 3N_i(\hat{\eta} \cdot \boldsymbol{R_i})^2 \frac{1}{kR_i^2} |f(k,\pi)| \sin\big(2kR_i + \phi_i(k)\big) \qquad 1.33$$

This formula, however needs some changes to take in account several important physical effects like disorder, multiple scattering and inelastic processes.

Inelastic processes introduce two multiplicative factors. The first one, S_0^2, was previously defined as the contribution of the non- interacting electrons while the second one is a decreasing exponential factor $e^{-\frac{R_i}{\lambda}}$ related to the mean free path of the photoelectron. Without inelastic scattering processes the mean free path is the distance that the photo-electron can travel before the core-hole excitation decays as shown in equation 1.34 where v is the photo-electron velocity and τ_u the core-hole life-time

$$\lambda_u = v \cdot \tau_u \qquad 1.34$$

However, the mean free path is limited also by the energy losses due to inelastic scattering processes. The mean free path in this case, indicated as λ_e, is quite difficult to quantify. Since both contributions (core-hole and inelastic dumping) are relevant it is necessary to define a parameter λ (a function of $\lambda_e$and λ_u) describing the actual value of the mean free path (equation 1.35).

$$\frac{1}{\lambda} = \frac{1}{\lambda_u} + \frac{1}{\lambda_e} \qquad 1.35$$

It is easy to understand that longer scattering paths are thus less probable and, consequently they give a lower contribution to the EXAFS signal. Considering inelastic contributions the standard EXAFS equation is 1.36

$$\chi(k) = S_0^2 \sum_i 3N_i(\hat{\eta} \cdot \boldsymbol{R_i})^2 \frac{1}{kR_i^2} e^{-\frac{2R_j}{\lambda}} |f(k,\pi)| \sin\big(2kR_i + \phi_i(k)\big) \qquad 1.36$$

As mentioned before, not only single scattering contributions are relevant to correctly reproduce the EXAFS signal. The photo-electron can be scattered by several atoms before coming back to the absorber center. The absorption coefficient can be expressed as the sum of a series of contributions as shown in equation 1.37, where the subscripts indicate the number of scattering processes that the photo-electron undergoes before going back to the absorber.

$$\mu(k) = \mu_0(1 + \chi_1(k) + \chi_2(k) + \chi_3(k) + \cdots) \qquad 1.37$$

In the EXAFS region, this series is strongly converging (this is not true for XANES region), so it is possible to reproduce quite well the experimental signal considering only the first two or three $\chi_i$terms, neglecting all the paths involving a higher number of scattering processes. Each

χ_i function can be expressed as shown in equation 1.38, where $\{\boldsymbol{r}_i\}$ are the partial distances composing the multiple scattering path and R_i the total path length. A and ϕ depend on the potentials of the atoms involved in the multiple scattering process.

$$\chi_i(k) = A_i(k, \boldsymbol{r}_i)\sin\big(kR_i + \phi_i(k, \boldsymbol{r}_i)\big) \qquad 1.38$$

As mentioned before, it is necessary to take in account also the contributions related to the structural disorder. Oscillations of the atoms around their equilibrium positions, can modify the interference phenomenon generating EXAFS. Small oscillations of the crystal structure, slightly distorting the local structure, can lower the effects of constructive or destructive interferences. The result is a smoother XAFS spectrum with lower features. In the standard EXAFS formula, the disorder contribution is represented by the so-called Debye Waller factors σ_i^2 that represent the mean square fluctuation of the scattering path lengths. The decreasing exponential term $e^{-k^2\sigma_i^2}$ strongly damps EXAFS oscillations when σ_i or k are too high and since σ_i^2 increases with the temperature, it is sometimes needed to cool down the sample to have an acceptable signal. The final form of the standard EXAFS formula can be expressed as shown in equation 1.39.

$$\chi(k) = S_0^2 \sum_i 3N_i(\hat{\eta}\cdot\boldsymbol{R}_i)^2 \frac{1}{kR_i^2} e^{-\left(\frac{2R_i}{\lambda}+2k^2\sigma_i^2\right)} |f(k,\alpha_i)| \sin\big(2kR_i + \phi_i(k)\big) \qquad 1.39$$

Since the EXAFS signal can be expressed as the sum of sinusoidal functions depending by the path half-lengths R_i, its Fourier transform in the radial distances space is a series of peaks centered in values related to the inter-atomic distances. An example is shown in Figure 1.5 where Fourier transforms of V and V_2O_4 are compared. Without performing a complete analysis with *ab initio* codes, starting from equation 1.39 it is possible to extrapolate some information. For example, it is immediately visible that V-V bonds in the V foil are longer than the V-O bonds in V_2O_4. This because the most intense peak at low R values, related to the first correlation shell less affected by inelastic effects, is centered at a lower position for the oxide. This is of course confirmed by crystallographic data[18] that shows a V-V distance of around 2.62 Å wider than the average V-O distance in V_2O_4 that is around 1.90 Å.

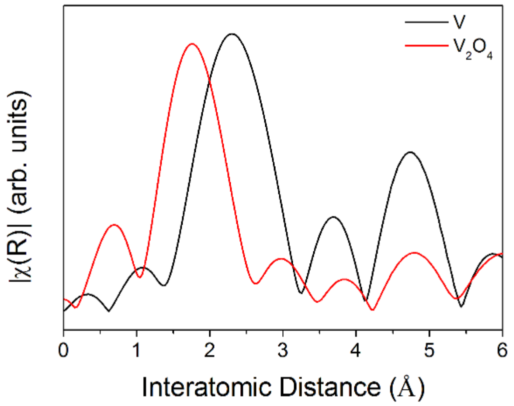

Figure 1.5: Comparison between the Fourier transform of the $\chi(k)$ signals of V (black curve) and V_2O_4 (red curve)

1.1.1.2 PHENOMENOLOGICAL INTRODUCTION TO XANES

The aim of this paragraph is to show how XANES spectra can provide crucial information about the studied systems also without any theoretical calculation. Some of the spectral features appearing near the absorption edge are strictly related to the chemical environment surrounding the absorber. Later in this work edge shifts and changes in the pre-edge features will play a key role in data interpretation, so a brief description of the physics behind these phenomena is required to fully understand the results obtained.

THE PRE-EDGE

In Paragraph 1.1.1.1 above, discussing the origin of XAFS, pre-edge features were related to dipole and quadrupole transitions from core levels to unoccupied bound states. These peaks are of great importance in the study of transition metals oxides because of their extreme sensitivity to local structure and symmetry changes. In Figure 1.6 the pre-edge features of TiO_2 anatase and rutile and $FeTiO_3$ ilmenite are shown. In all the three cases Ti is in a 4+ oxidation state and the surrounding oxygens are placed in the vertexes of distorted octahedrons. The three local structures are very similar, but bond lengths and angles are enough different to produce significant changes in the pre-edge structure.

When the local symmetry changes more significantly, the effects on pre-edge can be even more dramatic. For example an interesting study performed by Wong et al.[19] on Vanadium oxides highlights the correlation between the presence of an inversion center and the amplitude of the pre-edge peaks. This kind of correlation between local symmetry and amplitudes of the pre-edge features is valid also for the other transition metals as shown in reference [20].

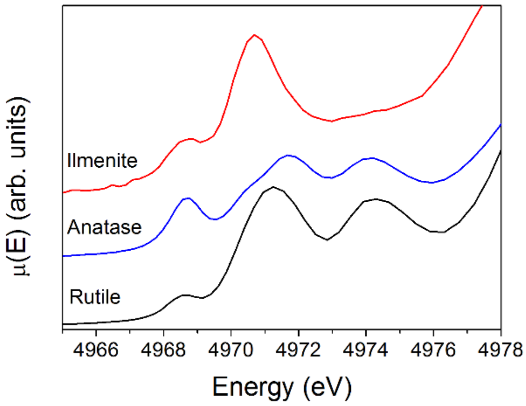

Figure 1.6: Comparison between the pre-edges of TiO2 (Anatase and Rutile) and FeTiO3 (ilmenite)

Considering the three most abundant V oxides (V_2O_3, V_2O_4 and V_2O_5) it is possible to see that the local structure surrounding V changes significantly, increasing the V oxidation state. In V_2O_3, V^{3+} cations are in the center of slightly distorted oxygen octahedrons. This structure showing only two possible lengths for the six V-O bonds is still a quite regular octahedron. In V_2O_4, V^{4+} cations are surrounded by even more distorted oxygen octahedrons showing six different V-O bond lengths. The local structure of V_2O_5, instead, is completely different. V^{5+} cations are placed at the center of a distorted square based oxygen pyramid. In Table 1.1 are listed some relevant structural parameters of these three compounds obtained from the literature[19].

Table 1.1: Relevant structural parameters for three of the main abundant V oxides. Values are obtained from reference [19]

Compound	Formal V Valence	Number of Bonds	Bond Lengths
V_2O_3	3+	6	3 x 1.96 Å 3 x 2.06 Å
V_2O_4	4+	6	1.76 Å 1.86 Å 1.87 Å 2.01 Å 2.03 Å 2.05 Å
V_2O_5	5+	5	1.585 Å 1.780 Å 2 x 1.878 Å 2.021 Å

In Figure 1.7 the comparison of pre-edge peak intensity for the three compounds is shown. The less symmetric V_2O_5 shows the highest peak, while V_2O_3 pre-edge feature is almost negligible. This phenomenon can be explained on the basis of group theory.[21] The key concept is that, for non-centrosymmetric structures like V_2O_5 the hybridization of d and p orbitals is possible and consequently the pre-edge peaks are intense because of the allowed dipole transition from core 1s to p levels. This kind of hybridization is impossible in regular octahedral structures with an inversion center. This explains why V_2O_3 shows the weaker pre-edge feature in Figure 1.7.

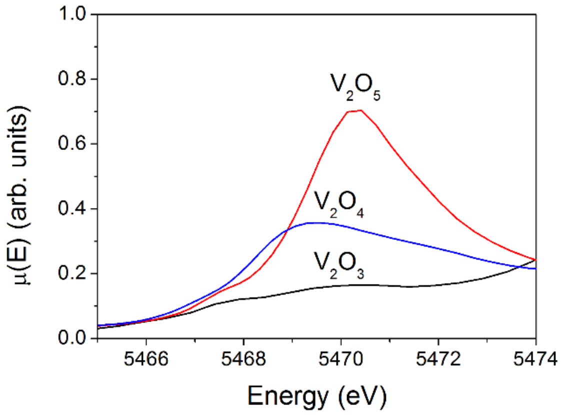

Figure 1.7: Pre-edge peaks of three V oxides.

This behavior is rather general among transition metal oxides as reported in several studies on other compounds.[20,22]

THE EDGE

The edge is defined as the onset of the continuum state and its position (E_0) is strictly related to the oxidation state of the absorber. This dependence can be easily explained using a simplified model as shown in Figure 1.8.

The strongest force acting on core electrons is the Coulomb interaction with the positive nucleus. The presence of other electrons, however generates a not-negligible repulsive electric field that lowers the energy needed to extract the electron from the atomic potential. This electron-electron contribution generates a screening of the Coulomb interaction between electrons and nucleus and for this reason is known as screening potential. The oxidation state of an atom depends on its electronic configuration when incorporated in a molecule. Some of the valence electrons can be transferred from or to the ligand species, depending on their electro-negativity. This change of electronic configuration influences the screening potential of the absorber atom. If the oxidation state rises (the atom donates charges to the ligands) the screening decreases and a higher energy is necessary to promote the electron transition to the continuum. On the other hand, in case of oxidation state reduction the electron transition to the continuum is favored and the needed energy is lower.

This correlation between edge position and oxidation state is very useful for XANES data interpretation. Comparing the edge position of an unknown sample with some references it is possible to have an indication of the oxidation state of the absorber in the unknown compound. The edge position E_0 can be easily evaluated finding the maximum of the spectrum derivative after the pre-edge region. Also in this case V oxides are very useful for a graphic and immediate representation of the physical concept. In Figure 1.9 it is shown how the edge position shifts to higher energies increasing V oxidation number. It is important to notice that a change of 1 in oxidation state can produce a visible shift of the edge of a few eV.

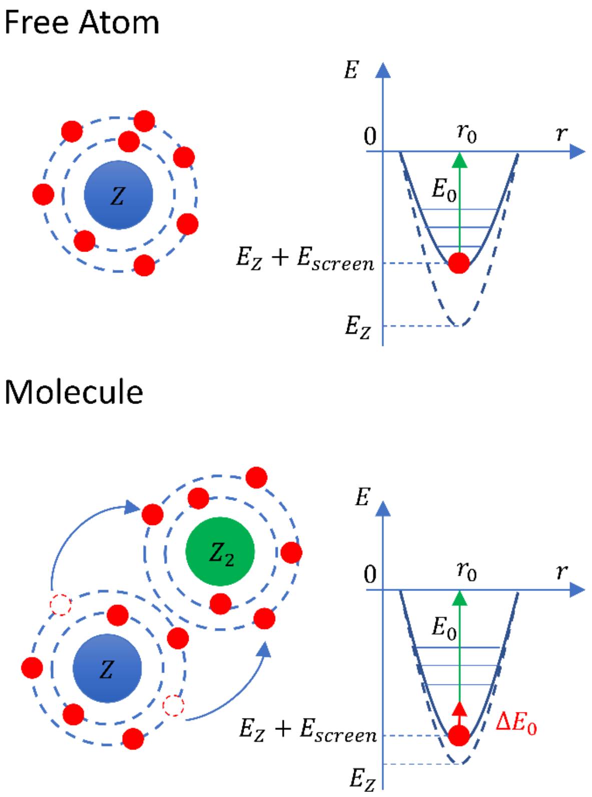

Figure 1.8: schematic description of the edge shift phenomenon. The interaction between the elements Z and Z_2 produces a lowering of the repulsive screening potential and a consequent increasing of E_0. In the right schemes E_z stays for the not-screened Coulomb potential while E_{screen} is the potential contribution due to electron-electron repulsion. The atomic potential is schematically simplified as a parabolic potential centered in r_0 that represent the average value of the distance between the electron and the nucleus.

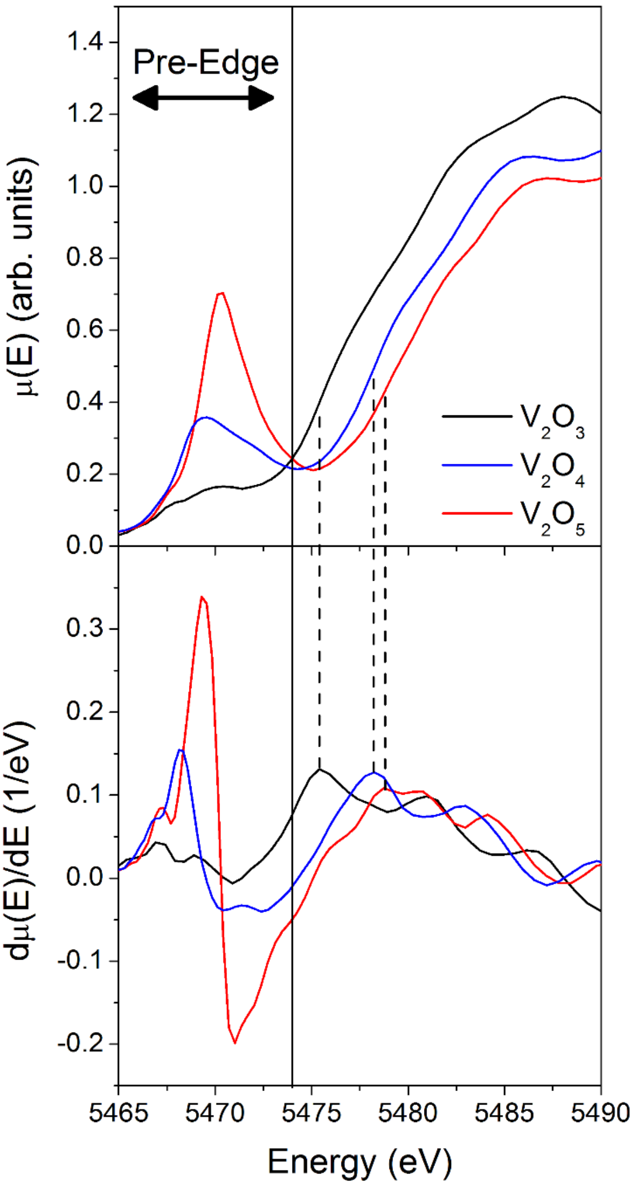

Figure 1.9: Comparison of the Edge position for V2O3 (V3+), V2O4 (V4+) and V2O5 (V5+). The edge position is clearly a function of the oxidation state.

POST EDGE REGION

The post-edge region is the section of the XANES spectrum generated by the interference of outgoing and scattered photo-electron wave-functions, the same physical mechanism discussed for EXAFS in paragraph 1.1.1.1. We mentioned above that the oscillating signal for EXAFS in a muffin-tin approach can be reconstructed using only a few scattering processes. In the XANES region, however, using the same approach it is possible to demonstrate that the series in equation 1.37 does not converge, so to obtain a satisfactory description of the near edge region is mandatory to consider all the possible multiple scattering paths. This approach is called full multiple scattering. Several codes for *ab initio* calculations rely on this kind of approach.[14,23] Recently, new methods were developed to overcome the muffin tin approximation and the full multiple scattering approach. In this work FDMNES,[24] will be mainly used, but several other codes based on DFT calculations are in continuous development.[25] A brief description of FDMNES will be given in paragraph 1.1.1.3.

THE LINEAR COMBINATION ANALYSIS

A common method to perform analysis of the XANES spectra of mixtures or multiphase compounds is the linear combination analysis. Starting from the spectra of selected reference species is sometimes possible with a linear combination fitting to reconstruct the unknown spectrum. In Figure 1.10 the application of this method to one of the V-TiO_2 nanoparticle samples studied in this work is shown. From XRD it is known that the overall structure of this nanoparticles is a superposition of three TiO_2 polymorphs (Rutile Anatase and Brookite). The advantage of using XANES instead of XRD, however is the possibility to use as reference spectra also those generated by low range ordered structures (amorphous) that are not detectable with XRD. In Figure 1.10 are shown two fits obtained with or without the spectrum of an amorphous TiO_2 sample (red solid curve). Using the linear combination fitting routine of the software Athena[26] it is possible to obtain the relative percentages of the different polymorphs and the χ^2 merit function as shown in Table 1.2.

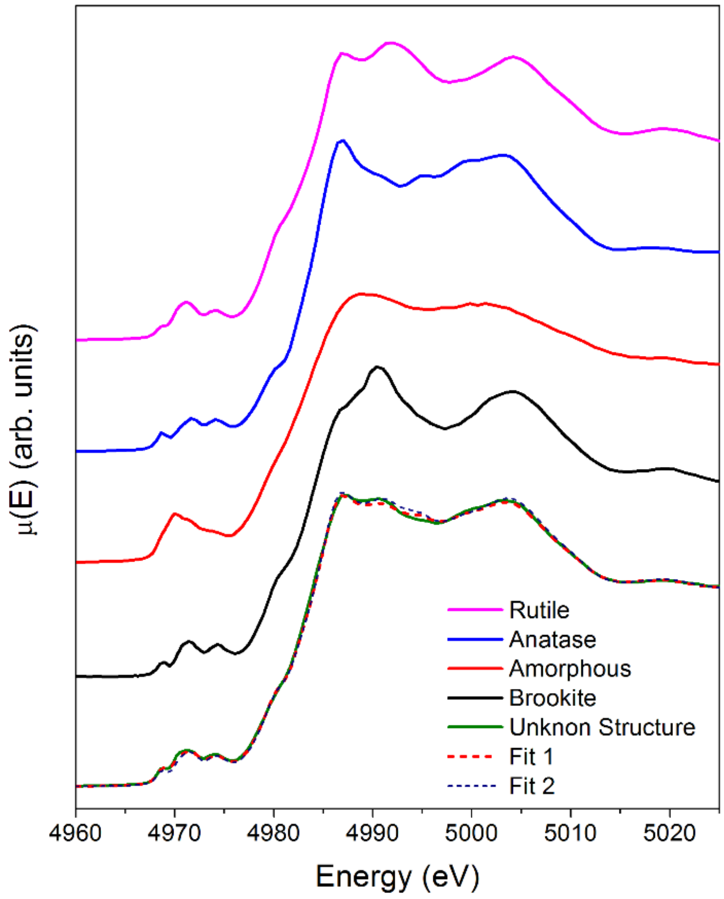

Figure 1.10: Fit of the unknown structure using different sets of standards

Table 1.2: Percentages of the standards used to fit the unknown structure. The fit including the amorphous structure gives a better value of χ^2 and a major agreement with the unknown spectrum.

Fit	Rutile Percentage	Anatase Percentage	Brookite Percentage	Amorphous Percentage	χ^2
Fit 1	28% (4%)	44% (1%)	12% (2%)	15% (2%)	0.009
Fit 2	41% (4%)	43% (4%)	16% (3%)	-	0.019

1.1.1.3 FROM XAFS OSCILLATIONS TO THE LOCAL STRUCTURE (COMPUTATIONAL METHODS)

The phenomenological approach to XAFS described in the previous chapter can be followed by a more rigorous description based on *ab initio* calculations. The XANES lineshape can be interpreted to understand which structural model gives rise to the specific interference pattern behind XAFS spectra. The approaches for EXAFS and XANES used in all the characterizations described in this work are slightly different. For both methods, a starting set of coordinates is needed. This set can be obtained from X Ray Diffraction (XRD) patterns in case of standard compounds or calculated *ab initio* with specific codes in case of engineered materials. Further in chapter 1.2 the theoretical background behind the density functional theory calculation of these coordinate sets will be briefly described.

The standard procedure for EXAFS is to fit the experimental signal with a theoretical one generated using the guessed structure. The fit procedure implemented in the IFEFFIT[27] code refines some of the parameters in the EXAFS formula (equation 1.39) . The best model is obviously the one better describing the experimental signal, but a good agreement is not sufficient. The goodness of a theoretical model depends also from the values of the refined parameters that must be reasonable.

For XANES, as mentioned in section 1.1.1.1 the muffin tin potential is not always a good approximation. Several full potential approaches were developed in these last years.[24,25] These kind of calculations, however can be very time demanding, so a real fit is very difficult. Simulating several spectra slightly varying the starting structural configurations could take months with a normal calculator, so the approach adopted during my PhD was to choose between the various theoretical models the one that generates a theoretical XANES spectrum comparable with the experimental data. This means that XANES analysis are less quantitative than EXAFS ones, but the number of free parameter used is a lot less.

In the following paragraphs, the two codes used for EXAFS and XAFS analysis will be briefly described. The first one, FEFF[14], is a world-wide known software for the analysis of the extended region. The other software is FDMNES,[24,28] one of the most recent software for full potential *ab initio* calculation of the XANES region.

FEFF

FEFF[14] and IFEFFIT[27] are two packages developed by researchers from the Seattle group to analyze EXAFS spectra. They can be used from the command line or with the graphical user interface Demeter[26] that contains also several useful tools for data treatment.

As demonstrated in section 1.1.1.1 the EXAFS signal can be reproduced as the sum of several contributions related to different scattering paths according to eq. 1.40 where the index i is related to a single or multiple scattering path.

$$\chi(k) = \sum_i \chi_i(k) \qquad 1.40$$

FEFF, starting from a user-defined set of atomic coordinates, calculates all the possible scattering paths and their contributions to the overall EXAFS signal using equation 1.41, where k and R_i are calculated from equation 1.42 and 1.43.

$$\chi_i(k) = \frac{N_i S_0^2 F_i(k)}{k R_i^2} \sin\big(2kR_i + \phi(k)\big) e^{-2k^2\sigma_i^2} e^{-\frac{2R_i}{\lambda(k)}} \qquad 1.41$$

$$R_i = R_0 + \Delta R_i \qquad 1.42$$

$$k^2 = \frac{2m(E - E_0)}{\hbar^2} \qquad 1.43$$

The number of parameters in these equations is big, so the meaning of each symbol is explained in Table 1.3. Some of these parameters are calculated by FEFF starting from the cluster potential modeled with the muffin tin approximation. Not all the parameters can be calculated *ab initio*. Some of them like the Debye Waller factors (related to the sample temperature and intrinsic disorder) must be refined by IFEFFIT during the fit procedure starting from reasonable guessed values. In Table 1.3 are listed all the parameters divided in the calculated and fit refined categories.

Table 1.3: Description of the parameters needed to produce the theoretical signal

Ab Initio Parameters	Physical Meaning
$\boldsymbol{R_0}$	Path half-length calculated from the coordinate set
$\boldsymbol{\lambda(k)}$	Mean Free Path of the photo-electron
$\boldsymbol{F_i(k)}$	Scattering amplitude
$\boldsymbol{\phi(k)}$	Phase-shift induced by the atomic potentials
Fit-Refined Parameters	**Physical Meaning**
$\boldsymbol{S_0^2}$	Inelastic contribution of the non-excited electrons
$\boldsymbol{N_i}$	Degeneracy of the i^{th} scattering path
$\boldsymbol{\sigma_i^2}$	Debye Waller factor

$\boldsymbol{\Delta R}$	Variation of the path half-length
$\boldsymbol{E_0}$	Energy Shift

IFEFFIT can perform fits in the k or R space modelling the theoretical signal to reproduce $\chi(k)$ or its the Fourier transform $\chi(R)$. This last is sometimes preferred, providing direct information about the interatomic distances of the first atomic shells.

The goodness of a fit, both in k or in R space, can be evaluated with a merit function r defined, as shown in equation 1.44. Lower is the value of the merit function and better is the agreement between experimental data and calculated signal.

$$\mathrm{r} = \frac{\sum\left[\chi_{observed} - \chi_{fit}\right]^2}{\sum\left[\chi_{observed}\right]^2} \qquad 1.44$$

As previously mentioned minimization of r is not sufficient to have a good fit. The values of fit parameters should be physically reasonable. When the number of parameters used is too high the fit can give misleading results due to unwanted correlations between the various parameters. A way to handle this problem and perform a meaningful fit is to relate with mathematical constrains several parameters reducing the number of free ones. In one of the papers published during my Phd course[1] based on EXAFS and XANES analysis of phthalocyanine compounds, adopting some results from Haskel[29] and Poiarkova,[30] a significant reduction of the parameters number was possible relating some of the multiple scattering Debye Waller Factors to those of single scattering paths.

FDMNES

The calculation of the theoretical XANES spectrum is way more complex than the EXAFS one. The muffin tin approximation and the related multiple scattering approach, can be sometimes inadequate as shown by Kravstova and co-workers.[31] They compared the theoretical spectra calculated using a muffin tin based software (FEFF[14]) and a full potential one (FDMNES[24]). The full potential approach is shown to well reproduce all the anatase features, better than the multiple scattering code. Since the samples analyzed in this work are mostly based on TiO_2 polymorphs, FDMNES seemed to be the best candidate to reproduce their absorption spectra.

In this paragraph, a brief description of FDMNES will be shown. Detailed descriptions of the code can be found in references.[24,28,32] Since FDMNES is a full potential software, parts of its code are based on simplified versions of the Density Functional Theory described in Chapter 1.2.1. The first step, is a self-consistent calculation to get the starting charge configuration and electronic potential surrounding the absorber. The Coulomb potential of the atomic cluster surrounding the absorber is evaluated solving the Poisson equation once the charge density is evaluated with the LDA -U technique. To calculate XANES spectrum, it is necessary to assume an excited electronic configuration for the absorber. This is implemented placing the core electron in the first available unoccupied level. The core of the calculation is the evaluation of the final state $|\psi_f\rangle$ in equation 1.16. This is performed solving the Schrodinger equation with the finite difference method. This approach consists in constructing a space grid and discretizing the Schrodinger equation on its points. Of course, the Coulomb potential in the

Schrodinger equation is the one obtained previously with the iterative self-consistent calculation. This means that no approximation is made on the shape of the potential, overcoming the muffin tin approximation. The final state wave-function is then used to calculate the matrix element M_{fi} and consequently the absorption spectrum.

The theoretical absorption spectrum requires often to be convoluted before the comparison with the experimental data, because of the broadening due to the core-hole width Γ_{hole} and to the spectral width $\gamma(\omega)$ of the final state. This convolution is made using an energy dependent Lorentzian function Γ_f.

1.1.2 RESONANT INELASTIC X-RAY SCATTERING (RIXS)

Until now, only X ray absorption techniques were described, however combining them with X-ray emission spectroscopy (XES) it is possible to obtain an extremely powerful technique called Resonant Inelastic Scattering (RIXS) giving a wider range of information about the chemical properties of the absorbers' environment. XES can be classified in two regions. If the incoming photon energy (indicated with $\hbar\Omega$) matches one of the absorption edges of the selected element the result is a resonant mechanism of excitation and emission passing through a core-hole excited state. The emission spectrum in this case is strongly dependent from the incident photon energy $\hbar\Omega$. This is the base phenomenon exploited in the so-called resonant X-ray Emission spectroscopy (RXES). If the incoming photon energy is well above the absorption edge the dependence from Ω vanishes and the emission phenomenon is labelled as normal. For this the relative technique is also called normal X-ray emission spectroscopy (NXES).

It is easy to understand that RXES is a lot more interesting than NXES. Depending on the emitted photon energy ($\hbar\omega$) RXES can be divided in two sub-categories. If ω is equal to Ω the phenomenon is called resonant elastic X ray scattering (REXS), while if ω is lower than the incoming photon energy, the sample absorbs part of the photon energy and the process is called inelastic X-ray scattering (RIXS). RIXS is a very powerful tool to study the electronic states in solids and in the next paragraphs the theory behind this experimental technique will be briefly described. There are already several reviews about this topic, and the formalism used in this section is the same used in references [7,33].

The interaction between electrons and photons was previously described in section 1.1.1.1 with a semiclassical approach. The perturbative potential can be written as:

$$H_{Int} = \frac{e}{m_e c}\sum_j 2\boldsymbol{p}_j \cdot \boldsymbol{A}(\boldsymbol{r}_j) + \frac{e^2}{2m_e c^2}\sum_j \boldsymbol{A}(\boldsymbol{r}_j)^2 \qquad 1.45$$

The incoming photons as previously mentioned have an energy $\hbar\Omega$ and its wave-vector is labelled as $\boldsymbol{k}_1$. On the other hand, the emitted photon energy, is indicated with $\hbar\omega$ and its wave-vector as $\boldsymbol{k}_2$. The differential scattering cross section can be derived in the minimal coupling formalism using the Kramers-Heisenberg equation (equation 1.46) where $\Omega_{\boldsymbol{k}_2}$ is the solid angle of collection and W_{12} is the transition rate.

$$\frac{d^2\sigma}{d\Omega_{\boldsymbol{k}_2} d\omega} = \frac{\omega^2}{c^4}\left(\frac{1}{2\pi}\right)^3 W_{12} \qquad 1.46$$

W_{12} can be calculated according to Fermi's golden rule, however it is necessary to remind that this kind of process is composed by two different steps (absorption and emission). Indicating with $|g\rangle$, $|i\rangle$, $|j\rangle$ respectively the unexcited state, the core-hole intermediate state and the final state after the emission, the rate W_{12} can be calculated as shown in equation 1.47.

$$\begin{aligned} W_{12} = \sum_j \frac{(2\pi)^3}{\Omega\omega}\left(\frac{e^2}{m_e}\right)^2 \delta\left(E_j - E_g + \omega - \Omega\right) \\ \times \left\| \left[\langle j|\boldsymbol{\rho}_{\boldsymbol{k}_1-\boldsymbol{k}_2}|g\rangle(\boldsymbol{\eta}_1\cdot\boldsymbol{\eta}_2) \right.\right. \\ + \frac{1}{m}\sum_i \left(\frac{\langle j|\boldsymbol{p}(\boldsymbol{k}_2)\cdot\boldsymbol{\eta}_2|i\rangle\langle i|\boldsymbol{p}(-\boldsymbol{k}_1)\cdot\boldsymbol{\eta}_1|g\rangle}{E_i - E_g - \Omega} \right. \\ \left.\left.\left. + \frac{\langle j|\boldsymbol{p}(\boldsymbol{k}_1)\cdot\boldsymbol{\eta}_1|i\rangle\langle i|\boldsymbol{p}(-\boldsymbol{k}_2)\cdot\boldsymbol{\eta}_2|g\rangle}{E_i - E_g - \omega} \right)\right]\right\|^2 \end{aligned} \tag{1.47}$$

The quantities $\boldsymbol{p}(\boldsymbol{k})$ and $\boldsymbol{\rho}(\boldsymbol{k})$ are defined as

$$\begin{aligned} \boldsymbol{p}(\boldsymbol{k}) = \sum_n \boldsymbol{p}_n e^{-i\boldsymbol{k}\cdot\boldsymbol{r}_n} \\ \boldsymbol{\rho}(\boldsymbol{k}) = \sum_n e^{-i\boldsymbol{k}\cdot\boldsymbol{r}_n} \end{aligned} \tag{1.48}$$

where the index n spans over the involved electrons. The energies E_g and E_i in equation 1.47 are respectively referred to the ground and core-hole excited states. The three terms in the square brackets are referred to different kind of scattering phenomena as shown in Figure 1.11. The first term is associated to an elastic scattering phenomenon, the Thompson scattering that does not create a core-hole excited state. The second term, instead, is the phenomenon that describes the decay of a core-hole excited state generated by the incoming X-ray photon. This is obviously the most interesting contribution for RIXS. This becomes even clearer considering that for photon energies close to the energy difference $E_i - E_g$ the second term diverges and the other two become negligible.

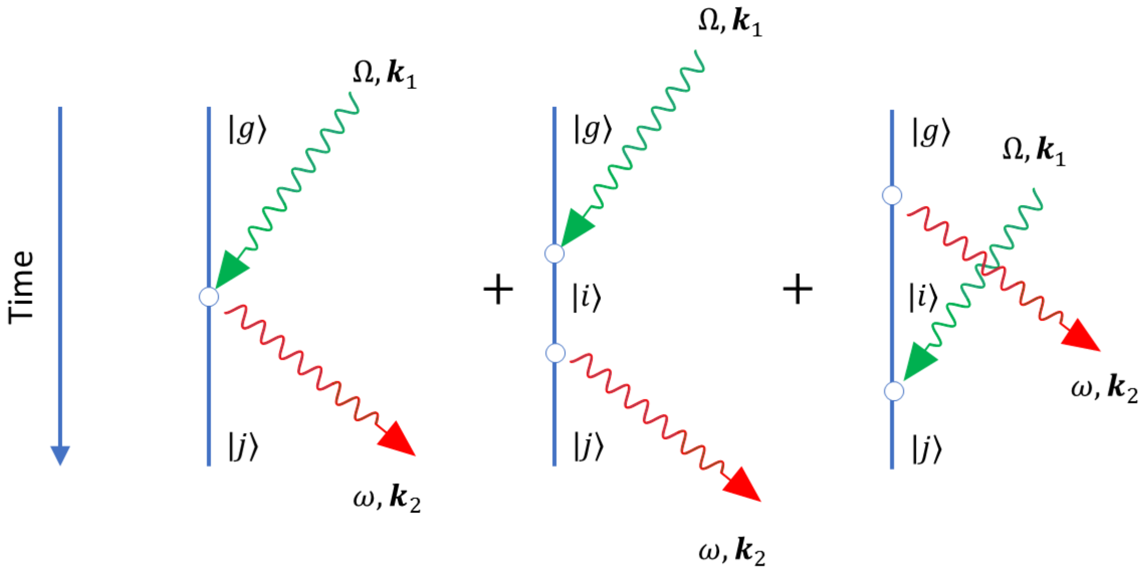

Figure 1.11: Schematic illustration of the three terms in square brackets of equation 1.47. The solid blue line represents the system of electrons, the white circles represent the interactions (absorption or emission) with the two photons (oscillating structures).

The problem of the divergence of the second term of the summation can be handled considering that the intermediate state $|i\rangle$ has a finite lifetime $\tau_i (= \hbar\Gamma_i)$. Because of this the energy E_i can be replaced by a complex value $E_i + i\Gamma_i$ removing the divergence problem. The RIXS spectrum can be thus described using equation 1.49 obtained from equation 1.47 removing all the negligible terms.

$$F(\Omega, \omega) = \sum_j \left| \sum_i \frac{\langle j|T|i\rangle\langle i|T|g\rangle}{E_g + \Omega - E_i - i\Gamma_i} \right|^2 \times \delta(E_g + \Omega - E_j - \omega) \qquad 1.49$$

The T operators in equation 1.49 represent the radiative transitions while Γ_i is the spectral broadening due to the core-hole lifetime in the $|i\rangle$ state. This parameter is considered constant for every possible intermediate state. If the final state $|j\rangle$ is the same as $|g\rangle$ equation 1.49 can be used to describe also the resonant elastic X ray scattering phenomenon. In general, from the spectrum $F(\Omega, \omega)$ it is possible to have a complete view of the electronic configuration around the absorber since both the absorption and decay processes are sampled.

From an experimental point of view RIXS is an evolution of X-ray absorption spectroscopy. The main difference is the presence of a high-resolution spectrometer needed to analyze the energy of the X-ray photons emitted from the sample in a determined solid angle, to reconstruct the $F(\Omega, \omega)$ spectrum.

A common way to show the $F(\Omega, \omega)$ spectrum is the RIXS map. Each point of this 2D plot is proportional to the number of fluorescence photons with a certain energy collected for several energies of the impinging photon. It is common use to place on the x axis of the plot the impinging photon energy and on the y axis the energy transferred to the sample. An example of RIXS plane is the one generated by a V doped TiO_2 thin film exciting the V K edge shown in Figure 1.12. Details about the samples and the meaning of the pre-edge peak will be better described later in this thesis.

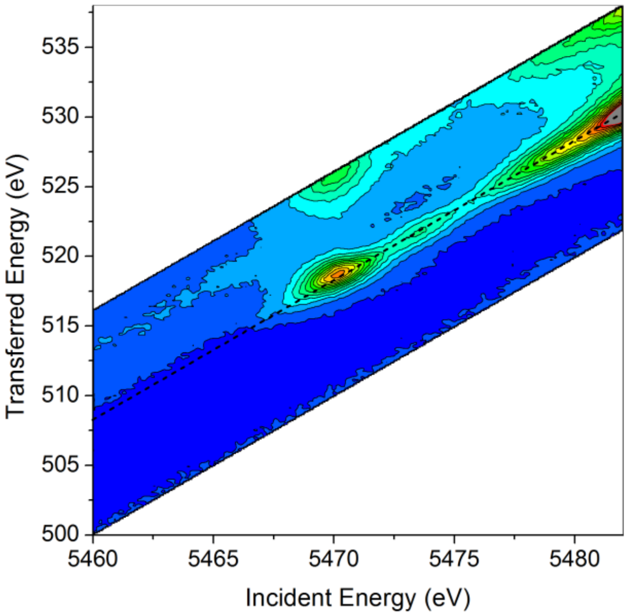

Figure 1.12: RIXS map of a V doped TiO_2 thin film at V K edge. The dashed diagonal line represents all the photons emitted at V K_α emission line

1.1.3 HIGH RESOLUTION FLUORESCENCE DETECTED X RAY ABSORPTION SPECTROSCOPY (HERFD XAS)

Another interesting technique based on the combination of XAFS and XES is the HERFD XAS. The subject of investigation, is the HERFD spectrum $\mu_H(E)$ and its variations related with the local structure surrounding the absorber. The number of fluorescence photons emitted by an irradiated sample is directly proportional to the absorption spectrum, because every core-hole excited state must decay emitting an X-ray photon or an Auger electron. The fluorescence photon energy, however, can change for decays involving different initial states. An example is shown in Figure 1.13 where the total fluorescence yield $\mu(E)$ and HERFD spectrum $\mu_H(E)$ collected at Ti K_β emission line are compared. The lowering of features A_1 and A_2 in the HERFD spectrum is related to their appearance at different emission energies. This can be seen in the references[34,35] where a RIXS spectrum of the pre-edge is shown. The different position of the pre-edge peaks in the emission energy range has been related to the different grade of localization of the orbitals giving rise to those features. According to Cabaret et al.[36] the core-hole influence is stronger on localized orbitals giving rise to features A_1 and A_2 that are so shifted in emission energy.

A clear advantage of HERFD is also the possibility to filter out contributions coming from the fluorescence of the surrounding atoms. In a compound, it is possible that some of the emission lines of the various elements are partially overlapped. In these conditions, collecting XAFS spectra in TFY mode the signal will be distorted by the unwanted background contributions. These can sometimes lead to misleading results. The high resolution RIXS spectrometer used for HERFD XAS can be tuned on a selected emission line removing the background coming from the other elements. This is extremely important in the study of low concentrated dopants, like in the case shown in this thesis involving V in a TiO_2 matrix.

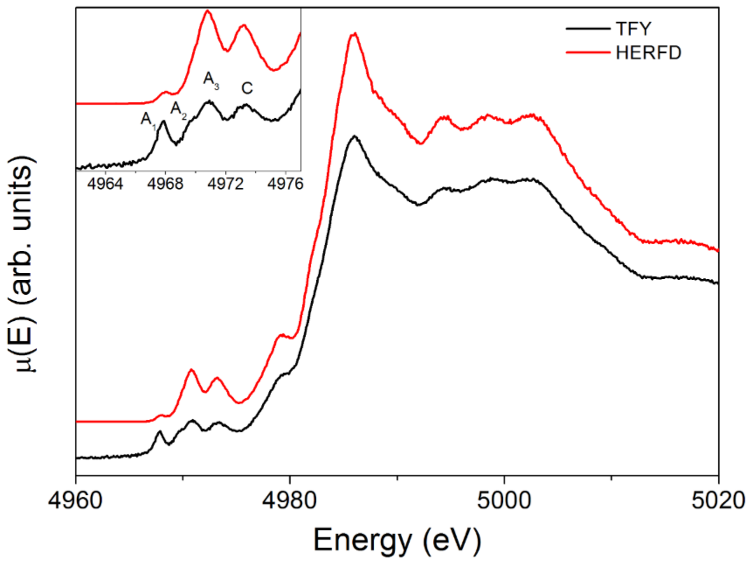

Figure 1.13: Comparison between the Total fluorescence yield and HERFD spectrum at Ti K_β emission line.

1.1.4 Optical Transient Absorption Spectroscopy

Pump and probe experiments are very powerful to follow the dynamic evolution of excited functional materials. The physical concept behind them, is to obtain the time dependence of a certain physical quantity after an excitation. All the experiments are characterized by the presence of an excitation (pump), that triggers the transition of the system to an excited state. Changes in the observed physical quantity are sampled with the probe measurements at known time delays from the excitation. In a pump and probe experiment the meaningful quantity to be measured is the transient signal that is a function of the time delay from the excitation (indicated with t). Defining A as the physical quantity to be monitored, the transient signal $\Delta A(t)$ can be obtained as sown in equation 1.50

$$\Delta A(t) = A_{pump}(t) - A_{unpump} \qquad 1.50$$

Optical transient absorption spectroscopy is a technique based on a pump and probe experiment. The physical quantity monitored is the visible absorption spectrum μ. This quantity is defined as shown for X ray absorption spectroscopy starting from the Lambert-Beer formula, shown in equation 1.1. The only difference is the wavelength of the incoming radiation. In the optical case, the typical range spans from the IR to the UV range.

The common setup adopted to perform such experiments is based on a single laser that performs both the pump and probe. A very simplified and schematic sketch is shown in Figure 1.14.

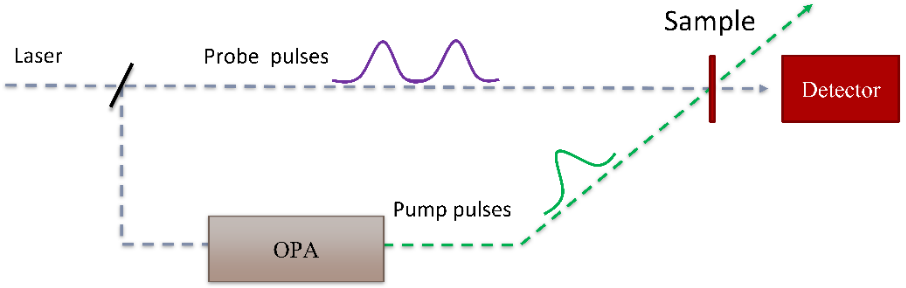

Figure 1.14: Schematic description of a common transient absorption spectroscopy setup

The pulsed laser beam is splitted in two branches. Pump and probe travel on different paths. The length difference between the paths is directly related to the time delay between the pump and the probe pulse on the sample. In order to measure a decay time trace, the length of one of the two patterns can be tuned using a moving stage, slightly changing the pump and probe delay.

In several experiments, like those showed in this thesis, pump and probe have different wavelengths. For this reason, in the two branches non-linear optical devices, like the optical parametric amplifier (OPA), can be installed to change the wavelength of the pump or probe pulse. In general, the pump pulse is chosen to be monochromatic, in order to excite only a selected transition. The probe pulse, instead is made of white light in to probe with in a single measurement all the absorption spectrum.

The time resolution of such pump and probe setups can be very high. It mainly depends on the time duration of the pump and probe pulses. Laser technology nowadays makes possible the measurements of electron dynamics appearing on the femtosecond timescale. In several applications it was also possible to achieve a time resolution on the attosecond timescale.[37]

1.2 MATERIALS MODELING

In this paragraph, the theoretical methods used to model the structure of doped compounds will be described. Nowadays there are several software[38–40] able to perform structural optimization and calculation of the quantum properties of molecules, crystals and atom clusters. Among them, for all the optimizations performed in this work Quantum ESPRESSO[38] was chosen. Like the most of *ab initio* codes it is based on the Density Functional Theory (DFT). In the next session, a brief description of this theory will be provided according to the formalism used in reference.[41] In this thesis *ab initio* codes are mainly used to obtain coordinates sets to be used in FDMNES, so a paragraph is dedicated to quasi-Newton methods used to optimize doped structures.

1.2.1 DENSITY FUNCTIONAL THEORY

In the following, the fundamental basis of the DFT elaborated by Kohn, Sham and Hohenberg[42,43] will be described. This theory simplifies a many body problem otherwise too complicated to be handled. The main issue of this theory is to relate all the physical quantities to the electron charge density n. In section 1.2.1.1 the Hohenberg-Kohn theorem, that relate charge density to the Coulomb potential of the screened nuclei, will be illustrated. This is the starting point to derive the Kohn-Sham equations describing the physics of the electrons of the system.

1.2.1.1 THE HOHENBERG-KOHN THEOREM

Let's consider a system of N interacting electrons in an external potential $v\ (\boldsymbol{x})$ determined by the superposition of the screened Coulomb potentials of the various atoms forming a cluster that can be a crystal or an isolated molecule. This potential is of course a function of the electron position $\boldsymbol{r}$, but it could also depend on its spin σ, so, without any approximation v is a function of the generalized coordinate $\boldsymbol{x}$ defined in equation 1.51

$$\boldsymbol{x} = (\boldsymbol{r}, \sigma) \qquad 1.51$$

In the following paragraphs, however the spin dependence will be ignored. The Hamiltonian of this system can be written as a functional of the potential v as shown in equation 1.52. In order to make the calculation easier all the multiplicative constants in the electron-electron interaction term are resumed in a constant called λ.

$$H[v] = -\frac{\hbar^2}{2m_e}\sum_{i=1}^{N}\nabla_i^2 + \sum_{i=1}^{N} v(\boldsymbol{x}_i) + \frac{\lambda}{2}\sum_{i\neq j}^{N} w\left(\left|\boldsymbol{r}_i - \boldsymbol{r}_j\right|\right) = T + U + W \qquad 1.52$$

The three terms in equation 1.52 are respectively the operators which expectation value are the kinetic operator (T) the external potential energy (U) and the electron-electron interaction (W). In the following calculations is useful to avoid the presence of several constants that can be put equal to one as shown in equation 1.53, without any loss of generality.

$$\hbar = m_e = \lambda = 1 \qquad 1.53$$

Consequently, energies will be expressed in Hartree (1 Hartree = 2Ry = 27.212 eV) and lengths in units of the Bohr radius a_{Bohr} $(0.52918 \cdot 10^{-10}\ m)$.

The functional dependence of H on v is affine-linear, it means that for two potentials v_1 and v_2 it is possible to write equation 1.54.

$$H[\alpha v_1 + \beta v_2] = \alpha H[v_1] + \beta H[v_2]\ with\ \alpha + \beta = 1 \qquad 1.54$$

All the Hamiltonians in equation 1.52 are considered bounded below. In other words, for a given electron-electron interaction w the ground state energy is finite and defined as shown in equation 1.55.

$$E_g[\quad] \overset{\text{def}}{=} \inf\{\langle\mathit{\Psi}|H[v]|\mathit{\Psi}\rangle \mid \Psi \in W_N\} \qquad 1.55$$

The wave-functions describing the system must satisfy some conditions resumed in equation 1.56 where the ensemble W_N is defined. These conditions, however, are quite reasonable since the wave-function of N fermions must be antisymmetric for particle exchange and it should be normalized and continuous.

$$\begin{gathered} W_N \overset{\text{def}}{=} \{\Psi \mid \Psi(x_1 \ldots x_N) \text{ antisymmetric}, \\ \langle\Psi|\Psi\rangle = 1, \\ \langle\nabla_i\Psi|\nabla_i\Psi\rangle < \infty \text{ for } i = 1 \ldots N\} \end{gathered} \qquad 1.56$$

The ground state (not necessarily unique) must be gauge invariant with respect to potential constants. It means that two external potentials are different only when $v_1 - v_2$ is not a constant function. In general, this property is summarized in equation 1.57.

$$E_g[v + const] = E_g[v] + N \cdot const \qquad 1.57$$

Indicating with $\Psi_0[v]$ the ground state wave-function for the Hamiltonian with external potential v it is possible to write equation 1.58.

$$H[v]\Psi_0[v] = E_g[v]\Psi_0[v] \qquad 1.58$$

Let's suppose that two different potentials can generate the same ground state ($\Psi_0[v_1] = \Psi_0[v_2] = \Psi_0$). Subtracting the two Schrodinger equations it will follow that:

$$\sum_i \big(v_1(x_i) - v_2(x_i)\big)\Psi_0 = (E_g[v_1] - E_g[v_2])\Psi_0 = \Psi_0 \cdot \text{const} \qquad 1.59$$

However, it was mentioned above that two different potentials cannot differ by a constant. This implies that $\Psi_0 = 0$, but also this case is impossible because this can happen only in presence of infinite potential walls that cannot be used to describe the Coulomb potential of an atom cluster. The logical consequence is that $\Psi_0[v_1] \neq \Psi_0[v_2]$ and equation 1.59 must be false. Since the electron density at the ground state can be expressed as:

$$n[v] = \langle\Psi_0[v]|\Psi_0[v]\rangle \qquad 1.60$$

It is clear that there is a unique relation between the external potential and the charge density as shown in 1.61.

$$n[v_1] \neq n[v_2] \quad \text{if} \quad v_1 \neq v_2 \qquad 1.61$$

This is the main point of the Hohnberg-Kohn theorem that can be expressed as:

There is at most one potential function $v(x) mod(const)$ for which $n(x)$ is the ground state density.

It means that it is possible to express the potential v as a unique function of the electron density n and consequently also the Hamiltonian functional will depend from this quantity.

Before discussing the origin of the Kohn-Sham equations it is necessary to define the Hohenberg-Kohn density functional (equation 1.62)

$$F_{HK}[n] \overset{\text{def}}{=} E_g\big[v[n]\big] - \int v[n]n\,dx \qquad 1.62$$

From a physical point of view the integral in the r.h.s is the Coulomb interaction energy U, so the Hohenberg-Kohn functional is an expression in terms of the charge density of the kinetic and electron-electron interaction energies. From these considerations, it is possible to derive the Hohenberg-Kohn variational principle (equation 1.63) that make possible the calculation of the ground state energy minimizing the quantity in brackets depending by two variables v and n considered independent.

$$E_g[v] = \min_{\mathrm{n}}\{F_{HK}[n] + \int vn\,dx\} \qquad 1.63$$

1.2.1.2 THE KOHN-SHAM EQUATION

In the previous section, it was shown that $F_{HK}[n]$, the Hohenberg-Kohn density functional, has a clear physical meaning as shown in equation 1.64.

$$F_{HK}[n] = \langle \Psi_0[n] | \mathrm{T} + \mathrm{W} | \Psi_0[n] \rangle \qquad 1.64$$

In particular, if w is 0 the density functional describes only the kinetic energy of the non-interacting system:

$$T[n] \overset{\text{def}}{=} \mathrm{E}_g^0\big[v^0[n]\big] - \int v^0[n]n\,dx \qquad 1.65$$

Determinantal states (antisymmetric combinations of one electron wavefunctions) can be a basis for the ground state of N non-interacting fermions. The density of a determinantal state can be expresses using equation 1.66 where the subscript i is referred to the considered electron.

$$n(x) = \sum_{\mathrm{i}}^{\mathrm{N}} \phi_i(x)\phi_i^*(x) \;\text{ for } \Psi_0^0(x_1 \dots x_N) = \frac{1}{\sqrt{N!}}\det\big||\phi_i(x_k)|\big|, \langle \phi_i | \phi_j \rangle = \delta_{ij} \qquad 1.66$$

The kinetic energy of such a system can be easily calculated as shown below:

$$T[n = \sum_{i}^{N} \phi_i\phi_i^*] = \langle \Psi_0^0 | T | \Psi_0^0 \rangle = -\frac{1}{2}\sum_{i=1}^{N} \langle \phi_i | \nabla^2 \, | \phi_i \rangle \qquad 1.67$$

Substituting this in the Hohenberg-Kohn variational principle it is possible to obtain equation

$$E^0[v] = \min_{\phi_i, \phi_i^*}\{\sum_{i=1}^{N}\left(-\frac{1}{2}\langle \phi_i | \nabla^2 \, | \phi_i \rangle + \langle \phi_i | v | \phi_i \rangle\right) \text{ with } \langle \phi_i | \phi_j \rangle = \delta_{ij}\} \qquad 1.68$$

Since the single particle wave-functions ϕ_i are orthonormal each term of the sum can be varied separately. This is equivalent to solve N Schrodinger equations like 1.69.

$$\left(-\frac{\nabla^2}{2}+v(x)\right)\phi_i(x)=\phi_i(x)\epsilon_i \qquad 1.69$$

In the interacting case, the Hartree and exchange term are present and the Hohenberg Kohn functional can be expressed as

$$F_{HK}[n]=T[n]+E_H[n]+E_{XC}[n] \qquad 1.70$$

The aim of the theory is to decompose the problem in N single particle equations like in the non-interacting case showed above. To do this the first step is to write the Hohemberg-Kohn variational principle using charge densities n derived from determinantal states (product of non-interacting single particles' wave-functions) as shown in equation 1.71

$$E_g[v]=\min_{\phi_i^*,\phi_i}\left\{\begin{matrix}\sum_{i=1}^{N}\left(-\frac{1}{2}\langle\phi_i|\nabla^2|\phi_i\rangle+\langle\phi_i|v|\phi_i\rangle\right)+E_H[n]+E_{XC}[n]\\ \text{with } \langle\phi_i|\phi_j\rangle=\delta_{ij} \text{ and } n=\sum_i^N \phi_i^*\phi_i\end{matrix}\right\} \qquad 1.71$$

It is possible to demonstrate that the Hartree contribution can be easily related to the electron density as shown in equation 1.73.

$$E_H[n]=\int n(\boldsymbol{r})w(\boldsymbol{r}-\boldsymbol{r}')n(\boldsymbol{r}')\,d^3r\,d^3r' \qquad 1.72$$

This means that it is possible to define an Hartree potential v_H acting as an external potential to be added to the Coulomb one. Of course, from equation 1.72 it is immediately clear that this potential is a function of the charge density itself.

The exchange correlation, instead has no direct relation with the density n. This means that the exchange correlation potential v_{XC} can be only defined as shown in equation 1.73.

$$v_{XC}\overset{\text{def}}{=}\frac{\delta E_{XC}}{\delta n(x)} \qquad 1.73$$

Finding the exact dependence of the exchange energy from the charge density is not trivial and this is the main reason why several different approaches for its calculation were developed in time (PBE[44], LYP[45] etc.…) .

Expressing Hartree and exchange contributions as external potentials is a clear advantage. The Hohenberg-Kohn variational principle is reduced to the case of non-interacting electrons as shown in equation 1.74.

$$E[v] = \min_{\phi_i^*,\phi_i} \left\{ \sum_{i=1}^{N} \left(-\frac{1}{2} \langle \phi_i | \nabla^2 | \phi_i \rangle + \langle \phi_i | v + v_H + v_{XC} | \phi_i \rangle \right) \; with \; \langle \phi_i | \phi_j \rangle = \delta_{ij} \right\} \qquad 1.74$$

Also in this case, the problem is reduced to the minimization of the energies of N single particle Schrodinger equations.

$$\left(-\frac{\nabla^2}{2} + v_{eff}(x) \right) \phi_i(x) = \phi_i(x) \epsilon_i \qquad 1.75$$

These equations are the so-called Kohn-Sham equations and the ϕ_i, their eigenstates are the Kohn-Sham orbitals that can be used to evaluate the charge density and all the related physical quantities. The calculation, however, is not trivial and time demanding, since v_{eff} depends on the charge density itself. This implies that the calculation must be iterative and self-consistent.

1.2.2 QUASI-NEWTON ALGORITHMS FOR STRUCTURAL RELAXATION

The calculation of the Kohn Sham functions is only the first step for materials modelling. Sometimes it is necessary to relax the crystal structure like in the case of doped materials described in this work. The most common approaches used by *ab initio* codes are the approximated Newton methods for nonlinear optimization. The theoretical base behind will be briefly described in the following paragraphs.

In the Born-Oppenheimer approximation atomic nuclei are considered fixed with respect to electrons, however the total energy of the system is still a function of their position, because the electron charge density is strictly related to the geometrical structure of the atom cluster. The total energy can be expressed as a functional $E[\boldsymbol{X}_1, \dots, \boldsymbol{X}_N, n(\boldsymbol{X}_1, \dots, \boldsymbol{X}_N)]$, where $\boldsymbol{X}_i$ are the ionic coordinates and n the electron density written as a function of the ionic positions.

Forces acting on the i^{th} ion can be determined with the laws of classic mechanics as shown in equation 1.76.

$$\boldsymbol{F}_i = -\frac{\partial E[\boldsymbol{X}_1, \dots, \boldsymbol{X}_N, n(\boldsymbol{X}_1, \dots, \boldsymbol{X}_N)]}{\partial \boldsymbol{X}_i} \qquad 1.76$$

Using the Hellmann-Feynman theorem these forces in an atom cluster can be expressed as:

$$\boldsymbol{F}_i = -\int n(\boldsymbol{r}) \frac{\partial v(\boldsymbol{r})}{\partial \boldsymbol{X}_i} d\boldsymbol{r} - \sum_{j \neq i}^{N} \frac{\partial E_{ij}(\boldsymbol{X}_1, \dots, \boldsymbol{X}_N)}{\partial \boldsymbol{X}_i} \qquad 1.77$$

Where E_j is the energy contribution due to the interaction between the i^{th} nucleus and the others N-1, while $v(\boldsymbol{r})$ is the Coulomb potential generated by the superposition of the screened nuclei. To perform a structural optimization, it is thus necessary to search the ion configuration leading to the equilibrium position when the forces $\boldsymbol{F}_i$ are null. The optimal configuration can be obtained iteratively. In Figure 1.15 is shown a hypothetical 2D potential energy surface with a minimum in the red dot. The blue particle starting from position $\boldsymbol{X}_1$ reaches the equilibrium position with a series of discrete steps (the subscript is now referred to the iteration step). The direction of the steps is determined by the direction of the energy gradients $\boldsymbol{g}$ that is always perpendicular to the equipotential surfaces (blue ellipses) and parallel to the forces F_i. This iterative procedure for the ion is summarized in equation 1.78 where the λ is the amplitude of the step.

$$\boldsymbol{X}_{k+1} = \boldsymbol{X}_k - \lambda \frac{\boldsymbol{g}_k}{|\boldsymbol{g}_k|} \qquad 1.78$$

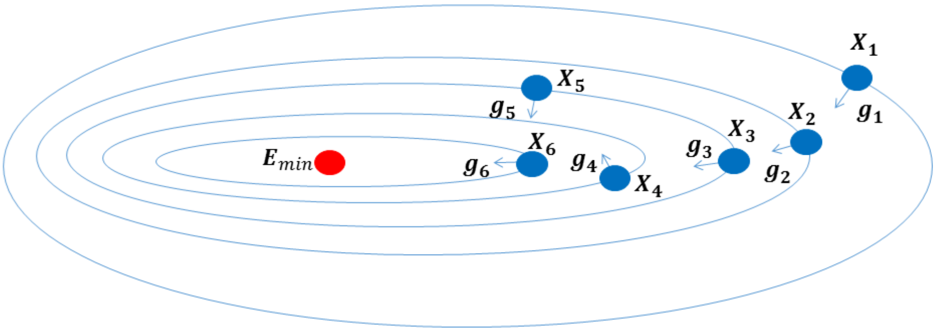

Figure 1.15: The particle starting from position $\boldsymbol{X}_1$ reaches the minimum of the energy in the red dot by discrete steps in the gradients $\boldsymbol{g}_k$ directions perpendicular to the equipotential surfaces.

Supposing that at the $(k+1)^{th}$ step a stationary point is reached it is possible to find the amplitude and the direction of the step to be performed to relax the system in one iteration. Let's take a Taylor expansion of the energy as a function of the ion coordinates around stationary point $\boldsymbol{X}_{k+1}$

$$E(\boldsymbol{X}_{k+1}) - E(\boldsymbol{X}_k) = \boldsymbol{s}_k \boldsymbol{g}_k(\boldsymbol{X}^k) - \boldsymbol{s}_k^T \boldsymbol{\mathcal{H}}_k \boldsymbol{s}_k \text{ with } \boldsymbol{s}_k = \boldsymbol{X}_{k+1} - \boldsymbol{X}_k \qquad 1.79$$

In equation 1.79 $\mathcal{H}_k$ is the Hessian matrix calculated at the k^{th} step and $\boldsymbol{g}_k$ the gradient vector. This latter can be also expanded as shown in equation 1.80.

$$\boldsymbol{g}(\boldsymbol{X}_{k+1}) - \boldsymbol{g}(\boldsymbol{X}_k) = \boldsymbol{\mathcal{H}}_k \boldsymbol{s}_k \qquad 1.80$$

If a stable configuration exists after several iterations the force acting on the ion must decrease to zero. This is expressed in equation 1.81.

$$\lim_{k \to \infty} \boldsymbol{g}(\boldsymbol{X}_{k+1}) = 0 \qquad 1.81$$

This result can be used to derive a suitable expression for the step $\boldsymbol{s}_k^{NR}$ (equation 1.82) called Newton-Raphson step that bring the ion to the stationary point. This procedure works perfectly if the potential energy surface can be well approximated to a quadratic function and using the full Hessian matrix.

$$\boldsymbol{s}_k^{NR} = \mathcal{H}_k^{-1} g_k \qquad 1.82$$

For most of applications however the complete hessian is unknown and an approximated one is used. The process is so iterated moving the system of Newton-Raphson steps until a reasonable value of the forces acting on the ions is reached. For every step the approximated Hessian matrix must be updated. One of the most successful methods to do this is the Broyden–Fletcher–Goldfarb–Shanno (BFGS) that is shown in equation 1.83 where $\boldsymbol{\gamma}_k$ is the difference between the gradient at the $(k+1)^{th}$ step and the one at the k^{th}step.

$$\mathcal{H}_{k+1}^{-1} = \mathcal{H}_k^{-1} + \left(1 + \frac{\boldsymbol{\gamma}_k^T \mathcal{H}_k^{-1} \boldsymbol{\gamma}_k}{\boldsymbol{s}_k^T \boldsymbol{\gamma}_k}\right) \frac{\boldsymbol{s}_k \boldsymbol{s}_k^T}{\boldsymbol{s}_k^T \boldsymbol{\gamma}_k} - \left(\frac{\boldsymbol{s}_k \boldsymbol{\gamma}_k^T \mathcal{H}_k^{-1} + \mathcal{H}_k^{-1} \boldsymbol{\gamma}_k \boldsymbol{s}_k^T}{\boldsymbol{s}_k^T \boldsymbol{\gamma}_k}\right) \qquad 1.83$$

The demonstration of the BFGS algorithm is too specific to be included in this thesis and it can be found in the references. [46–50]

2 XAFS CHARACTERIZATION OF TIO$_2$ DOPED SYSTEMS FOR PHOTO-CATALYSIS

The possibility of determining the local structure around dilute species (e.g. dopants) in condensed matter is one of the most advantageous features of XAFS. The local character of this technique and its chemical selectivity make possible the measurement of local structural parameters, which can provide the structural basis for an understanding of the effects of dopant incorporation. The incorporation site of dopants in the host matrix can profoundly affect the optical and electronic properties of a compound. This is usually reflected in the efficiency of related devices. In this chapter the XAFS characterization of two promising photo-catalytic systems, V and V-N doped TiO$_2$ will be described. Using reference compounds spectra and *ab initio* calculations it was possible to determine the local structure of both dopants.

2.1 DOPED AND UNDOPED TIO$_2$ (POTENTIAL APPLICATIONS AND SYNTHESIS)

2.1.1 THE ENVIRONMENTAL IMPORTANCE OF TIO$_2$

Before describing the experimental results obtained on various TiO$_2$ based systems it is interesting to discuss their importance for environmental and energy applications. Among the various wide band-gap oxides of transition metals, TiO$_2$ is one of those giving better results as photo-catalyst for several interesting reactions like water splitting and organic pollutants degradation.[51] The global importance of these two processes is immediately clear. Hydrogen is a viable candidate to replace fossil fuels. It can be applied in several existing technologies (cars, power plants, industries…) with the clear advantage that from H$_2$ combustion no greenhouse gas is produced.[9,52–54] Moreover, water decontamination is becoming necessary to contain the growing pollution leaded to massive industrialization.[55–57]

TiO$_2$, compared with other promising materials, has some clear advantages. For example, it is relatively not-expensive and, above all, biocompatible and non-toxic. The efficiency of solar devices for water splitting based on bare TiO$_2$ it is still not competitive.[9,58] The main issue is related to the wide band-gap characterizing this oxide. Most of the photo-catalytic properties of TiO$_2$ are related to the presence of electron and holes available for photo-reduction processes. Electron-holes couples, can be generated exciting electronic transitions from the valence to the conduction band, but being the bandgap of TiO$_2$ around 3.0 eV, this can be done using UV radiation only. Since a very small portion (around 5%) of the solar spectrum is in the UV region it is clear that bare TiO$_2$ cannot achieve competitive efficiencies. Furthermore electron-holes pairs generation it is not a sufficient condition to have an efficient photo-catalyst. Charge trapping and surface phenomena play a fundamental role. The efforts of the scientific community working on these systems are mainly concentrated in lowering the energy necessary to trigger the photo-excitation. This can be done with several methods (doping, plasmon nanoparticles, dyes, …). In the literature there are already several review articles explaining the state of the art of the researches performed on TiO$_2$ based systems,[51,59] but there is still a lot to understand in order to design even more efficient, knowledge based devices.

2.1.2 V AND V-N DOPED SAMPLES

Among the various techniques investigated to improve the efficiency of TiO_2, doping is one of the most studied. The physical concept is to incorporate atoms that, injecting charge carriers, can lower the energy needed to activate the photo-catalyst. Doping TiO_2 with 3d-transition metals like V is known to be an efficient method to improve visible-light photocatalytic activity.[60,61] According to theoretical investigations this is related to the creation of filled intra-gap states that can lower the excitation bandgap.[62] Another possible route is N doping, related to the generation of acceptor states above the valence band.[63] However, in both cases, as mentioned above, light absorption is not a sufficient condition to determine the photo-catalytic efficiency of a compound. The structural and electronic modifications introduced by dopants can deeply influence the lifetime of photo-generated electron-hole states, creating recombination centers that speed up the exited states decay processes.

In this thesis V and V-N doped samples were analyzed. In particular, V incorporation was investigated both in nanoparticles and thin films grown with different physical processes.

Nanoparticles were grown via gas phase condensation in a vacuum chamber ($\approx 10^{-5}$ Pa) filled with 266 Pa of He. Ti and V powders were mixed in the right proportions and loaded on a W boat. To obtain a precursor T-V alloy the powder mixture is first heated above the melting point of Ti (1668 °C). The system is left to homogenize 2 hours at 1200 °C where no significant evaporation takes place. After, the evaporation is performed admitting He in the chamber in proximity of the W boat fluxing the alloy vapors to a liquid nitrogen cooled cylinder. The evaporation rate is constantly monitored with a quartz microbalance. To maintain it constant the W boat temperature is continuously tuned to compensate variations. During the evaporation, Oxygen is admitted inside the chamber up to 2.6 KPa. The TiO_2 nanoparticles deposited on the cylinder show an amorphous structure. To obtain fully crystalline samples an annealing procedure is performed at 400 °C for six hours. SEM and a TEM images of the NPs are shown in Figure 2.1. The average nanoparticle size oscillates between 10 and 20 nm. It is possible to observe that the particles aggregate in large agglomerates with diameters around 100 nm. The V content can be roughly estimated using Energy Dispersive X-Ray spectroscopy (EDX). Further and more detailed information about the deposition procedure can be found in references.[2,4] In general, the resulting crystal structure, as confirmed by the diffraction patterns shown in Figure 2.2, is a superposition of anatase and rutile with very small percentages of brookite. The relative fraction of anatase and rutile polymorphs seems to be related to the evaporation rate. Samples with higher rutile fractions were obtained with fast evaporations, while anatase-like samples are associated to slow ones. The physical phenomenon behind the correlation between evaporation rate and samples' crystal structures it is still under investigation.

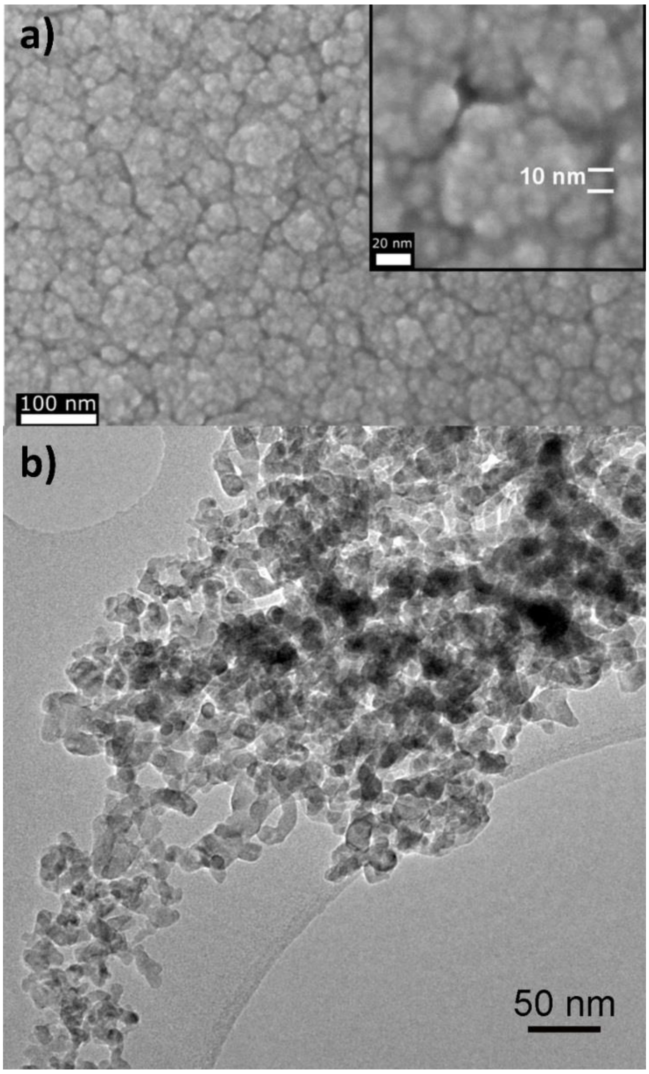

Figure 2.1 a) SEM image of V-TiO_2 nanoparticles deposited on Silicon substrate. In the inset the zoom of a nanoparticle agglomerate. Image taken from [2] b) TEM image of V-TiO_2 nanoparticles Image taken from reference [4]

For XAFS investigations several nanoparticle samples were grown with different structures or dopant concentrations. Nanoparticles were deposited during the evaporation on a Si (111) substrate. The thickness of the films checked with the atomic force microscope was around 240 nm for all the samples. The V content in the samples was determined by EDX in a Cambridge Stereoscan 360 Scanning Electron Microscope (SEM). The measured V concentrations will be expressed in atomic percentage, defined as the ratio between the number of V atoms and the total number of cations (Ti and V). In Table 2.1 the doping percentages and the main characteristics of the measured samples are listed. The overall crystal structure, checked with XRD, is amorphous for as deposited samples and a mixture of anatase and rutile for the annealed ones. The dependence of the crystallinity from the annealing temperature is visible in Figure 2.2 where the structure of an 8% V doped powder sample is checked variating the annealing temperature that is maintained for 6 hours. XRD data were collected using a Panalytical X'Celerator powder diffractometer. Bragg reflections of anatase (a) and rutile (r) TiO_2 began to appear after annealing 300 °C, while full crystallization was induced by annealing at 400 °C. In the XRD patterns, Bragg reflections attributable to vanadium oxides were never detected.

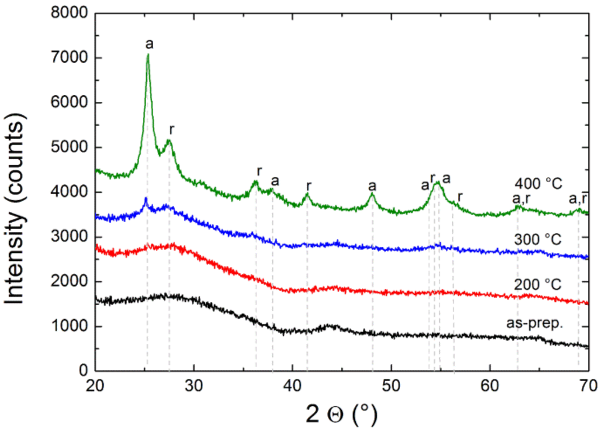

Figure 2.2: XRD patterns of a nanoparticle sample with 8 at.% V subjected to 6 hours annealing at different temperatures. The Bragg reflections of anatase (a) and rutile (r) TiO2 are indicated. The different patterns are vertically shifted for the sake of clarity.

As mentioned above the relative percentages of the two phases rutile and anatase are related to the deposition rate. Faster deposited samples like sample 5 show a major percentage of rutile phase, while the structure for those evaporated with a rate of 1.4 nm/min usually show a mixed structure.

Table 2.1: Properties of nanoparticle samples

Sample	$\frac{N_V}{N_V+N_O}$ **(at. %)**	**deposition rate (nm/min)**	**Description**
1	3.5 ± 1.0	1.4	as – deposited
2	3.5 ± 1.0	1.4	annealed at 400 °C
3	4.4 ± 1.1	1.9	as – deposited
4	4.4 ± 1.1	1.9	annealed at 350 °C
5	4.4 ± 1.1	1.9	annealed at 400 °C
6	7.5 ± 0.9	1.6	annealed at 400 °C
7	8.0 ± 1.2	1.6	as – deposited
8	8.0 ± 1.2	1.6	annealed at 400 °C

V-doped and V-N-co-doped TiO_2 thin films were deposited on glass substrate by radio frequency magneton sputtering using a TiO_2 target and Argon as working gas.[3] V-doping was obtained by placing V pieces over the TiO_2 target, while N-doping was obtained introducing into the deposition chamber a controlled N_2 flux. Changing the temperature of the deposition substrate it is possible to determine the crystal structure of the film. If the substrate temperature does not exceed the 70 °C or in general remains at room temperature the sample structure is amorphous. If the substrate is maintained at 350 °C the deposited sample undergoes to an annealing process and crystallizes.

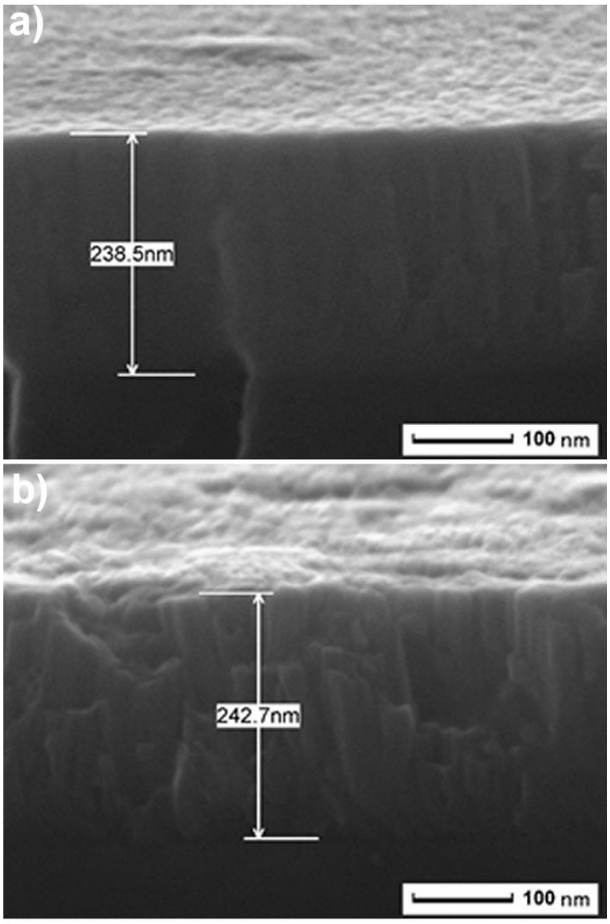

Figure 2.3: Cross Sectional SEM images of amorphous (a) and crystalline (b) V-TiO2 thin films

Using Raman spectroscopy, it was possible to determine the dominant phases. Raman spectra of V-TiO_2 and V-N-TiO_2 films deposited at a substrate temperature of 350°C are presented in Figure 2.4. These samples are crystalline and present the characteristic five peaks of the anatase phase: at 144 cm^{-1}, 197 cm^{-1}, 399 cm^{-1}, 513 cm^{-1} and 639 cm^{-1}, which are attributed to the E_g, E_g, B_{1g}, A_{1g}, and B_{2g} modes, respectively.[64] Moreover, the peak widths indicate a good crystalline quality of the V-doped samples. The spectrum of V-N-TiO_2 exhibits broader features, suggestive of a lower crystalline degree; moreover, the presence of a weak peak around 260 cm^{-1} and the small shift of the two peaks at 399 cm^{-1} and 639 cm^{-1} towards higher and lower wavenumbers, respectively, may indicate the presence of a small amount of rutile phase. No Raman peaks were detected in the thin films deposited at low temperature (inset of Figure 2.4(a)), indicating that these films are amorphous.

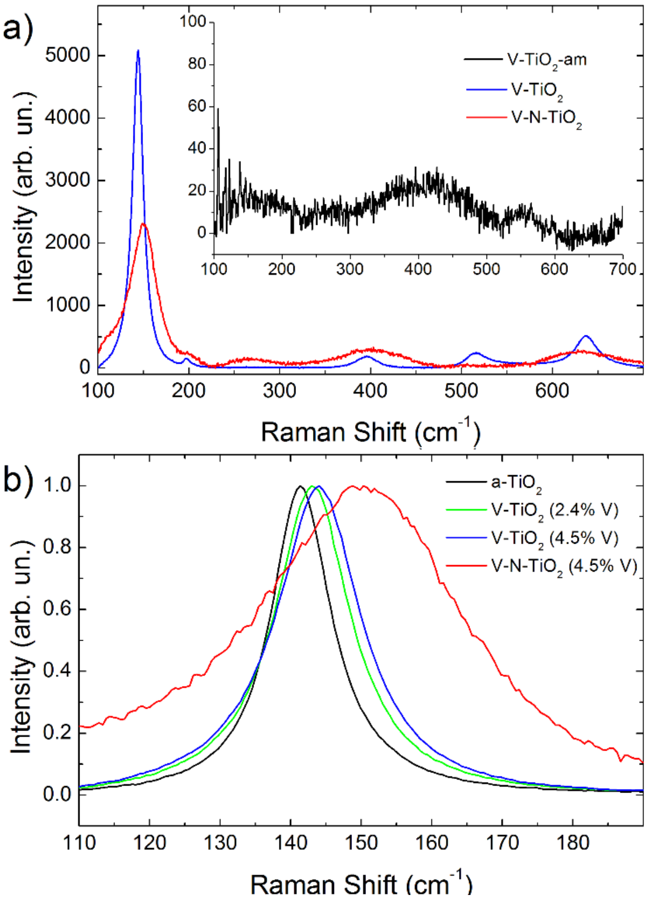

Figure 2.4: (a) Raman spectra of V-TiO2 and V-N-TiO2; the inset in (a) shows the Raman spectrum of an amorphous V-TiO2 thin film labelled as V-TiO2-am. (b) Detail of the main Raman peak, normalized to the same maximum intensity, for pure anatase (a-TiO2), V-TiO2 films with different V content (2.4 and 4.5 at.%) and V-N-TiO2.

The comparison between the normalized Raman spectra of V-TiO_2 with two different V contents revealed that the main peak at 144 cm^{-1} slightly broadens and shifts towards higher wave number with increasing V dopant level (Figure 2.4 (b)). The broadening and shifting effect is much more pronounced in case of additional N-doping. These features can be ascribed to smaller crystallite sizes affecting the force constants and the vibrational amplitudes of the nearest neighbour bonds[65]. The shift of the Raman peaks can also be induced by the incorporation of the dopants in the TiO_2 matrix, causing a distortion of the lattice and forming new bonds not present in pure TiO_2 film, and more generally by an internal strain field that affects the Raman peak positions.

For XAFS measurements four samples labelled with capital letters A, B, C and D were chosen. Sample characteristics are resumed in Table 2.2. Also in this case V concentration was estimated with EDX, while for N it was estimated using X-Ray Photoelectron Spectroscopy (XPS). Sample thickness in all the cases is 240 ± 20 nm as shown in Figure 2.3.

Table 2.2: Main characteristics of thin film samples

Sample	Substrate Temperature (°C)	$\frac{N_V}{N_V+N_{Ti}}$ (at. %)	$\frac{N_N}{N_N+N_O}$ (at. %)
A	< 70	4.5 ± 0.5	--
B	350	4.5 ± 0.5	--
C	350	4.5 ± 0.5	4.0 ± 0.7
D	350	2.4 ± 0.5	--

2.2 EXPERIMENTAL PROCEDURES AND SETUPS

XAFS measurements of nanoparticles and thin films samples were performed both in the hard and in the soft X-ray regimes, to have a complete overview of the local structure surrounding all the involved atomic species. This is especially important in the co-doped systems, since N and V K edges are in completely different energy ranges.

Hard XAS measurements at the Ti and V *K* – edges for all the samples except the V-N-TiO_2 sample C, were performed at the BM23[66] beamline of the European Synchrotron Radiation Facility in Grenoble, using a double bounce flat crystal Si(111) monochromator. Reference samples (Ti and V oxides) were measured in transmission mode using finely ground powders dispersed in polyethylene. Doped samples were measured in the fluorescence mode using a Vortex Si drift diode detector placed in the horizontal plane at right angles to the impinging beam. V K-edge XANES using the High Energy Resolution Fluorescence Detection (HERFD) XANES setup at the ID26[67] beamline were subsequently measured on the crystalline film samples B and C. In all the cases EXAFS signal were measurable with a good signal to noise ratio only at the Ti K edge. Because of the low dopant concentration and the partial superposition of the Ti K_β and V K_α emission lines, V K-edges were measured only in the XANES region.

Soft XAS measurements at the Ti and V $L_{2,3}$ – edges were performed at the BACH[68] and BEAR[69] beamlines at Elettra, the Italian synchrotron. In all these cases (except the N K edge of sample C collected in total fluorescence yield mode), the spectra were collected in the total – electron – yield (TEY) mode, by measuring the drain current from the sample to ground.

2.3 DATA ANALYSIS AND STRUCTURAL MODELLING

2.3.1 EXAFS PROCESSING

Ti K edge spectra were processed according to standard procedures using Athena.[70] The pre-edge region was fitted with a linear function while the post – edge region was fitted with a cubic spline to simulate the atomic cross section. As a first approximation, the energy origin for the energy – to – wavenumber conversion (E_0) was chosen as the maximum of the first derivative of the absorption spectrum. Quantitative data analysis was based on simulated signals calculated using the FEFF code[14] and non – linear fitting using ARTEMIS.[71] Analysis of the Ti *K* – edge EXAFS data of the two as – deposited samples will not be reported as these samples were highly disordered and it was not possible to obtain meaningful fits.

2.3.2 XANES TREATMENT

The analysis of the XANES region was performed both in a qualitative way (as shown in paragraph 1.1.1.2) and with a more rigorous approach based on *ab-initio* calculations described in the following paragraphs. In the second case, a two–step approach was followed. First of all, a structural relaxation was performed to determine the equilibrium atomic coordinates of Ti and O ions around the V dopant using a DFT approach as implemented in the Quantum ESPRESSO code;[72] subsequently, these coordinates sets were used as an input for full potential spectral simulations with the FDMNES code.[24] Similar or related approaches have been used for studies of dopants and defects in semiconductors.[73–80]

2.3.3 STRUCTURAL MODELS AND SIMULATIONS SETTINGS

V-TIO2 MODELS

Structural relaxations of V-TiO_2 models were performed for anatase and rutile phases, starting from known crystallographic structures.[18] For all the calculations, the pseudopotentials used for structural relaxations for Ti, V and O were chosen from the Quantum ESPRESSO database[81–83]. These pseudopotentials are Vanderbilt ultra-soft[84] with PBE (Perdew–Burke–Ernzerhof) exchange correlation functional.[85] Self-Consistent Field (SCF) calculations were performed using the Davidson algorithm while the structural relaxations using the BFGS (Broyden-Fletcher-Goldfarb-Shanno) one.[86,87] To obtain a realistic simulation of dopant environment at low concentrations, it is necessary to build a supercell, composed by several unit cells of the matrix compound. Quantum ESPRESSO automatically replicates this supercell performing calculations with the Plane-Wave algorithm using the PWscf code.[88] The cutoff energy for the plane waves basis wavefunctions was set at 30 Ry. To simulate a realistic environment for a low concentrated dopant, only one Ti atom was substituted with a V one inside the supercell. After this substitution, the BFGS routine was used to optimize the atomic positions and the supercell dimensions. The k-space sampling for the optimization was done using a 4 × 4 × 4 mesh. SCF convergence was achieved when the difference between the total energy calculated with self-consistent Kohn-Sham DFT and the value calculated with the non-self-consistent Harris energy functional[89] was lower than $1.3 \cdot 10^{-6}$ eV. The structural convergence, instead, was achieved when the total force inside the cluster was less than $1 \cdot 10^{-3} \frac{\mathrm{Ry}}{\mathrm{a_0}}$.

The supercell for rutile was formed by 2 × 2 × 3 tetragonal unit cells, with a total of 72 atoms corresponding to a vanadium-titanium percentage of 4.1%. Inclusion of V in rutile resulted in a compression and distortion of the octahedron formed by the O nearest neighbors; in the basal plane four O atoms relax towards the dopant by ~ 0.03 Å, while the two apical O atoms move inwards by ~ 0.027 Å. The supercell used for anatase was composed by 2 × 2 × 2 unit cells containing 96 atoms corresponding to the substitution of the 3.1% of titanium atoms with vanadium ones. Following inclusion of V in anatase the four O nearest neighbors in the basal plane contract inwards by ~ 0.027 Å and the two apical O atoms move inwards by ~ 0.03 Å. For anatase that is characterized by a less dense crystal structure also an interstitial V site was tested. It was obtained by relaxing the 96 atom super-cell of anatase with an extra V atom placed in the space between Ti octahedra. V-doped models are shown in Figure 2.5.

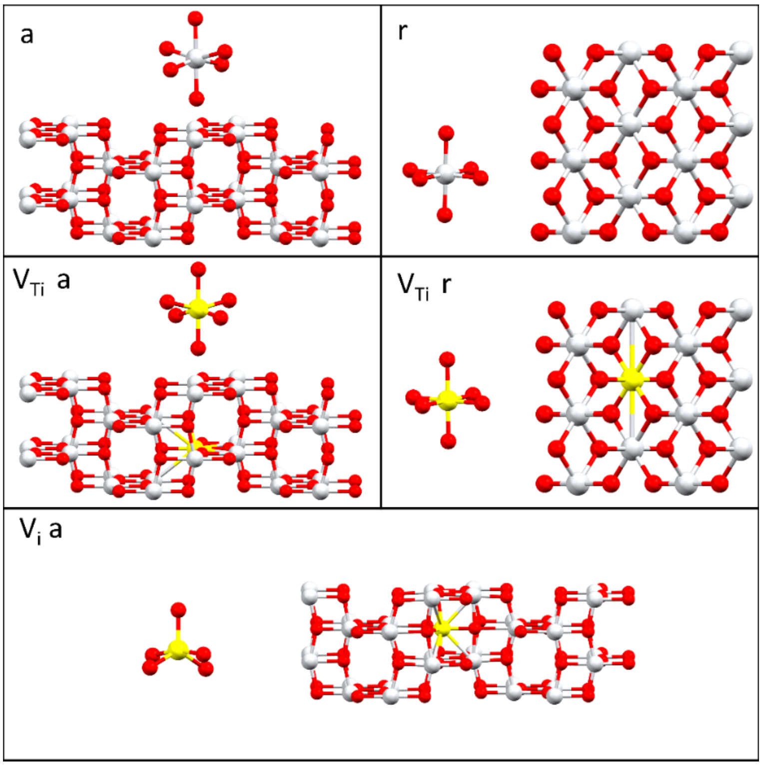

Figure 2.5: Models of the local structure for V – doped TiO2. “a” and “r” refer to anatase and rutile, respectively. The subscript Ti indicates a substitutional dopant while “i” stands for an interstitial one.

V-N-TIO2 MODELS

Being N a light element with a small atomic radius, the probability to find this dopant in stable interstitial configurations is quite high if compared to V. The possibility of an interstitial behavior was also investigated in the literature.[90] Below it will become clear that V can be found only in substitutional configurations. For this reason, all the proposed V-N models are based on the V_{Ti} ones. The structural optimization was performed using the same Quantum Espresso settings previously described for V doped models. The N pseudopotential was always a Vanderbilt ultra-soft one with PBE exchange correlation potential, chosen from the Quantum Espresso Repository.

In

Table 2.3 the seven investigated models (six for anatase and one for rutile) are listed giving a brief description of the starting and relaxed configurations. Quantum Espresso supercell coordinates are reported in the supplementary materials of reference [3]. The same models are shown in Figure 2.6 where pictures of the supercells are coupled with those showing the local structure of the two dopants.

Table 2.3: Description of the starting and relaxed dopant configurations for all calculated models of V and N dopants in TiO2. Only model M7 refers to rutile, while the other models are for anatase. The images of the corresponding relaxed structures are displayed in Figure 2.6.

Model Label	Starting configuration	Relaxed configuration
M1	V substitutes Ti and N replaces one neighboring O	The local geometry of the octahedron containing the two dopants is heavily

		distorted if compared with the anatase ones. The V-N bond length is ≈ 0.3 Å lower than the V-O ones that variate in a range between 1.87 Å and 2.20 Å
M2	V and N substitute Ti and O in different octahedra	The local geometries of the dopant-containing octahedra are similar to the anatase one where apical and basal atoms show different bond lengths, with longer apical distances. The V-O distances smaller than the Ti-O distances in undoped anatase variate between 1.87 Å and 1.95 Å. The Ti-N bond length is comparable with the V-O ones.
M3	V substitutes Ti. N is in an interstitial site near the V octahedron	N is attracted by the V octahedron and shares a corner with one O. The O-N couple is located ≈ 2 Å far from the V cation. One of the V-O bonds is shorter than the others measuring only 1.72 Å. This could be related to the presence of the V-O couple. The others V-O bond lengths variate in a range between 1.91 Å and 1.99 Å comparable with the Ti-O ones in anatase.
M4	V substitutes Ti. N is in an interstitial site far from the V octahedron	N is attracted by a Ti-centered octahedron and shares one corner with an O. The Ti-N distance is 1.95 Å. This model is quite unstable and difficult to relax compared with the others.
M5	V substitutes Ti. Far from the V dopant, a N_2 dimer substitutes one O in a Ti octahedron	The octahedron containing the two N atoms is slightly distorted compared to the anatase ones. The distance between the two N atoms and the Ti cation is 2.08 Å, a little bit higher than that observed in anatase for the apical O atoms.
M6	V substitutes Ti. A N_2 dimer is placed in an interstitial site far from V.	The presence of a N_2 dimer induces significant distortion of the surrounding structure as shown in Figure 2.6. The distance between the two N atoms is 1.11 Å, comparable with the interatomic distance observed in N_2 molecules.
M7	V and N substitute Ti and O in two distant octahedra of the rutile structure.	The N-containing octahedron is quite similar to rutile ones. However, the Ti-N distance is 1.87 Å, significantly shorter than the Ti-O distances in

		undoped rutile. The oxygen octahedron seems to be affected by the presence of N in the supercell because the rutile octahedron symmetry is lost. Two of the V-O bonds are shortened to 1.72 Å while other two are elongated to 2.13 Å.

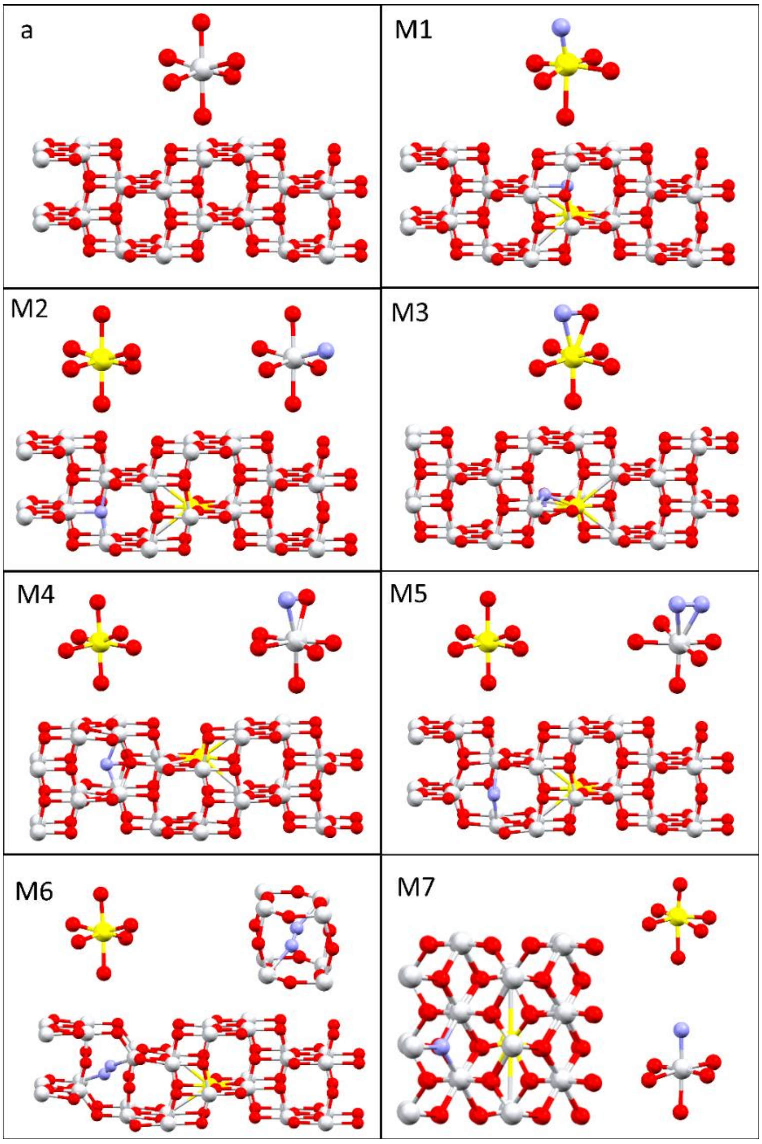

Figure 2.6: Relaxed structures for V-N-codoped TiO2. Ti in grey, V in yellow, O in red and N in blue. a: undoped anatase TiO2; M1-M6: V-N-codoped anatase; M7: V-N-codoped rutile.

FDMNES SETTINGS

The coordinate sets used as input for FDMNES were calculated as replicas of the Quantum Espresso super-cells described above. This procedure is fully justified, because of the plane wave algorithm used for the structural optimization. For each simulation, a cluster containing all the atoms comprised within a sphere of radius 6.5 Å centered on the absorber is considered. The SCF calculation, instead, was performed on a sphere of radius 4.00 Å surrounding the absorber. Calculations for V doped models at the V K edge were performed using the Perdew exchange correlation functional in order to be consistent with the Quantum Espresso relaxations. All the simulated spectra were convoluted using the standard FDMNES Γ function, to take in account the experimental and core-hole lifetime broadenings. This function is also designed to suppress all the filled levels lying below the Fermi energy. The latter is evaluated during the SCF calculation. Further details about the structural relaxation can be found in reference [2].

2.3.4 EFFECTS OF THERMAL TREATMENT

It was already clear from XRD and Raman analysis that thermal treatments (annealing for nanoparticles and heated substrates for thin films), induce crystallization. In this section, the effects of these treatments on the XANES spectra will be shown.

For both sample categories (NPs and TFs) the same behavior was observed. In general, as shown in Figures from 2.7 to 2.10, crystallization induces a clear sharpening of pre and post-edge spectral features at all the measured absorption edges. In the post edge region, a possible explanation for the broad features of the amorphous samples can be the lack of long-range order beyond the first coordination shells.

A very interesting behavior can be highlighted in figures from 2.8 to 2.10 where the $L_{2,3}$ and K edge spectra of Ti and V are shown. Thermal treatments, generate a visible blue-shift of the edge positions. According to the interpretation given in section 1.1.1.2, it is possible to relate crystallization to an increase of the oxidation state of the two cations. This phenomenon can be ascribed to the disappearing of low coordinated Ti^{3+} and V^{3+} site after the crystallization. In particular, in Figure 2.9, it is possible to observe that the main edge of the absorption spectrum associated to sample 4, annealed at 350 °C and not completely crystallized, is in an intermediate position between those of the as deposited and fully crystallized (annealed at 400 °C) samples. The O K edge position, instead remain the same after the thermal treatment, suggesting the absence of changes in oxidation state of anions.

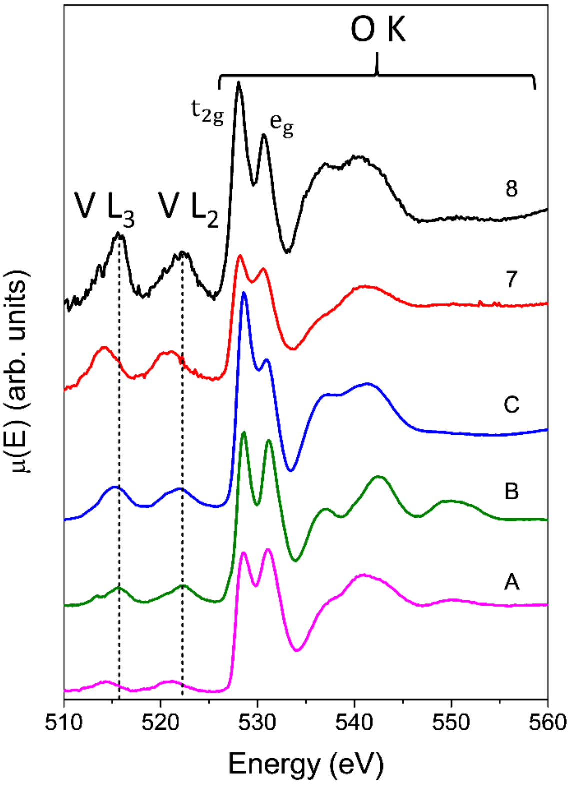

Figure 2.7: V $L_{2,3}$ edge and O K edge XANES spectra for nanoparticle and thin film samples. The position of the V $L_{2,3}$ edges for annealed samples is highlighted with dashed lines. The blue shift of these edges after annealing is clear. Amorphous samples A and 7 clearly show broader features compared to the other annealed samples. Sample C (V-N-TiO_2 thin film) shows broader features compared to its V doped counterpart B, indicating a more disordered local structure.

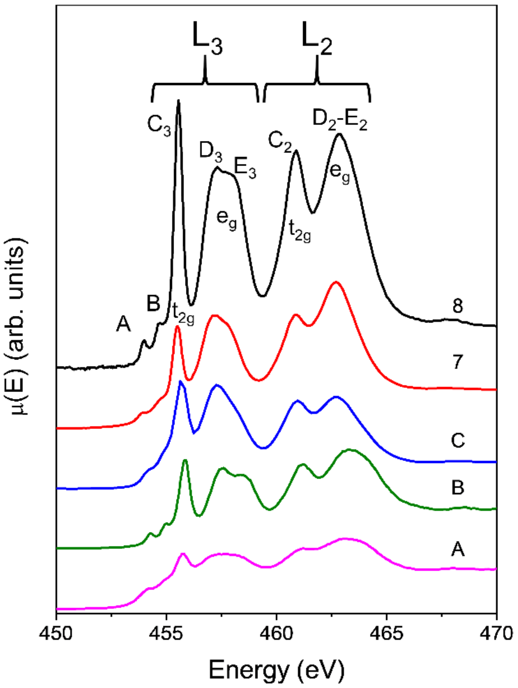

Figure 2.8: Ti $L_{2,3}$ edge XANES spectra for nanoparticle and thin film samples. In both cases the annealed samples show sharper features. The V-N-TiO_2 sample C thin shows broader features than its V-doped equivalent sample B.

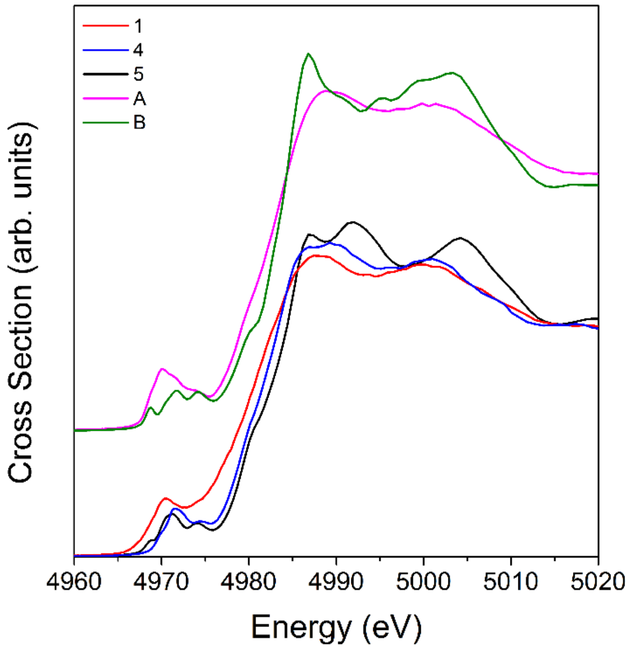

Figure 2.9: Comparison of the Ti K edge of crystalline and amorphous samples. The edge position shifts to higher values after the thermal treatment

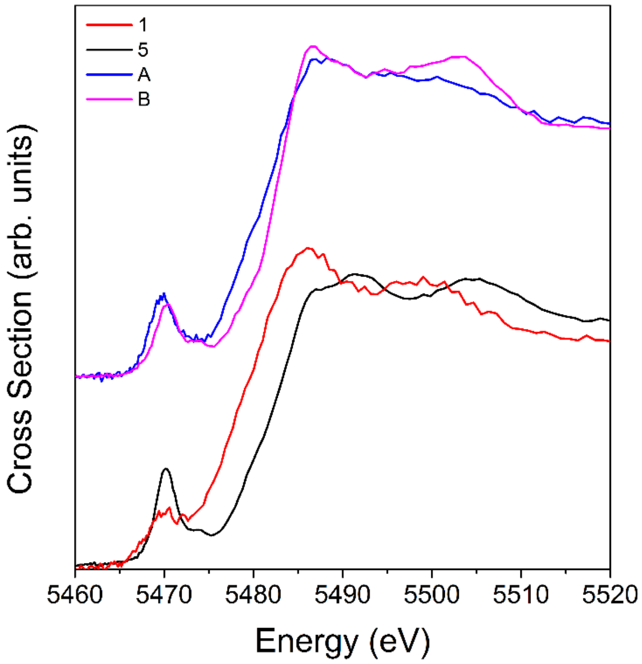

Figure 2.10: Effects of thermal treatments at V K edge. Untreated samples show broader features and lower V oxidation.

2.3.5 LOCAL STRUCTURE OF INVOLVED ATOMIC SPECIES

In this section, the local environment of all the involved atomic species is determined starting from the XANES spectra of reference compounds and using theoretical spectra generated from known models.

2.3.5.1 TITANIUM

An accurate study of the Ti environment is an important basis for the understanding of charge transfer processes, which will be described in the following. A qualitative analysis of the pre- and main-edge regions of the XANES spectra can reveal precious information about the chemical environment surrounding Ti cations. By inspection of the data collected at Ti K edge (Figure 2.11) and comparison with the existing literature[19,91–95] it is possible to reach several qualitative conclusions.

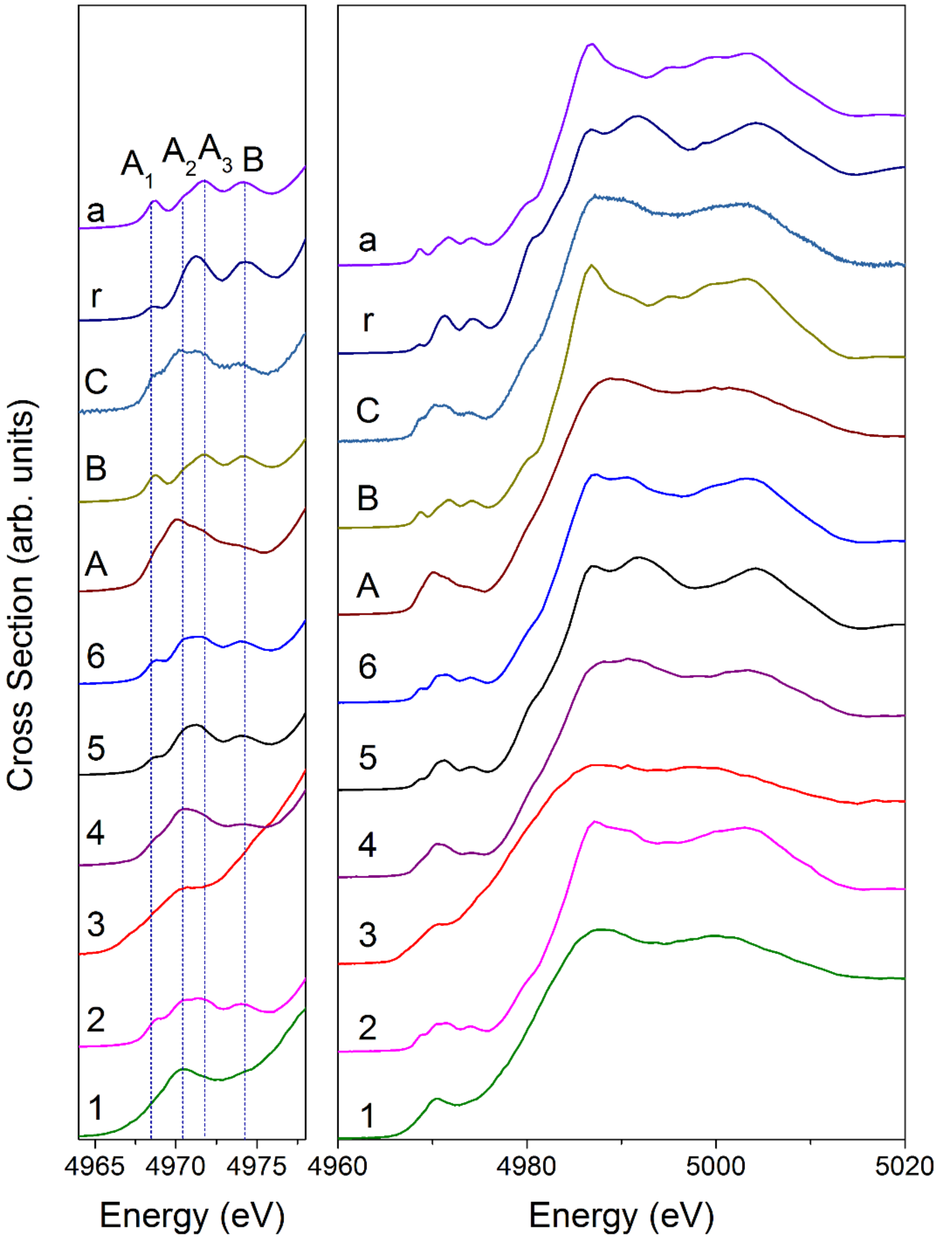

Figure 2.11: Comparison of the Ti K edge XANES spectra. In the left panel, a zoom of the pre-edge region.

Annealed samples exhibit line-shapes reminiscent of crystalline rutile or anatase. Thin films, in particular B, show an anatase-like line-shape, but C the V-N co-doped sample shows also traces of rutile features and a broader line-shape maybe due to a non-perfect crystallization.

Nanoparticle samples, in general, show a mixed structure of rutile and anatase. Sample 4, which was annealed at 350 °C, has broader features compared to the others, indicating a poorer degree of ordering. The remaining samples, annealed at 400 °C, exhibit lineshapes that are never identical to rutile or anatase; however, it is noted that sample 2 is more similar to anatase and sample 5 to rutile. These observations related with the deposition rates listed in Table 2.1 confirm the relation between deposition rate and relative fraction of rutile and anatase mentioned above. Sample 6, containing a higher V concentration shows pre-edge features similar to rutile but an intermediate main edge line-shape. In all these cases, the A_2 pre–edge component is more intense than in crystalline oxides; this, according to some papers in literature can indicate the presence of under-coordinated Ti cations on the nanoparticle surface.[92,96]

Since Titanium is a majority component in the sample composition it was possible to record high quality EXAFS spectra, which were used to perform a precise analysis of the structural changes induced by V doping. In Figure 2.12 are reported the magnitudes of the Fourier Transform of EXAFS oscillations of annealed nanoparticle samples, together with anatase and rutile reference compounds. Spectra for amorphous samples are not reported because the lack of order is reflected in an almost featureless EXAFS region, making the fit with a theoretical model completely pointless and unfeasible. The Fourier transforms were performed in the k range from 3.5 to 11 $Å^{-1}$with a k^3 weight. A similar comparison is shown in Figure 2.13 where the $\chi(R)$ signal of two crystalline thin films with different doping concentration is compared to that of anatase.

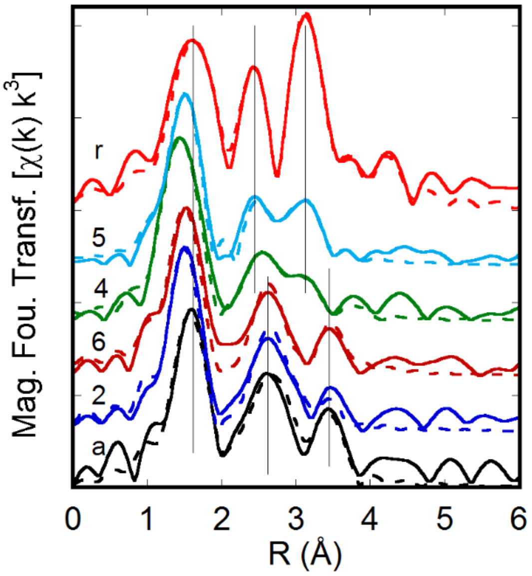

Figure 2.12: Magnitude of the Fourier Transform of Ti K-edge EXAFS spectra. Solid and dashed lines represent experimental spectra and best fits, respectively.

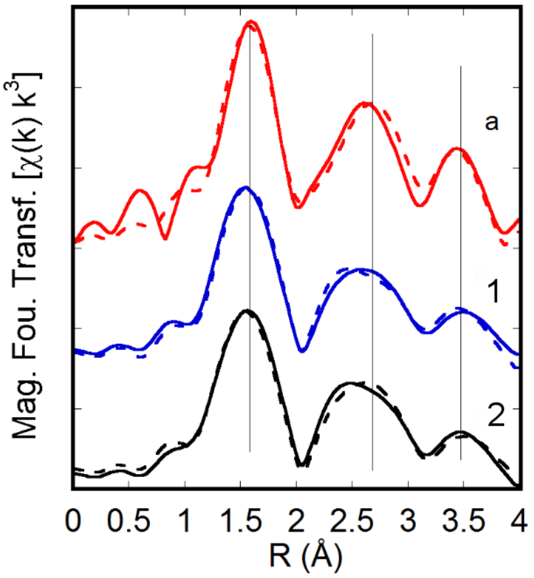

Figure 2.13: Magnitude of the Fourier Transform of Ti K-edge EXAFS spectra of the V-TiO_2 crystalline thin films with different V content (1= 2.4 at. % V; 2= 4.5 at. % V), compared to reference anatase (a). The Fourier transform was performed in the range $k = 4.0 - 11$ Å^{-1}with a k^3 weight. Dashed lines represent best fits.

At a qualitative level, it can be noticed that the spectra of samples are relatively similar and look like those of rutile or anatase. This is completely comparable with the observation made on the XANES region. The first shells peak in all samples is found at a slightly smaller distance compared to the reference oxides. Crystalline thin films and nanoparticle samples 2 and 6 show a structure quite similar to anatase; Sample 4 and 5, instead resemble rutile, but with a significantly lower amplitude of the peaks in the region $\mathrm{R} = 2 - 4$ Å, an indication of increased structural disorder compared to the crystalline reference. Comparing spectra for samples 4 and 5 (annealed at 350 °C and 400 °C, respectively) it can be noticed that a higher annealing temperature correlates with an increase of the amplitude of the third peak.

For a quantitative analysis, the spectra of rutile and anatase were analyzed first. Based on the crystallographic structure the single (SS) and multiple scattering contributions to the fine structure oscillations were calculated using the FEFF code[34]. Using ARTEMIS[71] the spectra were fitted varying some parameters of the FEFF calculated paths. Those parameters were an energy origin shift, a single isotropic distance variation parameter and individual Debye – Waller (DW) factors for each path. Spectra for both samples were fitted in the range $k = 3.5 - 11$ Å^{-1}. The R range for fits for both types of samples was 1 to 4 Å. For both anatase and rutile phases only a few of the possible paths were necessary for a good fit. In Table 2.4 and Table 2.5 the degeneracies and the involved atomic shells of the useful paths used for anatase and rutile are listed together with the refined values of the fit parameters. The resulting fit signals are indicated with dashed lines in Figure 2.12 and Figure 2.13.

Table 2.4: Numerical results of fits for anatase and samples 2, 6 and thin films with different doping percentages. Numbers in brackets indicate uncertainties in best estimates.

			anatase		**2**		**6**		**2.4 at. % V Thin Film**		**B 4.5 at. % V**	
Path	**legs**	**N**	**R (Å)**	**σ² (Å²)**	**R (Å)**	**R (Å)**	**σ² (Å²)**	**R (Å)**	**σ² (Å²)**	**σ² (Å²)**	**R (Å)**	**σ² (Å²)**
O (1st/2nd)	2	6	1.9565 (99)	0.0055 (12)	1.9321 (96)	1.949 (11)	0.0050 (14)	1.948 (11)	0.0048 (14)	0.0045 (13)	1.948 (20)	0.0065 (19)

Ti (3rd)	2	4	3.055 (15)	0.0058 (12)	3.048 (12)	3.058 (15)	0.0055 (15)	3.050 (15)	0.0051 (15)	0.0078 (13)	3.061 (40)	0.0071 (20)
Ti (4th)	2	4	3.804 (19)	0.0040 (31)	3.720 (76)	3.690 (26)	0.0003 (26)	3.690 (25)	0.0007 (27)	0.0063 (34)	3.680 (76)	0.0058 (34)
O (1st/2nd) Ti (4th)	3	8	3.849 (20)	0.0075 (17)	3.780 (30)	3.797 (23)	0.0012 (23)	3.800 (23)	0.0017 (23)	0.0153 (41)	3.791 (18)	0.0038 (30)

Table 2.5: Numerical results of fits for rutile and samples 4 and 5. Numbers in brackets indicate uncertainties in best estimates.

			Rutile		**4**		**5**	
Path	**Legs**	**N**	**R (Å)**	**σ^2 (Å^2)**	**R (Å)**	**σ^2 (Å^2)**	**R (Å)**	**σ^2 (Å^2)**
O (1st/2nd)	2	6	1.9636 (74)	0.0080 (17)	1.946 (20)	0.0079 (38)	1.952 (13)	0.0075 (21)
Ti (3rd)	2	2	2.9656 (11)	0.0039 (18)	3.047 (40)	0.0059 (71)	3.040 (30)	0.0058 (37)
O (4th)	2	4	3.495 (13)	0.0000 (40)	–	–	–	–
O (5th)	2	4	3.568 (14)	0.0115 (18)	–	–	–	–
Ti (6th)	2	8	3.578 (14)	0.0095 (44)	3.60 (22)	0.021 (81)	3.556 (22)	0.015 (79)
O (1st/2nd) Ti (6th)	3	16	3.758 (14)	0.0015 (31)	3.69 (42)	0.001 (39)	3.66 (17)	0.000 (13)
O (7th)	2	8	4.091 (15)	0.020 (24)	3.866 (90)	0.000 (17)	3.819 (89)	0.008 (41)
O (9th)	2	8	4.584 (15)	0.0038 (29)	–	–	–	–

The path degeneracies were kept fixed at the values of the crystals since, due to the well-known high correlation with Debye – Waller factors, it was impossible to determine them independently with a reasonable uncertainty. For samples 4 and 5 some of the weak O contributions were not included, as their structural parameters could not be determined reliably.

For anatase – like samples, the DW factors for the Ti coordination shells are slightly higher than in the reference. For rutile – like samples, the same trend is found; sample 4, annealed at a lower temperature, has the highest DW for the Ti – Ti 6th coordination shell. This could be an indication of the limited size of ordered clusters generated with a non-complete annealing. The Ti – O first shell interatomic distances in the NPs are shorter than in the reference compounds by 0.01 – 0.02 Å. This, according to Chen et al.[96] is related to the shorter Ti-O bond length characterizing surface sites. In nanoparticles, where the surface to volume ratio is higher, this contribution becomes appreciable.

2.3.5.2 OXYGEN

The O K edge spectra were already reported in Figure 2.7, discussing the effects of the annealing on the low energy edges. In this section it will be proved, using *ab initio* simulations of the XANES region that the local structure surrounding O is always a mixture of those of rutile and anatase. The structures used as input for FDMNES were obtained from literature[18] while the settings used are the same described in section 2.3.3.

The simulated spectra are in complete agreement with several measurements of anatase and rutile K edges reported in earlier literature studies.[91,97,98] In Figure 2.14 the main features of those theoretical spectra are labelled according to the notation used by Wu et al.[97] It is possible to observe that the line-shape of thin film samples (indicated with capitals letters) are almost identical to the theoretical prediction for the absorption spectrum of an anatase crystal. The relative amplitude of the features C_1 and C_3 are comparable with those of the simulation and above all no C_2 feature is present. In nanoparticle samples, instead it is possible to highlight a higher concentration of rutile that significantly modifies the post-edge region. In general, apart from sample B that shows a very crystalline structure, it is possible to observe a significant broadening of the features also for thermally treated samples. This can be related to the fact that also annealed samples like C and 8 show a certain degree of disorder. Amorphous A and 7 samples are appreciably disordered but still show only the two typical anatase features that are however significantly broadened if compared to those of sample B.

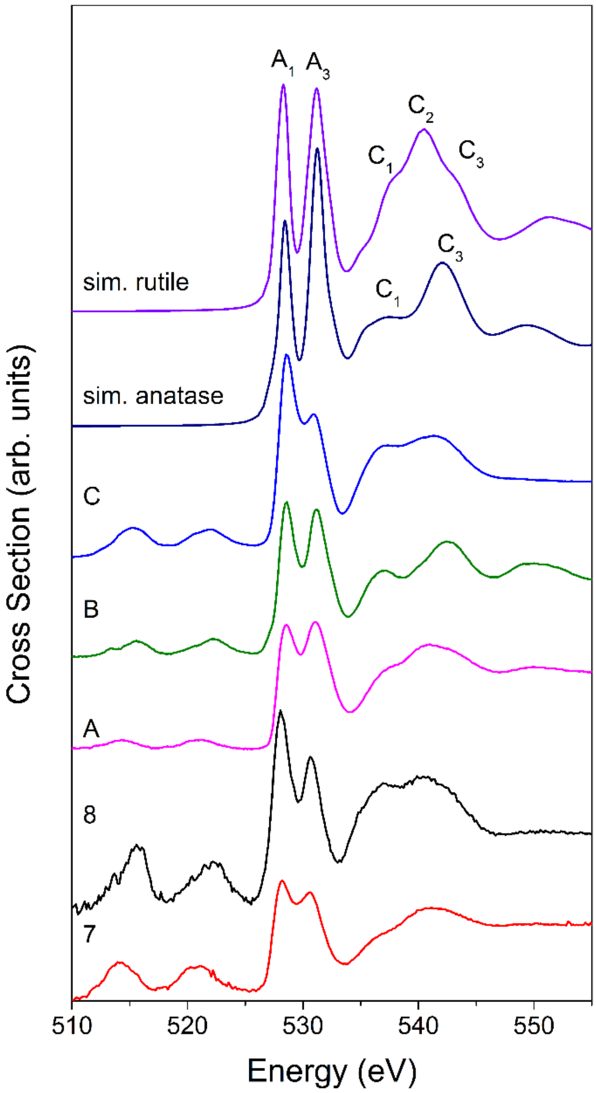

Figure 2.14: Nanoparticles and thin film O K edge spectra compared with theoretical spectra generated by pure anatase and rutile

2.3.5.3 VANADIUM

Being V one of the two studied dopants, the descriptions of its local environment will be one of the most important parts of this thesis. Determining the incorporation site of V in the TiO_2 matrix is fundamental to understand most of the properties of the doped system. A good and reliable set of coordinates can be the perfect starting point to theoretically predict the band structure, the charge density and even the optical properties of the sample.

As mentioned above the local structure was determined in two ways. The first one, relies on a phenomenological approach, while the second is based on rigorous *ab* initio simulations based on the models illustrated in section 2.3.2. The starting point for both interpretations, however are the V K-edge XANES spectra of nanoparticle and thin film samples reported in Figure 2.15.

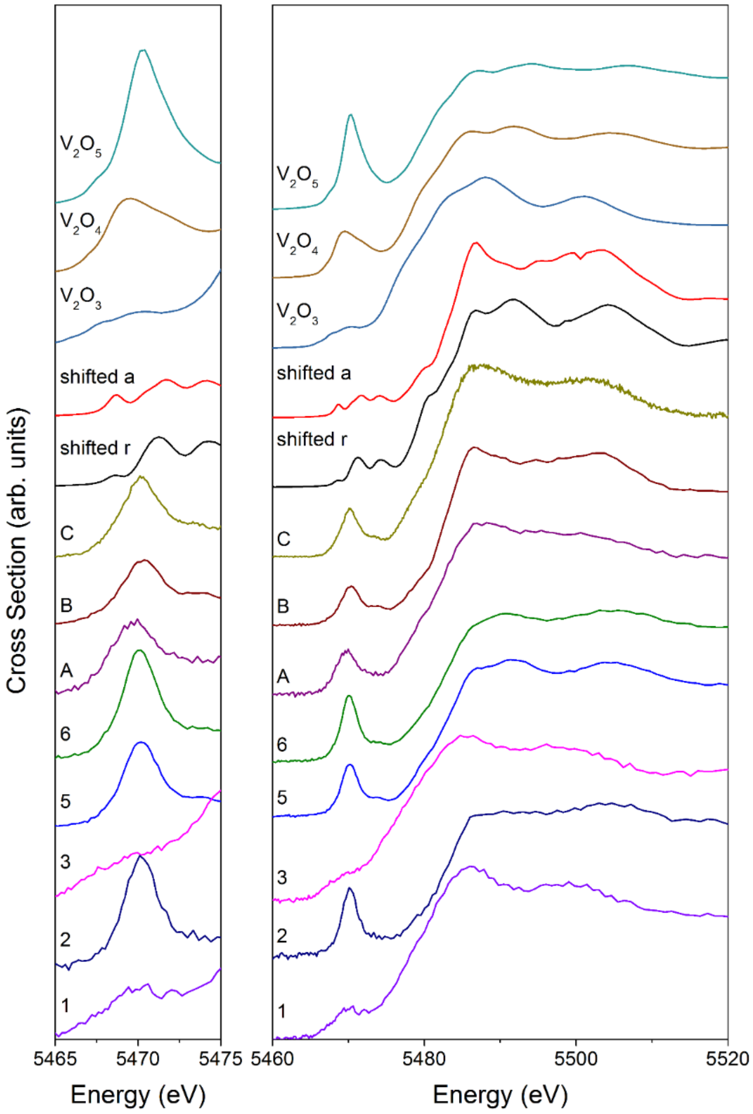

Figure 2.15: V K edge XANES spectra of nanoparticle and thin film samples compared to reference V oxides and shifted Ti K edge spectra of rutile and anatase reference samples.

Comparing Figure 2.15 and its equivalent at Ti K-edge (Figure 2.11) it is possible to observe some common characteristics. None of the doped samples spectra resembles the line-shape of V oxides, although the local structure of V_2O_4 is very similar to the rutile one (similar symmetry but shorter bond lengths).

Supposing a substitutional behavior of V, its local structure should be very similar to that of Ti cations. This implies that the post-edge region of Ti and V K-edge spectra should be comparable. In Figure 2.16 the V K edge XANES spectra for all sample are compared with those at Ti K edge shifted by 500 eV. The comparison between the V and shifted Ti spectra in the post-edge region indicates a close correspondence of the lineshape for most of the samples. This is a first indication that V substitutes Ti in the samples. For thin film samples, the agreement is full. Nanoparticle sample spectra, instead, show some differences between the two edges. In particular, sample 6 at V K-edge shows post-edge structures similar to those of rutile, while at Ti K edge it is clear the presence of a considerable fraction of anatase.

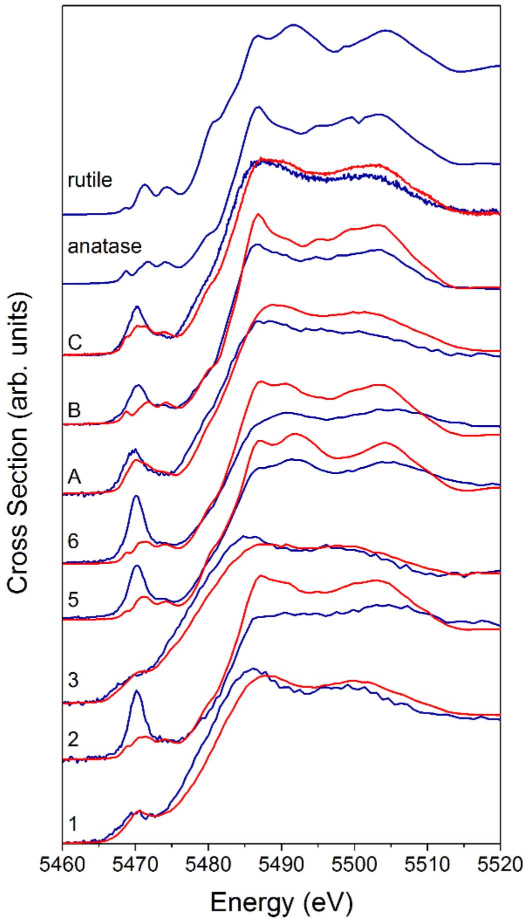

Figure 2.16: Comparison between V K-edge XANES spectra (blue) at V K edge and shifted Ti K edge spectra (red). Anatase and rutile shifted spectra are shown at the top.

A possible explanation for the absence of anatase features in the V K edge spectrum of sample 6 can be the thermodynamically favored formation of substitutional defects in rutile. Performing the structural relaxations showed in section 2.3.2 was also possible to give an estimation of the formation energy of the defects, that can be evaluate subtracting from the relaxed cluster energy the contribution that the single atoms give if isolated in a 15 Å simulation cube. For both substitutional defects, positive values of the formation energy were found. This mean that the processes are both thermodynamically unfavorite. However, the formation energy for V substitutional defects in rutile is only 0.74 eV while in anatase is around 1.0 eV. Similar values were also obtained by others in literature.[99] If the overall structure of the system is mixed it is thus probable that V incorporation in rutile will be favored.

To give a strong theoretical support to the substitutional hypothesis, FDMNES simulations were performed starting from the previously described Quantum Espresso relaxed models. Of course, simulations must be compared to those samples that clearly show a clear dominance of one of the two anatase or rutile phases. For this reason, only samples 5 and B will be considered. The first will be compared with the V_{Ti} r model, while the second with the V_{Ti} a and V_i models. The comparison is shown if Figure 2.17. It is immediately clear that the V_i model in anatase generates a XANES spectrum completely different from the experimental ones.

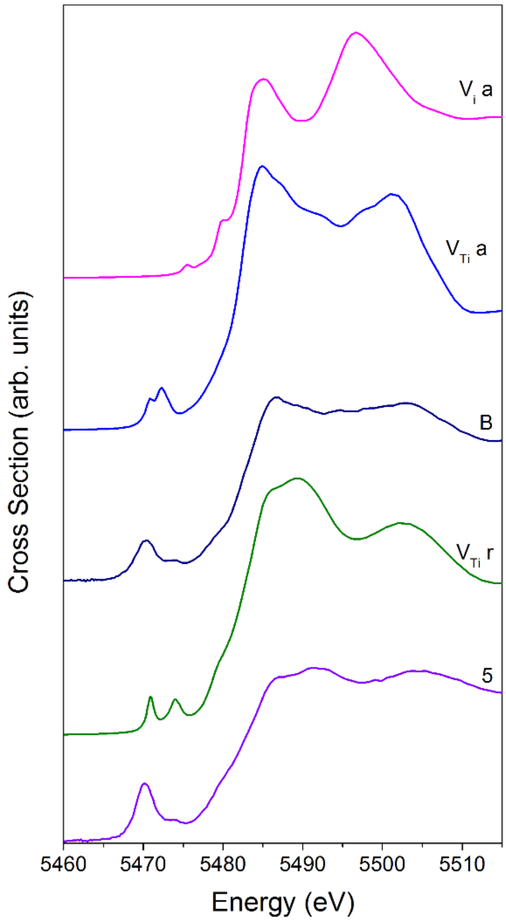

Figure 2.17: Comparison between XANES spectra of rutile-like sample 5, anatase-like sample B and simulated spectra obtained from Quantum Espresso relaxed models. “r” and “a” refer to rutile and anatase.

The substitutional models, well reproduce all the experimental features. This is a strong indication of the substitutional behavior of V in TiO_2, confirming what observed with the qualitative analysis.

To better understand the properties of V doped TiO_2 an important analysis to be performed is the determination of the oxidation state of the dopant. In the previous section the substitutional behavior of V was investigated. According to the FDMNES calculation, the charge localized on V atoms of the bulk for both rutile and anatase substitutional models is 3.9 *e*, suggesting a 4+

oxidation state. This behavior is also confirmed by others in literature,[100] and associated to the presence of donor deep levels in the TiO_2 gap.[62,99] V surface sites, however may attain the 5+ oxidation state, most stable under oxygen-rich conditions. In V-doped TiO_2 NPs prepared by chemical methods, the formation of V^{5+} vanadate surface-cluster species for V contents higher than about 5% was already reported in literature.[60,100] For the investigated sample, having a high value of the surface to volume ratio, the XANES spectra at V K edge will be the superposition of those related to surface and bulk sites. If the V oxidation state is different between the two regions it is reasonable to expect XANES spectra addressable to an intermediate oxidation state between 4+ and 5+.

Looking at the data, it is very difficult to clearly point out which is the dominant oxidation state for V. In several cases the XANES main edge position can be very helpful to identify the absorber's oxidation state. In this case however, as shown in in Figure 2.18, the main edge for TFs and NPs samples compared with those of V oxides is clearly shifted to higher energies. The local structure surrounding V in a TiO_2 matrix is then enough different from those of V oxides to generate completely different line-shapes. From Figure 2.18, however, it is still possible to get some information about V oxidation state focusing on the pre-edge region. It is very interesting to notice that both NP and TFs show a main peak centered almost at the same energy of the pre-edge feature of V_2O_5. This could be an indication of the presence of V^{5+} sites. The peak amplitudes, however are comparable with that of V_2O_4 suggesting a distorted octahedron local geometry very different from the V_2O_5 one. In conclusion, in the pre-edge region it is possible to highlight both V_2O_4 and V_2O_5 characteristics, suggesting that the system could be in an intermediate state. The interpretation given above with surface V^{5+} and bulk V^{4+} sites could be a reasonable explanation for this mixed behavior.

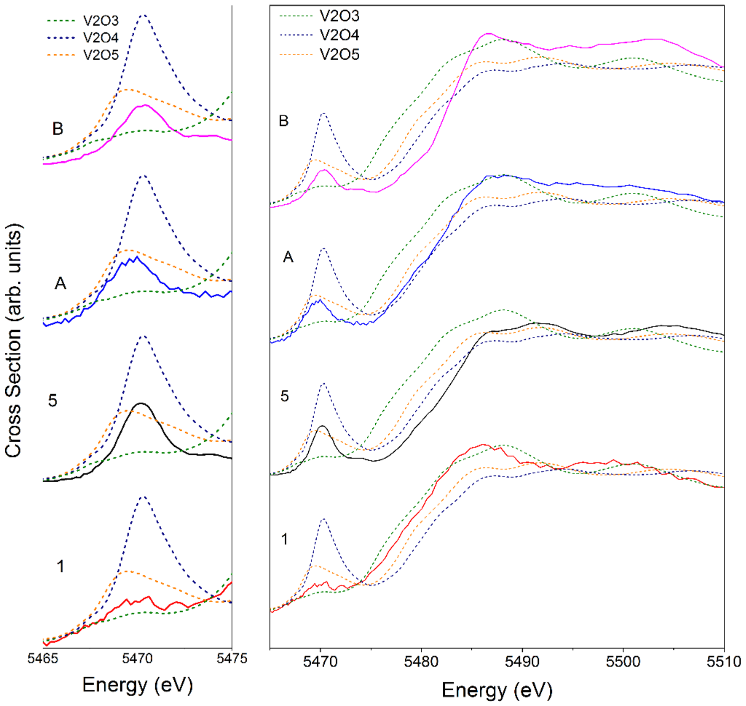

Figure 2.18: Comparison between reference V oxides (dashed lines) and selected samples. On the left a zoom on the pre-edge.

2.3.5.4 NITROGEN

The N K-edge XANES spectrum of the V-N co-doped thin film C, is shown in Figure 2.19. It is characterized by a very intense white line at about 399 eV (labeled B) with a weak shoulder at lower energies (labeled A). At higher energies, the spectrum shows three broad features, centered at 407.5, 412.5, and 417.5 eV and labeled C, D, E. It is immediately clear that at least for the features A and B the spectrum does not resemble that at O K edge, shown in Figure 2.7, but the relative intensities of the C and D features, resemble that of the anatase O K edge spectrum. This can suggest a substitutional configuration for N that replaces one of the oxygens in the TiO_2 structure. The number of possible configurations for the co-doped system, however is higher than the three used to study the V local environment. In the literature it is possible to find studies like that performed by Di Valentin et al.[90] indicating a possible interstitial behavior of V. In this thesis, the number of possible models tested is even higher, considering several interstitial configurations involving also N_2 dimers. In Figure 2.20 the theoretical spectra associated to the models described in section 2.3.2 are compared with the experimental spectrum.

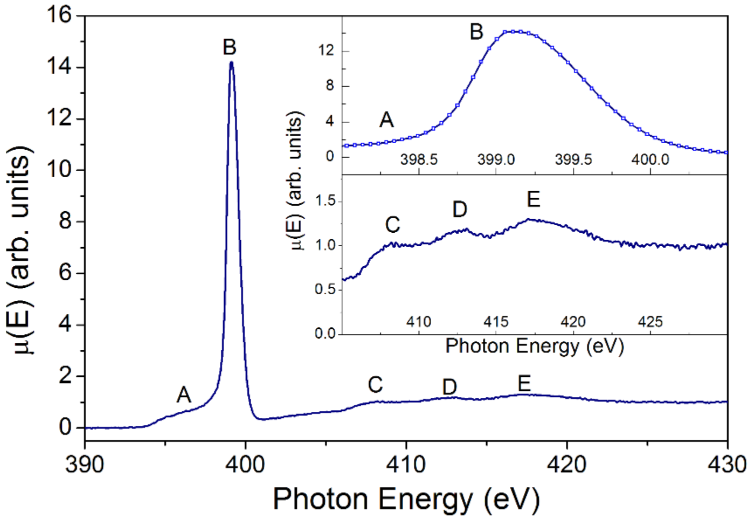

Figure 2.19: N K edge XANES spectrum of sample C. In the two insets are shown details of the features

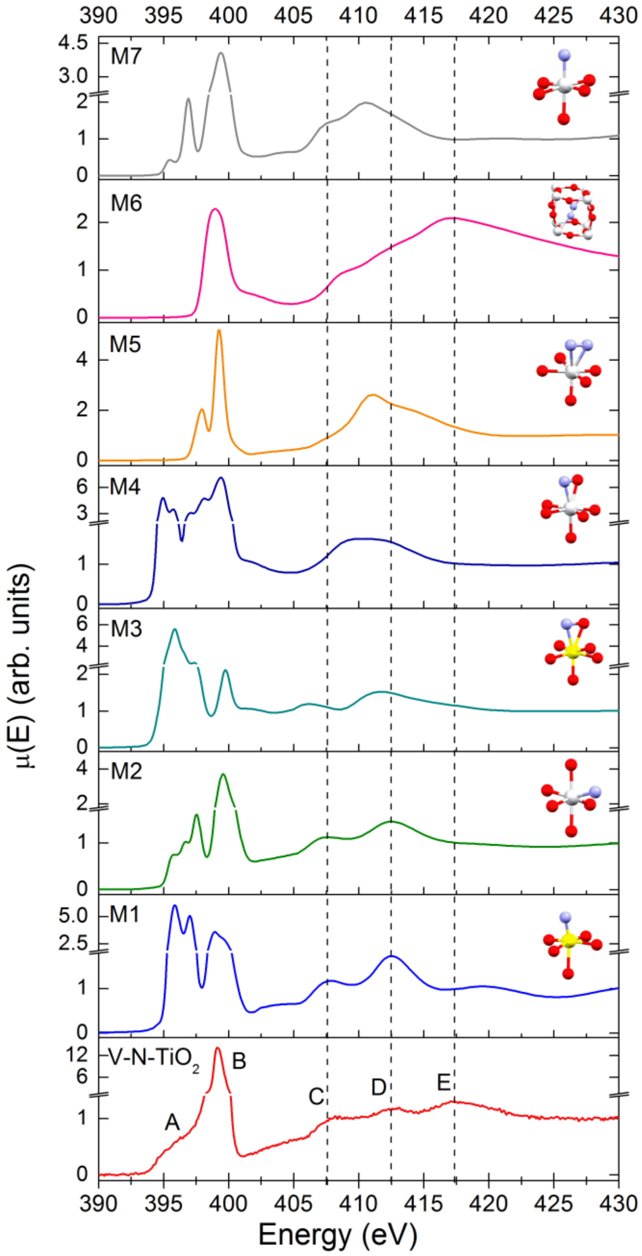

Figure 2.20: Comparison between experimental XANES spectrum of sample C (red line) and theoretical models M1-7. The dashed lines are a guide the eye related to the major features of the experimental spectrum.

It is immediately clear that none of the N models can describe exactly the experimental spectrum. Among the various theoretical line-shapes, however, the one best describing the experimental features from A to D is that of model M2. In this case N occupies one anionic site located far from the V substitutional defect. Models M1 and M3 representing respectively a N_O and a $(NO)_O$ configuration with one V as nearest neighbor can be excluded because the relative amplitude of features A and B is completely different from the experimental one. Moreover, models M4 and M5 representing a $(NO)_O$ and a $(N_2)_O$ configurations cannot describe almost any of the features. Model M7, a N_O configuration in rutile, shows a different structure at high energy, which is characteristic of rutile[101] and does not account for the C-E features. Interestingly, model M6, which represents a N_2 dimer in an interstitial site $(N_2)_i$, is the only one that accounts for feature E, and additionally predicts a single white line exactly at the energy position of B. The calculated N-N distance for this model is 1.11 Å, quite close to the interatomic distance in the free N_2 molecule (1.10 Å).

In the end, the only two possible configurations contributing to the experimental spectrum seem to be M2 and M6. The presence of two different N species is consistent with N 1*s* XPS measurements on similar samples[102], which show two main broad peaks at different binding energies (BE). The lower BE (394-396 eV) one can be associated with N_O, which is the most reduced species[103], while the higher BE (398-402 eV) is compatible with different defects: $(NO)_i$[103], $(N_2)_i$[104], and N_2 adsorbed at surface defects[105]. This conclusion is further strengthened by previous reports of a strong N K-edge white line in TiO_2 containing the $(N_2)_i$ defect, namely oxidized TiN[104] and TiO_2 annealed under NH_3[106]. On this basis, it is possible to interpret the intense white line as a distinct signature of the $(N_2)_i$ defect. This is in agreement with DFT calculations[106], which indicate that N atoms incorporated in the bulk of TiO_2 tend to recombine forming interstitial N_2 dimers. In addition, it is possible that N_2 molecules adsorbed on the surface of the growing film remain trapped during the sputtering process. It is important to stress that no gaseous N_2 bubbles were found within the film: if it were so, a vibrational structure would be clearly visible in the white line, as shown for instance in N-doped ZnO[107]. This is not case, as demonstrated by the zoomed view of the white line in Figure 2.19.

2.3.6 CONCLUSIONS

In conclusion, using XAFS it was possible to achieve a full description of the local environment surrounding V and N dopants and to observe the changes in the oxidation state of the involved species when crystallization is induced.

About the local structure of the dopants, the V substitutional behavior was proven, independently from the long-range structure of the samples. However, some discrepancies appear in mixed structure samples, where the incorporation in rutile, thermodynamically favored, dominates on the anatase counterpart.

On the other hand, N is found both in a substitutional and interstitial incorporation site. The peculiarity is that the favored interstitial configuration involves N_2 dimers, instead of single atoms. This behavior, however is justified by the fact that a single N is too reactive to give rise to stable interstitial configurations. An N_2 molecule, instead, can be easily trapped in anatase interstitial sites distorting the overall structure but finding a stable configuration.

3 OPTICAL MEASUREMENTS ON V-DOPED TIO$_2$ SAMPLES

3.1 Optical Properties of Doped Samples

In this section, the changes induced by V doping on the optical properties of TiO$_2$ will be described. As mentioned above, several studies have found that V induces states within the band gap of TiO$_2$. According to Umebayashi et al.[62] the incorporation of transition metal (TM) cations in substitutional sites of TiO$_2$, generates a narrow band of partially-filled intra-gap states. According to the *ab initio* calculations they performed for V, these levels should be located just below the conduction band as shown in Figure 3.1 in which the electronic density of states (DOS) is reported. The density of state of V doped TiO$_2$ shown in Figure 3.1 is also confirmed in a more recent paper by Patel et al.[10] Osorio-Guillén et al.[99] also predicted the intra-gap levels, highlighting that V cannot directly inject electrons in the TiO$_2$ conduction band like other dopants (Ta and Nb). This is experimentally confirmed by the fact that, after doping with V, the system is still an insulator. The expected consequence of doping is an enhancement of the absorption coefficient in the visible range, in which undoped TiO$_2$, because of its wide bandgap ($\approx 3\ eV$), cannot absorb. It must be mentioned that in a real nanoparticle (NP) several defect states localized on the surface or in the bulk (e.g. due to vacancies) may exist and can play an important role in charge trapping phenomena.

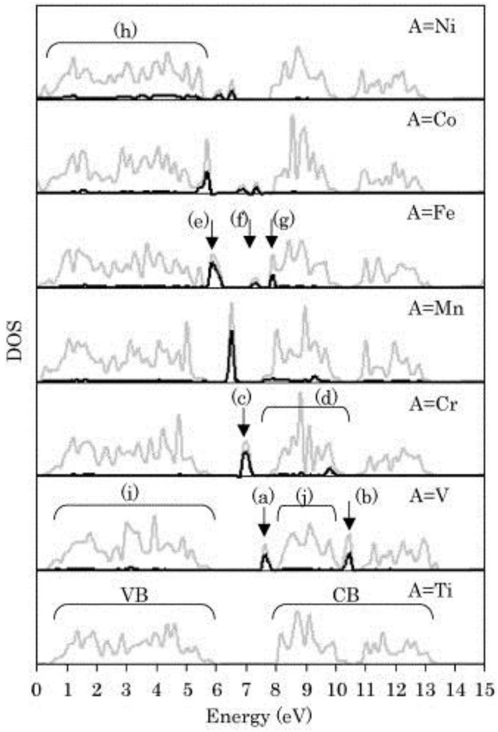

Figure 3.1: Electronic DOS for TM doped TiO$_2$ (from reference 62).

Measuring the UV-vis absorption spectrum of doped and undoped TiO$_2$ samples it is possible to identify the differences introduced by V incorporation. Standard transmission measurements of the absorption spectrum are impossible because of the strong scattering arising from the high surface roughness. For this reason, diffuse reflectance measurements were performed using a Perkin- Helmer, lambda 45 spectrometer. The absorbance spectra plotted in Figure 3.2

were obtained from the measured total reflectance ones using the Kubelka-Munk theory.[108] Clearly, V doping causes an enhancement of the absorbance in the region between 350 nm and 550 nm. A similar trend can be also found in literature for similar samples.[109] The samples used for these measurements are the same described in section 2.

The increased absorption in the visible range may be due, in principle, to various electronic transitions (e.g. from the valence band to empty gap states, from filled gap states to the conduction band, a combination of both, not to mention the role of surface states). Furthermore, the initial absorption is accompanied by complex relaxation and possibly charge trapping processes which play an important role in photocatalytic processes. Precious information on this can be obtained with optical pump and probe experiments with time resolution of a few 10 fs which will be described in this chapter. We note, however, that despite the advantages of time resolved optical spectroscopy, a direct determination of the involved atomic species, is impossible. In section 4 a differential illumination x-ray spectroscopy study is reported, which, due to the chemical sensitivity, will provide important new information on this issue.

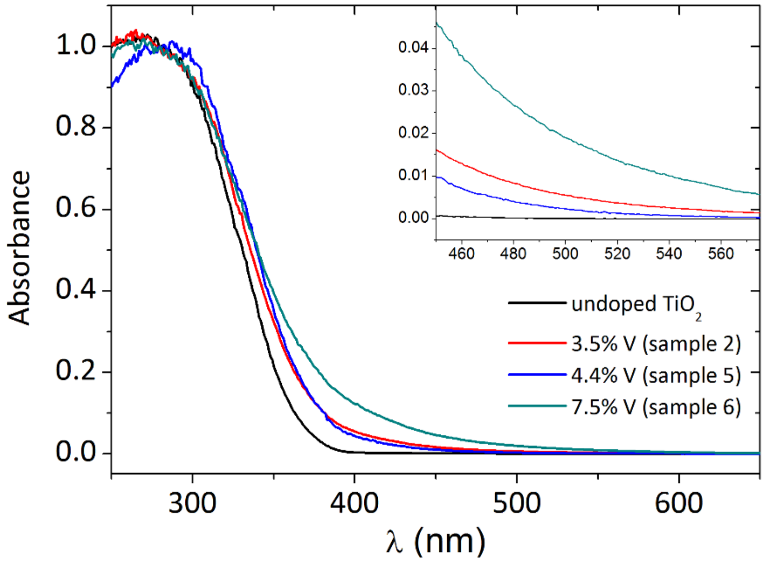

Figure 3.2 UV-vis absorbance of V-doped and undoped TiO_2 NPs, obtained by applying the Kubelka-Munk function to diffuse reflectance spectra and normalized to unit value at 280 nm.

3.2 ULTRAFAST TRANSIENT ABSORPTION SPECTROSCOPY MEASUREMENTS

3.2.1 SAMPLES

Samples for the transient absorption experiments were grown via gas phase condensation. Details about the deposition technique were already described above in section 2.1.2. The chosen samples show a very similar crystal structure as confirmed by the diffraction patterns shown in Figure 3.3. One of them, labelled as V-TiO_2 is doped with V, while the other is used as a reference. The V atomic fraction defined as the relative amount of V ions referred to the total number of cations, estimated with EDX, for the doped sample was 3.0 ± 0.5 at. %.

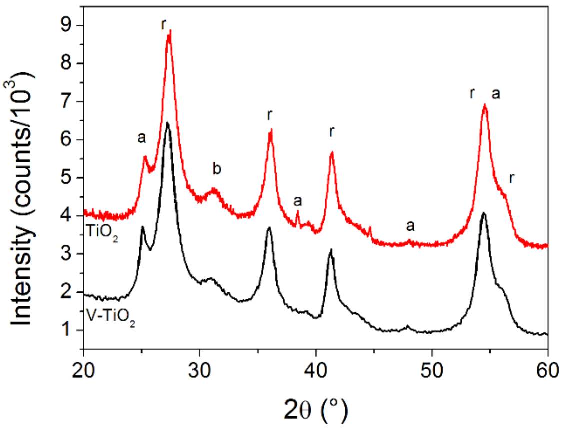

Figure 3.3: XRD patterns for doped and undoped TiO_2 samples. Features related to rutile anatase and brookite are respectively indicated with letters r, a and b. For both samples the overall structure is mainly rutile.

To perform the TA measurements, the doped and undoped TiO_2 nanoparticle samples were suspended in a solution of bi-distilled water and acetic acid in 70:30 proportions. Acetic acid is known to be an efficient surfactant useful to obtain stable suspension of TiO_2 nanoparticles.[110] The concentration of the suspension was 1mg/ml for both samples. The homogeneous suspensions were deposited on UV quartz substrates via drop casting. The thickness for the two thin films obtained was around 10 µm.

3.2.2 Experimental Setup

For the ultrafast transient absorption spectroscopy measurements, the experimental apparatus present at Consiglio Nazionale delle Ricerche- Istituto di Struttura della Materia (Rome) was used. The apparatus is equipped with a Ti:Sa Vitara-T mode locked Oscillator emitting 20 fs pulses with an 80 MHz repetition rate. The fundamental wavelength is 800 nm and the emitted power is 550 mW. The oscillator is coupled with a Legend Elite HE+ regenerative amplifier that lower the repetition rate to 1 kHz, but increases the power to 4W at 800nm. The pulse duration after this amplification process is increased to 35 fs. To produce pump pulses in a wide range of wavelengths (240-20000 nm) the system can be coupled with an OperA-Solo Optical Parametric Amplifier. This was used only for those measurements performed with 530 nm pump pulses. The 400 nm pump was obtained exploiting the second harmonic of the oscillator. The white probe pulse (350-1600 nm) was obtained by focusing the 800 nm laser o crystal. The differential signal defined as the difference between pumped and unpumped absorption spectra is collected with a fast transient absorption spectrometer.

3.2.3 Results

3.2.3.1 330 nm Excitation

Since it is reasonable to expect that V incorporation can lead to a modification of the charge carrier dynamics at wavelengths at which undoped TiO_2 has a high absorption, the first step in the investigation was performed with an excitation wavelength $\lambda_e = 330\ nm$. Measurements at sub band gap wavelengths will be reported in the next sections. The starting point for the investigation of doping-related changes is of course a good knowledge of the behavior of undoped TiO_2. In the literature, there are several examples of pump and probe experiments performed on TiO_2 NPs exciting the samples above the band-gap.[111–115] In some of those papers,[112–114] it was possible to associate specific spectral features of the transient absorption spectra to the presence of trapped and free photo-generated charge carriers by using so called "scavengers", that are chemical species that are able to absorb selectively trapped holes or electrons on the NPs' surface). According to Yoshihara et al.[112], in particular, the transient absorption spectrum of undoped TiO_2 NPs is composed by three positive features as shown in Figure 3.4. The feature centered between 400nm and 500nm is related to holes trapped on the NP surface in hole trap (HT) states while the broader peak centered between 700nm and 800nm is related to electrons trapped in electron trap (ET) states, also on the NP surface. HT and ET states are energetically within the band gap. Superposed to the previous features there is a broad polynomial component due to the intra-band transition of free electrons.

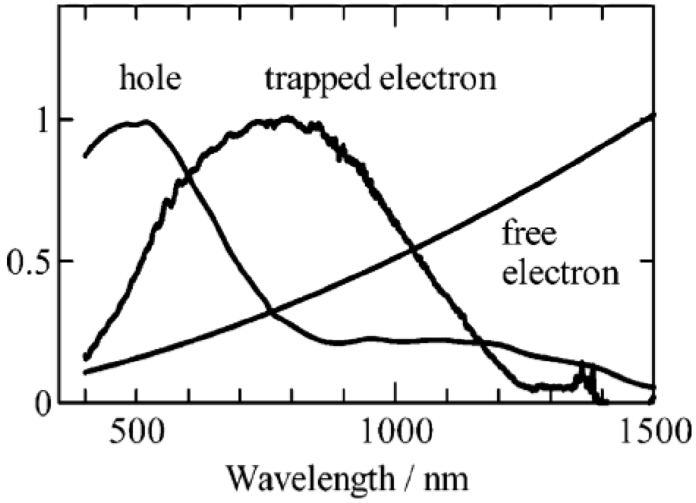

Figure 3.4: Identification of the origin of the spectral components of transient optical absorption spectra of TiO_2 NPs. From reference 112.

Based on the quoted literature, the electron and hole transitions responsible for these spectral features are now described. The initial absorption of $\lambda_e = 330\,nm$ light (the "pump") causes transitions of electrons from the valence band (VB) to the conduction band (CB). Electrons in the CB and holes in the VB subsequently relax and are trapped in ET and HT states within the band gap. Specifically, hole trapping is due to the formation of O^-or O_3^- according to the following equations:[114,116,117]

$$O^{2-} + h^+ \rightarrow O^- \qquad 3.1$$

$$O^{2-} + O_2 + h^+ \rightarrow O_3^- \qquad 3.2$$

The excess of holes (electron depletion) in the HT states leads to the transient positive absorption due to electron transitions from the VB to the HT at 400 nm. This process is illustrated in Figure 3.5a. Likewise, electron trapping is due to the process:[118]

$$Ti^{4+} + e^- \rightarrow Ti^{3+} \qquad 3.3$$

The excess of electrons in the ET states leads to the transient positive feature due to electron transitions from the ET to the CB at 750 nm, as shown in Figure 3.5b. Superposed to these two peaks there is a polynomial contribution ($\propto \lambda^n$) due to the intra-band transitions occurring in the valence and conduction bands (Figure 3.5c).

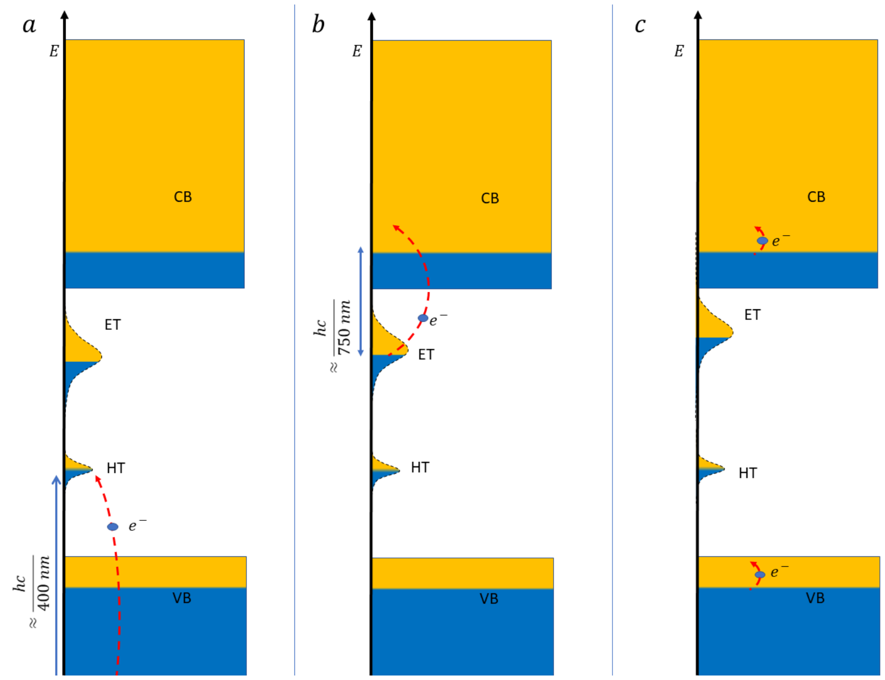

Figure 3.5: Electron transitions made possible after laser excitation. (a) filling of trapped holes on the nanoparticle surface, (b) transition of trapped electrons on the Np surface to the CB, (c) intra-band transitions in VB and CB

Pump and probe experiments on doped TiO_2 systems have also been reported in the literature, always using above bandgap excitation ($\lambda_e \approx 350$ nm). The most recent study is of Sun et al.[119], who studied Co and W doped TiO_2 multilayer systems and observed that doping increases the speed of the decay of the feature at 730 nm related both to free and surface trapped electrons. This study was performed with a time resolution of 120 fs, very similar to the one used for the current experiments. Previous studies on V-doped systems were performed by Choi et al.[120] focusing only on the trapped electron spectral component. The time resolution achievable with their setup, however, was not good enough to sample the first ps evolution, but they observed that also in the μs timescale, V doping induces faster recombination dynamics compared to undoped TiO_2.

The results shown in the following paragraphs agree with these previous initial studies confirming faster decay dynamics for the doped samples also in the fs timescale. However, they allow new physical insight due to the use of variable wavelength excitation and the observation of a correlation between the electron and holes dynamics, made possible by the advanced characteristics of the apparatus.

We will initially describe TA measurements with $\lambda_e = 330\ nm$, which were performed also to reproduce literature data on undoped TiO_2, as a check. The excellent time resolution of the apparatus (≈50 fs) can give detailed information on the ultrafast dynamics after the laser excitation. The wide spectrum used for the probe pulse made it possible to originally correlate the time evolution of the spectral features due to electrons (free and trapped) and trapped holes. In Figure 3.6, 2D maps of the transient signal as a function of the probe wavelength and time delay are shown. The exciting laser was operating with an intensity of 5 μJ/pulse.

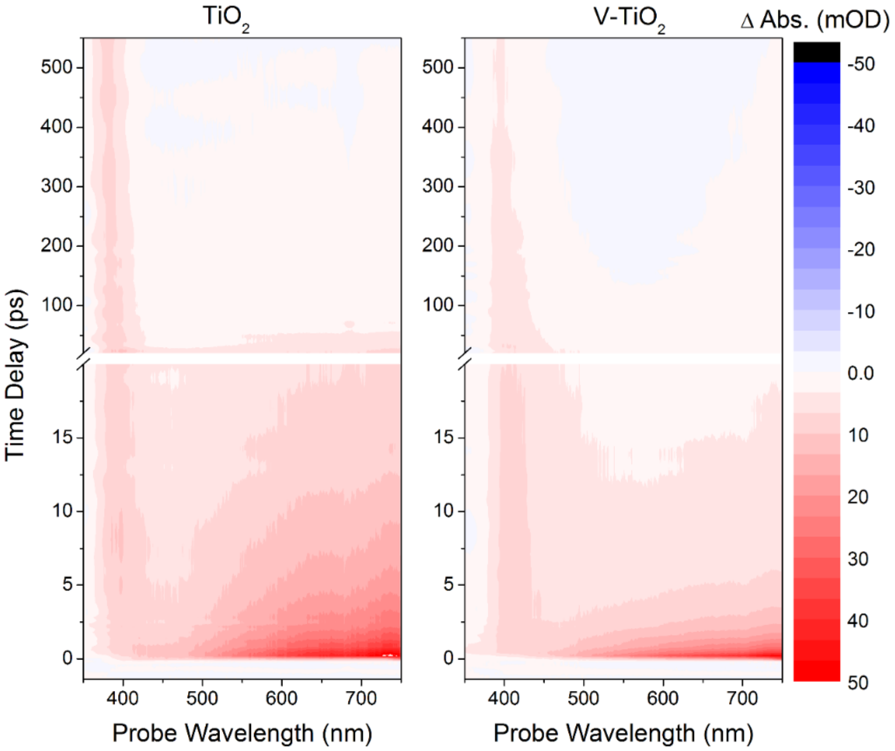

Figure 3.6: 2D maps of the differential signal generated by undoped TiO$_2$ (left) and V-doped (right) NPs with 330 nm excitation.

Looking at the maps, it is immediate to notice the presence of broad positive signals for both samples. In particular, it is possible to identify a long-living excitation around 400 nm and a faster decaying signal appearing between 500nm and 750 nm. To have a clearer idea about the features characterizing the transient spectra, some spectral traces obtained at different time delays are shown in Figure 3.7. The line-shapes for doped and undoped TiO$_2$ samples are very similar. Both show the typical features reported in the literature on undoped TiO$_2$, as described above. The only difference introduced by V doping, also visible in the maps in Figure 3.6 is a small shift of the trapped holes peak to higher wavelengths. For undoped TiO$_2$ nanoparticles, this feature is centered at around 390 nm while for the doped particles its position is shifted to 400 nm.

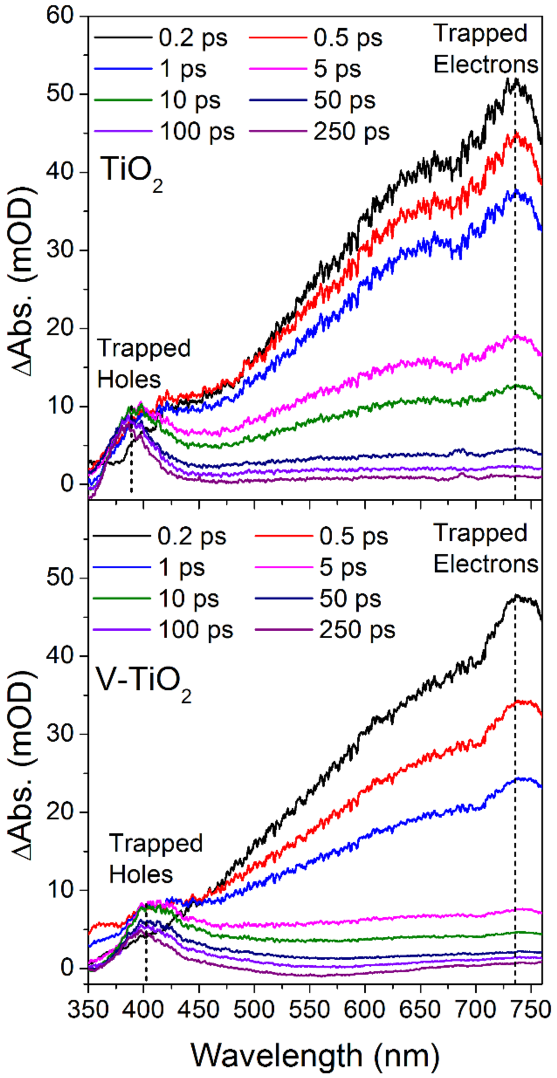

Figure 3.7: Transient absorption spectra of doped (bottom) and bare TiO2 (top) nanoparticles at different time delays.

The main differences introduced by V doping, however, are in the time domain: doping clearly induces a faster evolution of all the spectral components. In particular, in Fig. 1.8a the time dependence of the transient absorption signal at 730 nm are reported. A quantitative fit of the two decay traces in the ultrafast regime is possible with the function:

$$A(t) = A_\infty + C_1 e^{-\frac{t}{\tau_1}} + C_2 e^{-\frac{t}{\tau_2}} + C_3 e^{-\frac{t}{\tau_3}} - \frac{t}{\tau_4} \qquad 3.4$$

The function is a sum of three decay processes plus a linear term that can be considered as the first term of the series expansion of a very slow exponential decay. This formula is in agreement with the kinetic model used by Rothenberger et al.[115] to describe TA of undoped TiO2 under UV excitation. According to them, e-h recombination is the main responsible for the differential signal attenuation. They demonstrated that the recombination rate of photo-generated e-h couples is directly proportional to x^2 where x is the initial number of photo-generated couples. This proportionality is due to the x^2 possible interactions of x electrons with x holes. They found that the general expression describing the differential signal $A(t)$ is given by the following expression, where A_0 is the initial amplitude of the signal and k the recombination probability of a single e-h couple:

$$A(t) = \sum_{n=1,\ n \in N}^{\infty} C_n(A_0)e^{-n^2k(t-t_0)} \tag{3.5}$$

According to their interpretation this formula can be simplified in two limit cases. Since the c_n coefficients depend on A_0, for very small values of this parameter they demonstrated that 3.5 can be approximated with single decaying exponential, while for very high values of A_0 the behavior is the one shown below:

$$A(t) = \frac{A_0}{1 + A_0kt} \tag{3.6}$$

In all the intermediate cases the decay associated to the recombination process can be described as a sum of decaying exponentials, but it is clear, looking at the limit cases, that higher is the number of initial e-h couples and faster is the decay.

As shown in Figure 3.8, the agreement between experimental data and fits is very good. This is a first indication that the recombination model described above can well reproduce the differential signal decay in the region around 730 nm. According to the results obtained by Tamaki and co-workers,[113] however, electron-hole recombination is not the only possible decay channel for photo-generated electrons. With this assumption they explained the physical origin of the asymmetry between the lifetimes of the features at 730 and 400 nm. According to them, some of the surface trapped electrons can migrate in the shallow levels of the bulk and decay to very localized deep levels always in the bulk where they remain trapped. This small fraction of electrons cannot easily recombine with surface trapped holes, explaining the long living signal at 400 nm. On the other hand, after the fast e-h recombination no signal can be detected at 730 nm because electrons in the deep levels of the bulk do not absorb in this energy range lying well below the shallow ones.

Focusing on the fits of the 730 nm time traces, it is possible to immediately highlight differences between doped and the undoped samples. Looking at the best fit parameters, listed in Table 3.1, it is clear that the major changes induced by V doping are in the three ultrafast dynamics characterized by decay lifetimes τ_1 and τ_2 and τ_3, while the linear contributions (due to even longer dynamics) are comparable. According to the above described interpretation the faster decay for the doped sample can be ascribed to a higher number of photo-generated charge carriers. This can be related to the massive injection in the conduction band of those electrons lying in the partially filled intra gap levels predicted in literature, as will be described in the following.

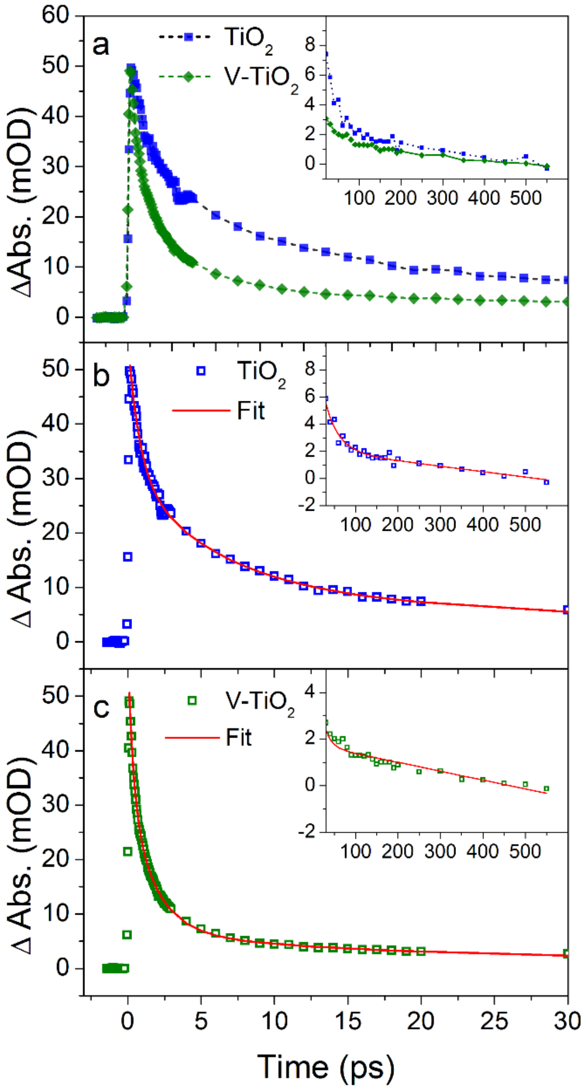

Figure 3.8: a): Comparison of 730nm time traces for doped and undoped TiO$_2$; b) fit of undoped TiO$_2$ 730 nm time trace; c) fit of V-TiO2 730 nm time trace.

Table 3.1: Best fit parameters for the electron dynamics peak.

Parameter	TiO$_2$	V-TiO$_2$
A_∞ (mOD)	2.1 (0.5)	1.8 (0.1)
C_1 (mOD)	20 (1)	19 (1)
C_2(mOD)	20 (2)	24.6 (0.9)
C_3 (mOD)	8 (2)	5.3 (0.7)
τ_1 (ps)	0.77 (0.07)	0.35 (0.02)
τ_2 (ps)	6 (1)	1.7 (0.1)
τ_3 (ps)	33 (11)	15 (3)
τ_4 (ps)	250 (60)	270 (40)

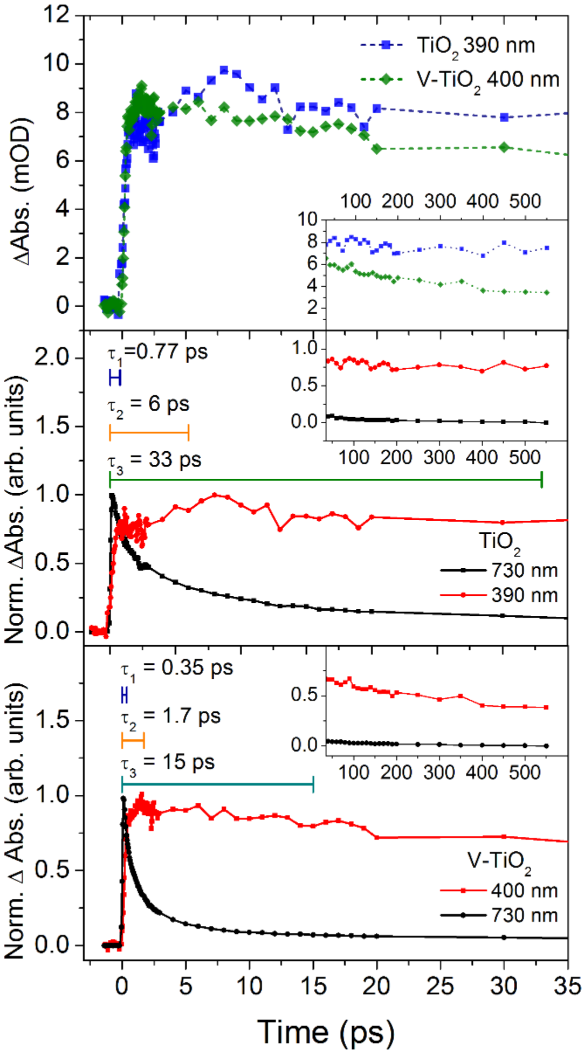

Figure 3.9: Top: Comparison between the trapped holes features time traces, Middle: Comparison between trapped holes and electron dynamics for undoped TiO2, Bottom: Same comparison for V-TiO2

By inspection of Fig. 1.9 an interesting correlation between the time dependence of the trapped electron and trapped hole signals is apparent. In fact, while the electron feature exhibits an abrupt rise and subsequent decay, the hole feature shows a gradual build up followed by a very slow decay, in both samples. In Figure 3.10 a zoom of the first 15 ps is shown to clearly highlight this correlation. The rise time of the hole feature is clearly comparable to the electron decay lifetime τ_1, while the maximum of the trapped hole component is achieved only after τ_2 when a slow decay starts. Trying to give a physical explanation of the interplay between electrons and holes a step by step approach will be followed in the following.

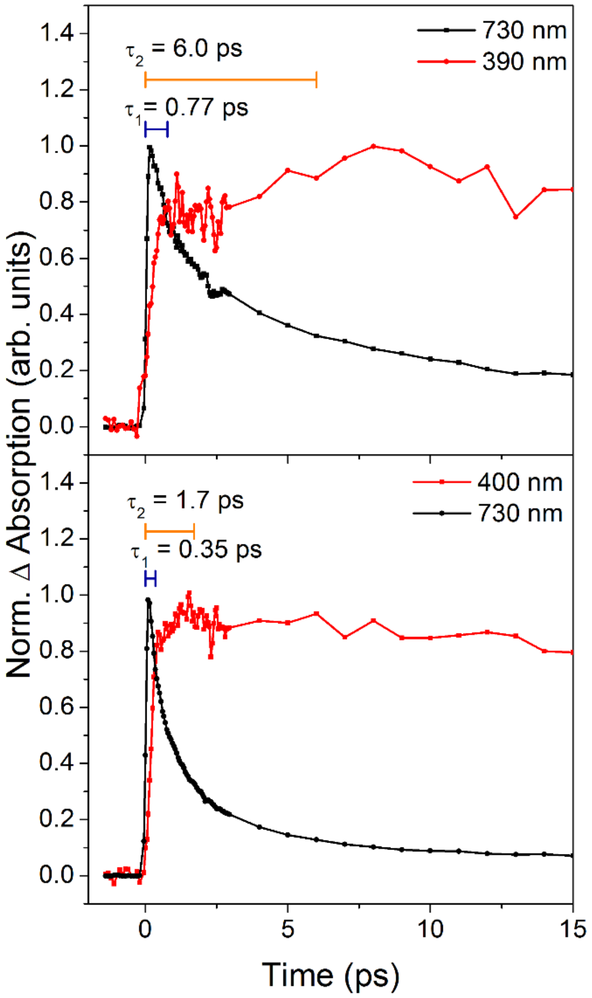

Figure 3.10: Comparison between trapped holes (red) and electrons (black) time traces for undoped (top) and doped (bottom) TiO2. Zoom of the first 15 ps.

The ground state electronic configuration before the laser excitation for doped and undoped TiO_2 is shown in Figure 3.11. The energy axis also pictorially separates bulk and surface states (left and right, respectively). According to Yoshihara et. al[121] in the intra-gap region, localized on the Np surface, there are filled and empty levels that act respectively like traps for holes and electrons. According to Tamaki et al.[122] in the bulk there are both shallow and deep levels. The former ones are partially overlapped in the energy with the surface trap levels for electrons. In the same paper they estimated that the electron decay from shallow to the deep levels has a lifetime $\tau \approx 500\,ps$. For this reason, the deep levels do not influence the ultrafast dynamics appearing in the first ps. In the doped system, according to the literature,[62,99] there will be also a narrow band of partially-filled levels localized in the bulk related to Vanadium $3d$ levels. These levels according to their calculations are located around 0.5 eV below the CB.

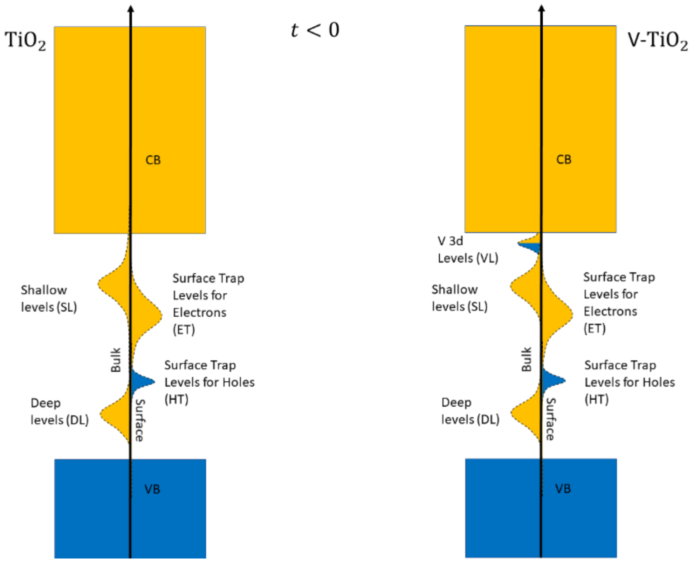

Figure 3.11: Ground state electronic DOS

At $t = 0$ the laser pulse of 330 nm wavelength excites the sample as shown in Figure 3.12. For undoped TiO_2 the only possible excitations are valence to conduction band transitions. In the doped system, instead, the bulk levels introduced by the dopant can be also excited. As mentioned by Umebayashi et al. electron transitions from the valence band to the V 3d levels are also possible. The gradual increase of the trapped holes signal at 400 nm suggests that electrons in the surface hole trap levels are not directly excited by the laser pulse, presumably due to a very small cross section. The time required for the hole signal to increase is related to hole diffusion time from the bulk to surface traps, as discussed below. Instead, the electron signal has an abrupt increase. According to Tamaki et al.[122] the shallow levels of the bulk are immediately filled after the excitation (i.e. the filling appears for time delays shorter than the time resolution of the experimental setup), which gives rise to the electron signal at 730 nm. Electrons in the valence and conduction bands can immediately undergo to intra-band transition, giving rise to the broad polynomial background in the transient spectra. No differential signal can be detected around 400 nm, because free holes need a certain time to diffuse from the bulk to the surface traps.

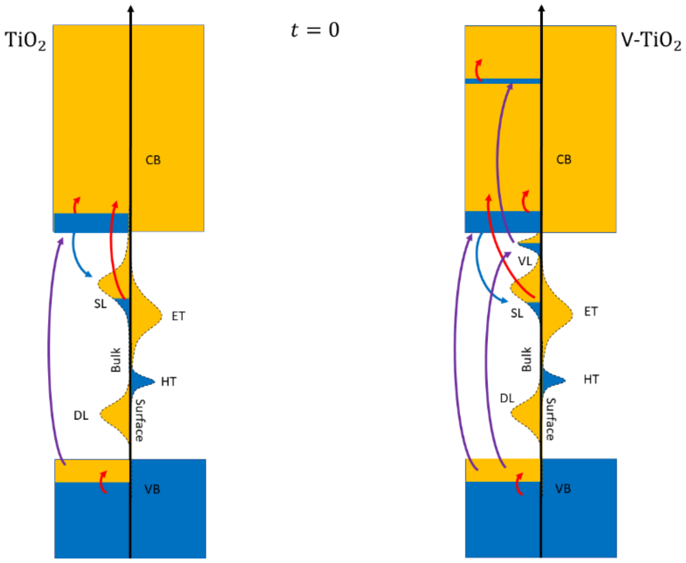

Figure 3.12: Excited electronic configuration immediately after the laser pulse. Violet arrows indicate the electron transitions triggered by the excitation pulse. The blue arrow, indicates the electron decay while red arrows indicate the transitions generating the transient signal.

τ_1 can be associated to the time needed for photo-generated charge carriers to diffuse from the bulk to the surface. According to Rothenberger et al.[115] an estimate of the diffusion time can be obtained using:

$$\tau_{diff} = \frac{r^2}{\pi^2 D} \qquad 3.7$$

where r is the nanoparticle radius and D the diffusion coefficient that, for TiO2, is $2 \cdot 10^{-2}\ cm^2/s$. Since the measured NPs have a diameter of around 10 nm the expected value for the diffusion time is around 1.3 ps, comparable with the values of τ_1 obtained for the undoped system. For V-TiO2 the τ_1 value is shorter suggesting a faster diffusion. The higher energy reached by those electrons originating in the intra-gap levels introduced by the dopant can be a possible explanation for the faster diffusion. A 330 nm radiation pulse can excite intra-gap electrons around 3 eV above the bottom of the conduction band. These hot electrons can propagate faster in TiO2 than those coming from the valence band reaching the surface in a shorter time. A cartoon picture of the processes happening between $t = 0$ and τ_1 is shown in Figure 3.13. Charge diffusion is not the only process appearing in the first ps. Electron-hole recombination between the conduction and the valence band starts immediately, producing a lowering of the electron signal at 730 nm. In the doped system a possible decay channel is also represented by the transition from the conduction band to the dopant levels. This, can contribute to the speed up of the decay in the doped system compared to that observed in the undoped one.

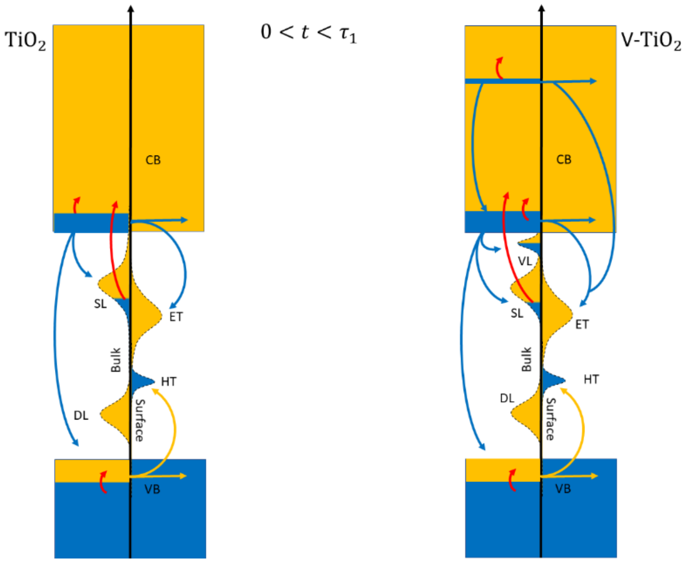

Figure 3.13: Electronic configuration between t = 0 and τ_1. Blue and yellow arrows indicate respectively the electron and holes relaxation dynamics. Red arrows, indicate the transitions generating the transient spectrum.

At $t = \tau_1$ the first trapped holes appear on the NP surface and consequently the signal at 400 nm increases. The electronic configuration and the transitions generating the differential signal are shown in Figure 3.14.

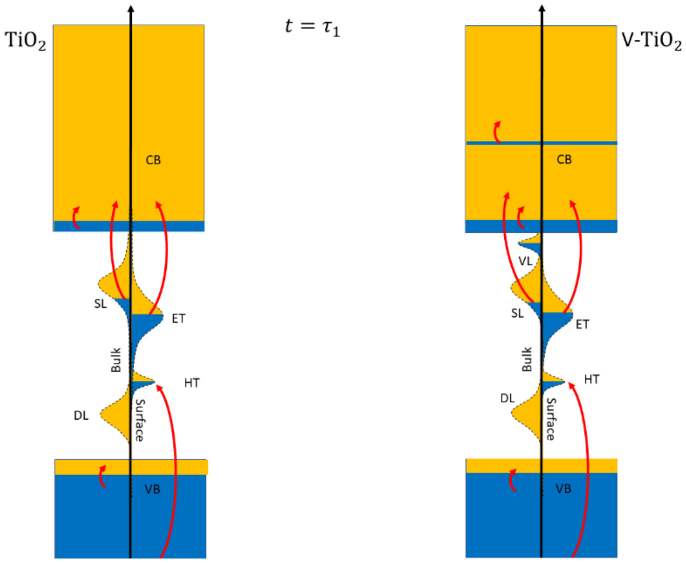

Figure 3.14: Charge configuration at τ_1. Red arrows indicate the allowed transition generating the differential signal.

Between τ_1 and τ_2 the hole component increases with a much lower slope with respect to $t < \tau_1$, while the electron one continues to decay. In Figure 3.15 a cartoon picture of the possible phenomena appearing in this time interval is shown. The hole component increases because of the diffusion of free holes from the bulk to the surface where they can remain trapped. However, electrons decaying from the conduction band, can also occupy the surface trap levels for holes, limiting the onset speed of the feature at 400nm. Although the increasing number of trapped electrons on the NP surface, due to the diffusion from the bulk, no increase in the 730 nm is visible because of the dominating e-h recombination process involving free holes in the VB.

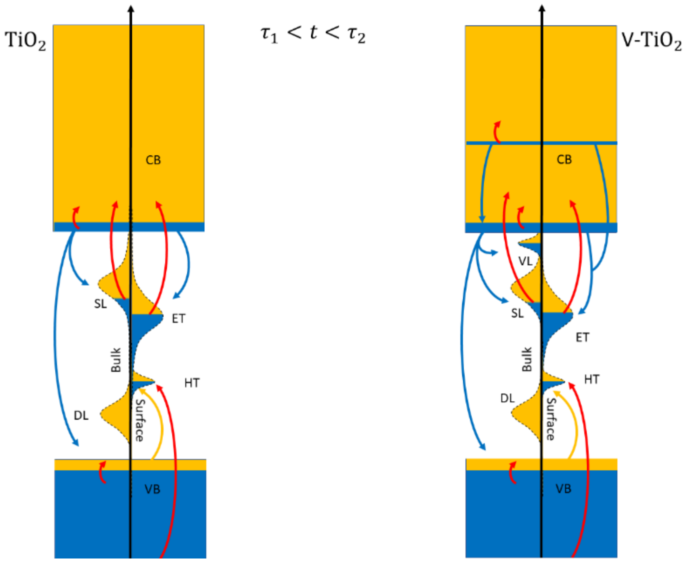

Figure 3.15: Electron configuration between τ_1 and τ_2. Blue and yellow arrows indicate electron and holes transitions. Red arrows indicate the allowed transition giving rise to the transient signal.

At $t = \tau_2$ (Figure 3.16) the feature associated to trapped holes starts to decay. This could be related to the almost complete recombination of electrons (free or trapped) with the valence band holes. Without propagating free holes, the population of those trapped on the NP surface cannot grow anymore and the recombination process starts to dominate. A possible explanation for the smaller value of τ_2 in the doped system can be related to a higher number of photo-generated electron-holes pairs, in agreement with the above described interpretation given by Rothenberger et al.[115] The presence of additional charges injected by V dopants can thus explain the faster decay for doped samples.

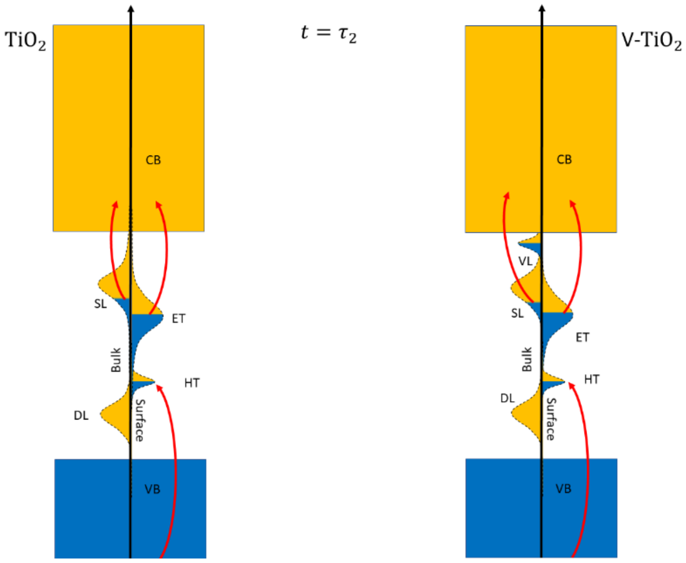

Figure 3.16: Electronic configuration at τ_2. Red arrows indicate the allowed transition giving rise to the differential spectrum.

For time delays greater than τ_2, the recombination between photo-generated charges is still the dominant process. This is confirmed by the slow decay of the trapped holes peak. However, after 500 ps the trapped holes signal is still present, while the broad signal related to the photo-generated electrons is almost absent. A possible explanation of this asymmetry, as mentioned above was given by Tamaki et al.[122] Trapped holes can remain on the NPs surface for a very long time because some of the electrons remain trapped inside the deep levels of the bulk characterized by a very low mobility. Electrons trapped in the deep levels, located well below the surface trap levels in the energy scale do not show any absorption in the range around 730 nm explaining the disappearing of the electron feature. With some photo-generated electrons trapped inside the bulk, according to their estimation a fraction of the photo-generated holes on the surface can remain trapped also for a few ms without recombining. In detail, the mechanism they proposed is based on the possibility to transfer a few electrons from the surface trap levels to the shallow levels of the bulk. This, as mentioned above, is possible because the two bands partially overlap in the energy range. They estimated that that once in the shallow levels, a few electrons can decay into the deep levels in around 500 ps explaining, together with the e-h recombination process why the electrons feature is almost absent after this amount of time. In Figure 3.17 and Figure 3.18, cartoon pictures of these processes are shown.

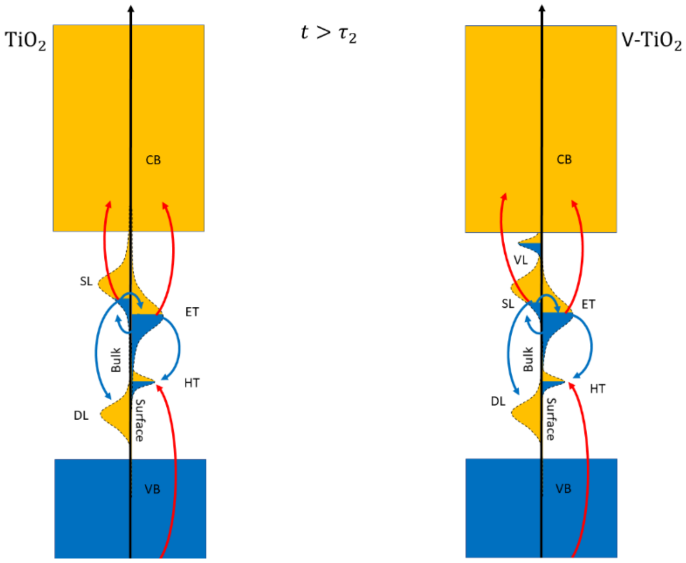

Figure 3.17: Electronic configuration for t > τ_2. Blue arrows indicate electron transitions. Red arrows indicate the allowed transition giving rise to the differential spectrum.

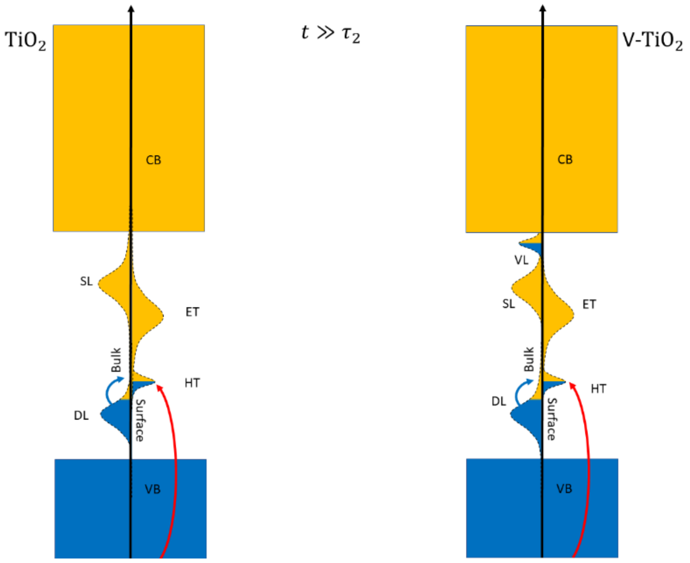

Figure 3.18: Electronic configuration for $t \gg \tau_2$. Blue arrows indicate electron transitions. Red arrows indicate the allowed transition giving rise to the differential spectrum.

In Table 3.2, the interpretation of the observed dynamic is schematically resumed.

Table 3.2: Schematic summary of the time behavior of photo-generated electrons and holes

Time	**Behavior of the Electron Feature (730 nm)**	**Behavior of the Trapped Holes Feature (400 nm)**	**Interpretation**
$\boldsymbol{t = 0}$	Instantaneous rise	Absent	Laser excitation generates valence to conduction band transitions. This, together with electrons filling the shallow levels of the bulk, gives rise to the feature centered at 730 nm
$\boldsymbol{0 < t < \tau_1}$	Fast decay	Fast rise	Photo-generated charges propagate from the bulk to the surface where trapping takes place. With the appearance of trapped holes on the surface the associated feature at 400 nm shows a fast rise. The feature at 730 nm decreases because of the e-h recombination, involving free holes in the VB.
$\boldsymbol{\tau_1 < t < \tau_2}$	Decay	Slow rise	The population of trapped holes on the NPs' surface grows because of the free ones propagating from the bulk. At the same time, the growth is limited by the decay of electrons from the conduction band. At $t = \tau_2$ the recombination between electrons in

			the CB and holes in the VB is almost complete and without free holes the population of trapped holes on the surface starts to decay.
$\boldsymbol{t > \tau_2}$	Decay	Slow decay	Some of the electrons from the surface traps decay to the deep levels of the bulk in a two-step process involving shallow bulk levels. This process, with a lifetime of around 500 ps, separates a small portion of electrons from the surface trapped holes, greatly increasing the electron hole recombination time, up to the ms timescale.

Before concluding this section regarding the studies performed with an exciting pulse of 330 nm it is useful to describe a fluence dependence study to observe the effects of the pump intensity on the differential signal. The expected result according to the previously cited paper of Rothenberger et al.[115] is a speed up of the decay signal when the fluence of the excitation pulse increases exciting an higher number of electron-hole pairs.

Because of its better signal to noise ratio the fluence dependence study was performed sampling the decay of the electrons feature at 730 nm. The measurements were performed on the V-TiO2 sample using pump beams with different fluences. In Figure 3.19 it is shown how higher fluences can speed up the electron dynamics. Fitting the signals with the function described in equation 3.4 it is evident that for higher fluences (5 μJ/pulse) the faster dynamics is due to a shortening of all the decay lifetimes. The long living dynamics is also speeded up, in fact, the slope $\frac{1}{\tau_4}$ for 5 μJ becomes clearly higher than 0. Thus, our measurements confirm the literature results and provide further evidence that the model proposed by Rotherberger et al. is correct.

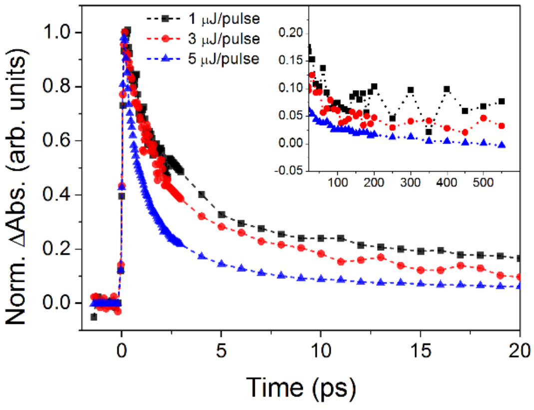

0

Figure 3.19: Fluence dependence study on V-TiO2. The time traces are collected at 730 nm

Table 3.3: Parameters list for different fluences

Parameter	1 μJ/pulse	3 μJ/pulse	5 μJ/pulse
A_∞	0.6 (0.1)	0.6 (0.5)	1.8 (0.1)
C_1	2.6 (0.5)	7 (1)	19 (1)
C_2	3.8 (0.4)	6.3 (0.9)	24.6 (0.9)
C_3	1.3 (0.4)	1.5 (0.5)	5.3 (0.7)
τ_1	0.6 (0.1)	1.0 (0.2)	0.35 (0.02)
τ_2	4 (1)	5 (1)	1.7 (0.1)
τ_3	30 (20)	60 (50)	15 (3)
$1/\tau_4$	0.0000 (0.0001)	0.000 (0.001)	0.0037 (0.0005)

3.2.3.2 EXCITING AT LOWER ENERGIES

As mentioned above, V doping increases the absorption spectrum of TiO_2 in the region between 350 and 550 nm. Which optical transitions are triggered by these excitation wavelengths? To answer this question two pump and probe experiments were performed using lower energy pump pulses. A first set of measurements was performed exciting with a 400 nm pump pulse, in the spectral region where the difference between the static absorption spectra of doped and undoped TiO_2 is maximized. At this wavelength it is still possible to excite some transitions between the tails of the VB and CB in undoped TiO_2. To probe only doping-related effects exclusively, measurements were also performed with excitation pulses of 530 nm, at which wavelength undoped TiO_2, does not absorb light.

The transient signals obtained exciting with 5 μJ pulses of 400 nm wavelength are comparable with to those described in the previous section and obtained with 330 nm excitation. 2D maps of the transient signal are shown in Figure 3.20, while the spectral traces for several time delays are shown in Figure 3.21. The features observed around 400 nm and related to the absorption spectrum of trapped holes on the nanoparticle surface, cannot be monitored in this experiment because of the large amount of pump scattered radiation that saturates the detector at 400 nm.

The feature related to the photo-generated free and trapped electrons is still visible and centered around 730 nm. The main difference between doped and undoped samples is clearly the intensity of the measured differential signal, that for the doped sample at 730 nm is almost an order of magnitude higher than that generated by the undoped sample. This means that exciting V-TiO_2 with sub-bandgap radiation it is still possible to photo-generates a lot of free and trapped electrons. The time trace sampled at 730 nm can be well fitted with the function described in equation 3.4 as shown in Figure 3.22 where a direct comparison of the normalized decay signals for the doped and undoped TiO_2 samples is also shown. The interpretation of the decay phenomena given for the previous experiment with a 330 nm wavelength excitation is still valid. The main difference is that for undoped TiO_2 the number of photo-generated charges is very small. Also in this case the recombination dynamics is faster for the doped sample. This can be related also in this case to the relation between the decay lifetime and the number of photo-generated trapped charges at time zero. This number is clearly higher for the doped sample and consequently a faster decay is expected. A further proof of the higher number of trapped electrons generated in the doped sample is the amplitude of the C_n coefficients refined with the fitting procedure and listed in Table 3.4. The values of these coefficient are almost an order of magnitude higher for the doped sample.

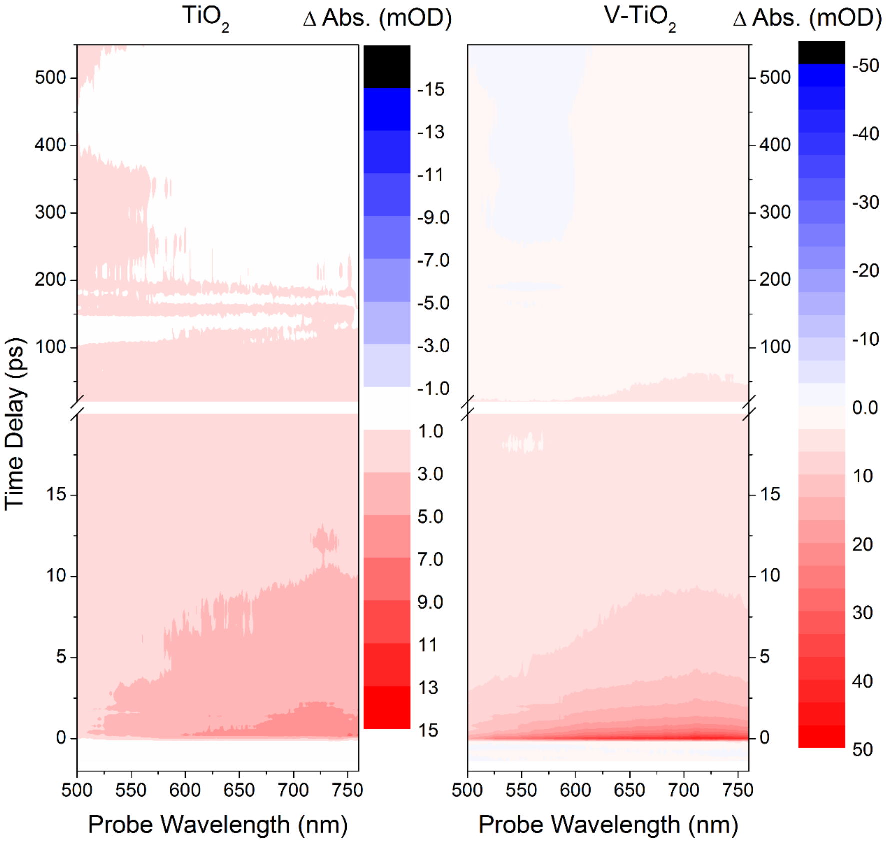

Figure 3.20: 2D maps of the transient signal generated by undoped TiO$_2$ (left) and V-doped (right) NPs with 400 nm pump pulse.

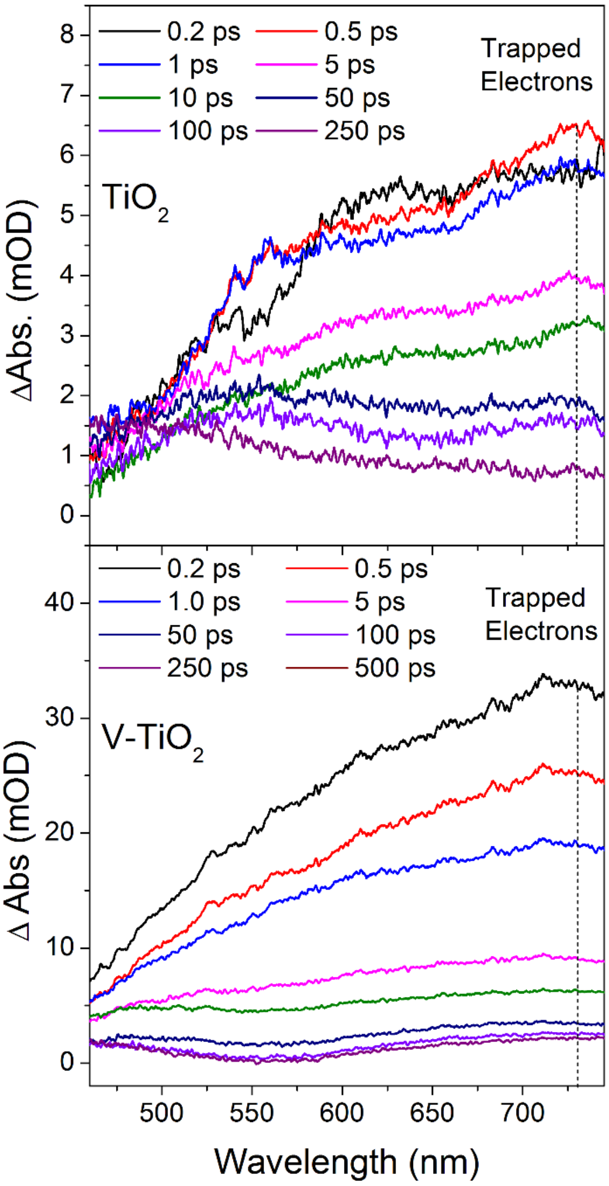

Figure 3.21: Transient signals generated by undoped (top) and doped (bottom) TiO_2 with 400 nm pump with a 5μJ/pulse fluence

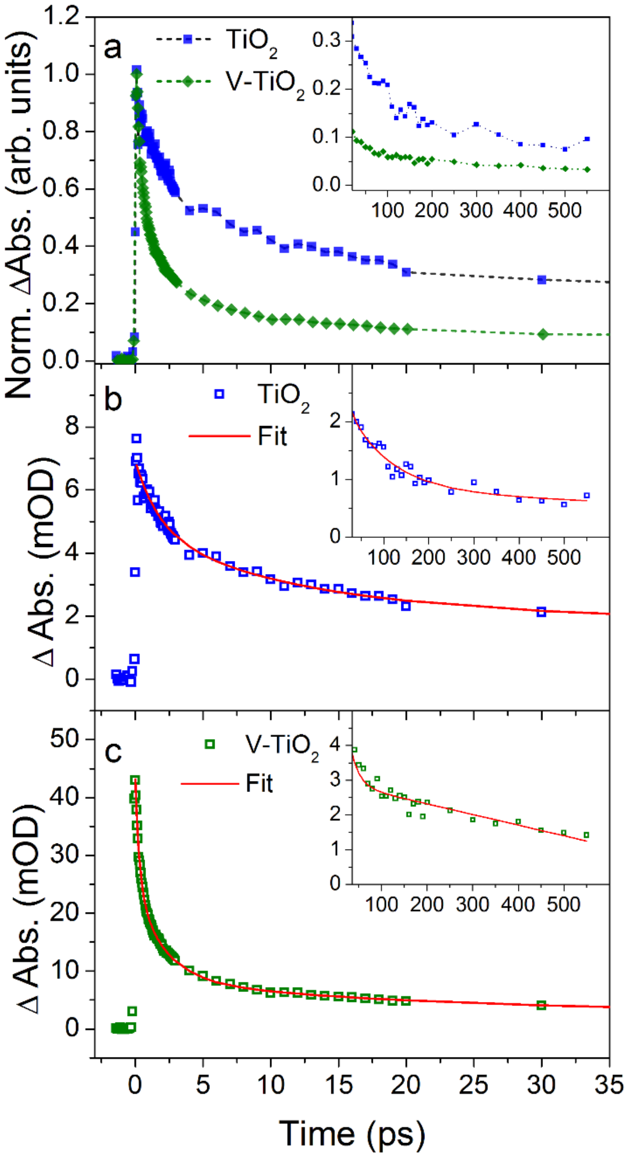

Figure 3.22: Time traces with 400 nm excitation.

Table 3.4: Fit parameters of the transient signal at 730 nm for undoped and doped TiO2

Parameter	**TiO_2**	**V-TiO_2**
A_∞ (mOD)	0.8 (0.7)	2.9 (0.1)
C_1 (mOD)	1.9 (0.6)	18.3 (0.5)
C_2(mOD)	2.3 (0.5)	16.0 (0.5)
C_3 (mOD)	1.7 (0.4)	5.3 (0.7)
τ_1 (ps)	1.7 (0.5)	0.31 (0.01)
τ_2 (ps)	9 (4)	2.0 (0.1)
τ_3 (ps)	100 (70)	19 (2)

k (1/ps)	0.000 (0.001)	0.0030 (0.0004)

Also in this case a fluence dependence study was performed on the doped system. The sample was excited with 400 nm pulses with 2 μJ, 5μJ and 10 μJ. In this case, as shown in Figure 3.23, differences between low and high fluence spectra are almost negligible. This can be related to the limited number of electrons that can be excited with 400 nm radiation. In particular, there is no difference between the 10 μJ and 5 μJ spectra while the one measured exciting with 2μJ pulses is too noisy to clearly spot a slower decay.

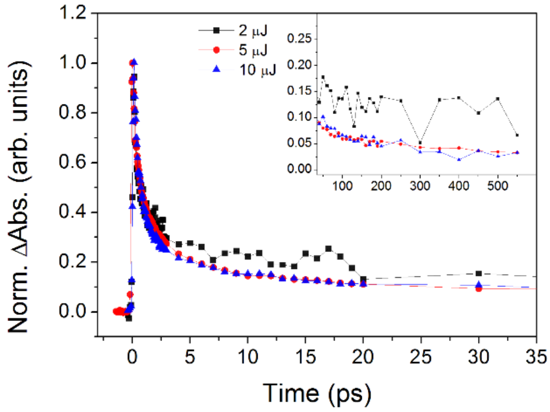

Figure 3.23: Fluence dependence studies at 730 nm with a 400nm pulse.

Performing the same experiment with a 530 nm excitation, it was impossible to measure any signal on the undoped TiO_2, sample; however as shown in Figure 3.24, using 20 μJ pulses, it was possible to observe a weak transient signal in the region around 730 nm for the doped sample, which exhibits a very slow decay. Using the same arguments used above it is possible to explain the long lifetime as a consequence of the presence of a very small number of photo-generated electrons, coupled with the absence of free holes in the valence band. Despite the low intensity these results are a clear proof that V incorporation makes possible the photo-generation and the surface trapping of electrons also exciting with green light.

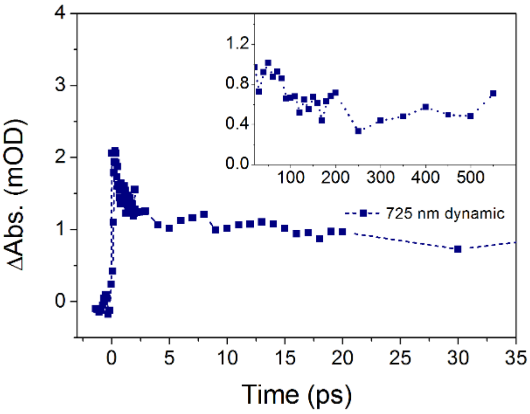

Figure 3.24: Transient signal at 730 nm for doped TiO_2 obtained with a 20μJ, 530 nm pump pulse

4 ELEMENT – SPECIFIC CHARGE TRANSFER VIA HIGH RESOLUTION X-RAY SPECTROSCOPY

What happens from an atomistic point of view when V-TiO_2 is excited in the visible range? How do the dopant atoms behave? Which are the atomic species exchanging charge carriers? In the previous section the time evolution of trapped electrons and holes on the nanoparticle surface was investigated using optical ultrafast transient absorption spectroscopy. However, this technique cannot directly answer the previous questions because of the lack of element selectivity. For this reason, a differential illumination high resolution XAFS experiment was designed, to specifically probe the role of V when the sample is exposed to visible radiation.

4.1 SAMPLES

The samples chosen for this kind of analysis were V-TiO_2 nanoparticles assembled films, deposited with the same method described in section 2.1. The two samples are labeled with letters A and B. Sample A, is the same used for the ultrafast transient absorption spectroscopy studies described in section 3. The XRD patterns reported in Figure 4.1 indicate that A and B have different crystal structures. Patterns were recorded with a Panalytical X'Celerator powder diffractometer using Cu K_α radiation. Both structures are a superposition of rutile and anatase phases. Tab. 1 lists the relative phase abundances determined by Rietveld refinement of XRD patterns using the program MAUD.[123] As mentioned above in section 3 sample A is mainly composed by rutile (≈ 80%), while in sample B the two phases (anatase and rutile) exhibit similar weight fractions. The weak and broad reflection around 31° indicates that both samples contain a small amount of brookite. Like in section 2.1, no Bragg reflections attributable to vanadium oxides were detected. Analysis of the peak broadening yields a crystallite size of about 15 nm.

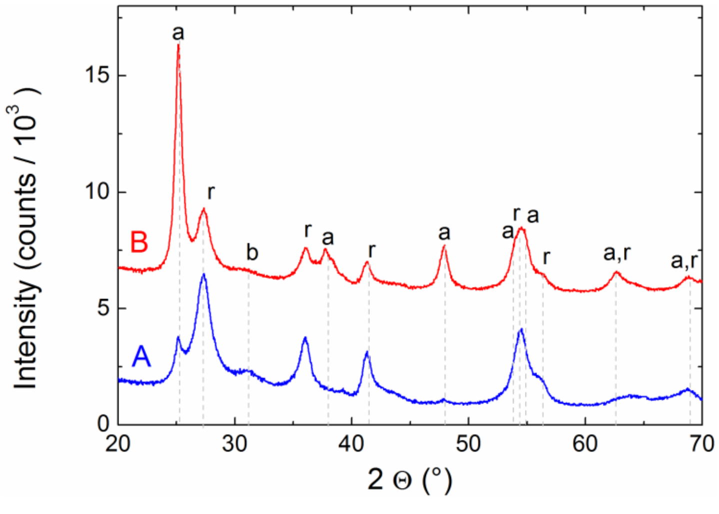

Figure 4.1: XRD patterns of samples A and B, vertically shifted for the sake of clarity. The Bragg reflections of rutile (r), anatase (a), and brookite (b) are indicated.

Table 4.1: Phase composition (a=anatase, b=brookite, r=rutile), determined by XRD analysis and V content measured by EDS for the two V-TiO_2 NPs samples. Uncertainties expressed as one standard deviation on the least significant digit are given in brackets.

Sample	**Composition (wt %)**			**V/(Ti+V) (at.%)**
	a	b	r	
A	10 (2)	10 (2)	80 (4)	3.0 (5)
B	43 (3)	10 (2)	47 (3)	3.5 (5)

4.2 EXPERIMENTAL SETUP

The experimental setup used for the differential illumination experiments was assembled at the ID26 beamline[67] of the ESRF in Grenoble, France. This beamline, designed for RIXS and HERFD XAS measurements uses a set of analyzing crystals to monochromatize the scattered radiation coming from the exposed sample. The choice of a RIXS beamline was suggested by the partial overlapping of Ti K_β and V K_α emission lines. The background generated by Ti cations must be filtered out to avoid the generation of completely misleading distortions in the absorption spectra at V K edge.

The beamline was equipped with a Si(311) double crystal monochromator. Higher harmonics were rejected by three Si mirrors in total external reflection at 2.5 mrad. The Johann emission spectrometer showed in Figure 4.2, based on Bragg optics arranged in Rowland geometry, was equipped with five Ge(331) bent (R = 1 m) crystal analysers and tuned between 75.58° and 74.70° to analyse alternatively Ti K_β and V K_α emission lines. The combined resolution of monochromator and spectrometer was 0.7 eV. All measurements were performed at room temperature and in air so no cryostat or vacuum chamber were used.

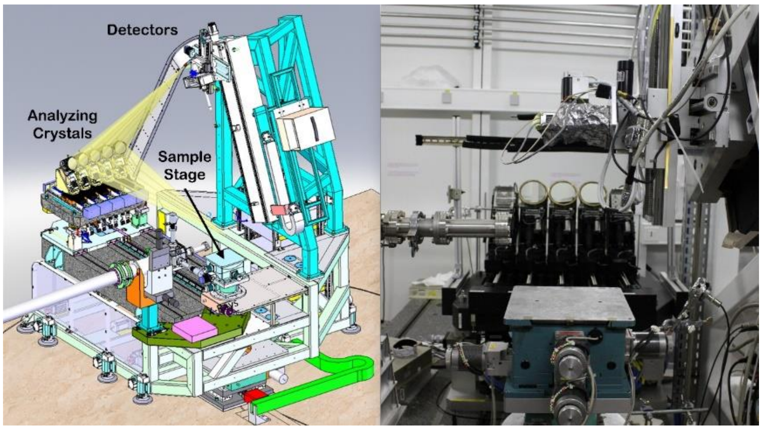

Figure 4.2: Left Panel. Schematic description of ID26 experimental setup. Right Panel: Detail of the analyzing crystals.

The visible excitation was performed using a 532 nm, continuous wave, 200 mW laser diode, focused in a 1.2 mm^2 circular spot superposed to X-ray beam. Selected HERFD - XANES spectra at both V and Ti edges were recorded with and without illumination. In order to minimize contributions coming from the sample damaging, acquisitions were performed in cycles. In each cycle dark and illuminated spectra were collected for one minute each. This procedure avoid the sampling of any contribution due to eventual X-ray induced damaging of the sample. To have a significant signal to noise ratio on the differential spectrum, around 100 cycles were performed for each sample. To exclude changes in the XANES spectra due to laser heating, sample was monitored with an IR thermometer. After laser exposure, the sample temperature increased less than 3 °C.

Below it will be clear that charge transfer phenomena are strictly related to the energy position of absorption edges. For this reason, a check of the reproducibility of the energy axis was mandatory. This was done comparing the position of a clearly identifiable pre-edge feature over 100 spectra collected under the same illumination condition. The resulting standard deviation of the mean was less than 5 meV.

4.3 RESULTS AND DATA PROCESSING

In this paragraph the experimental results will be shown. First the results of RIXS investigations will be described. From the RIXS planes it is possible to highlight the most promising emission energies to be sampled in the HERFD XAS experiments. After, the results of the differential illumination experiment will be shown.

4.3.1 RIXS CHARACTERIZATION OF THE SAMPLES

RIXS, as shown in section 1.1.2, is a powerful technique combining X ray absorption and emission. A RIXS study in the pre-edge region gives a lot of information about the origin of the various features arising in this portion of the absorption spectrum. This technique is moreover particularly suited to spectra of transition metal oxides, which are characterized by several pre-edge features.[124]

As illustrated in section xxx, RIXS planes and HERFD XANES spectra are strictly related, in fact fixing an emission energy ω and variating the incoming photon energy (i.e. tracing a diagonal line in a RIXS plane) it is possible to select one of the possible HERFD XANES spectra. Performing RIXS investigation before HERFD XANES experiments can be very useful as shown in the paper by Amidani et al.[34] As shown in Figure 4.3, they highlighted that the RIXS plane for anatase nanoparticles around Ti K_β emission line is characterized by the presence four pre-edge features. Two of them labelled as A_3 and B lie on the same diagonal of the main edge, while the others (A_1 and A_2) appears for lower emission energies.

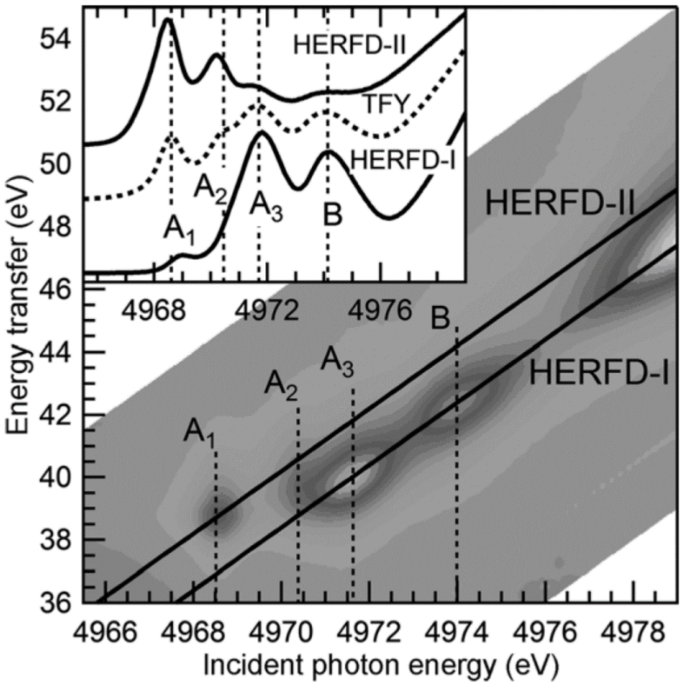

Figure 4.3: RIXS plane at Ti K_β emission line for anatase nanoparticles. Figure taken from reference 34.

According to Glatzel et al.[35] the distribution of the pre-edge peaks in different cuts of the RIXS plane is due to the different localization of the final states reached. Delocalized states (HERFD-I) are less affected by the core-hole potential and the associated features lie on the same diagonal of the main edge. The other peaks appearing at different emission energies (HERFD-II) are instead related to those final states localized near the absorber that are highly influenced by the presence of the core-hole excitation. For the current experiment on V-TiO_2 the only HERFD-XANES spectrum considered at Ti K-edge is that labeled as HERFD I in Figure 4.3. This diagonal line containing the main edge is obtained sampling only those photons emitted at the maximum of Ti K_β emission. Because of the different emission energies of localized final states, HERFD-XANES spectra for the two measured samples are quite different from total fluorescence ones as shown in Figure 4.4. Features A_1 and A_2 related to the transitions to localized final states appearing at lower emission energies are almost absent in HERFD-I spectra.

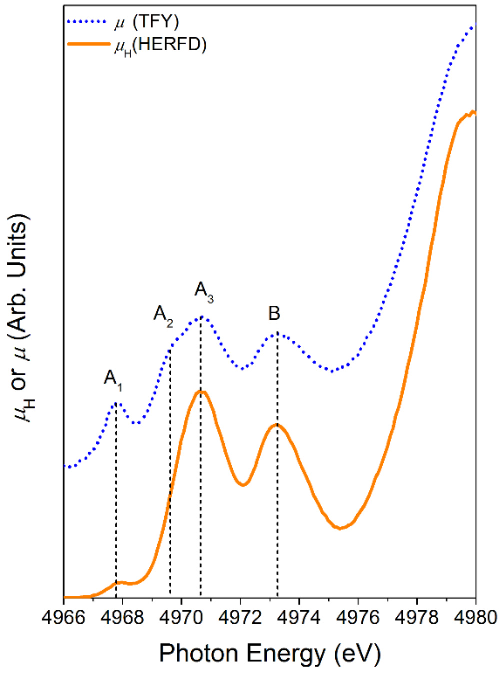

Figure 4.4:Comparison between HERFD XANES and TFY spectra of sample B. Features A1 and A2 are extremely lower in the HERFD spectrum, because of the difference in emission energy.

RIXS planes around V K$_\alpha$ emission line were collected for both A and B samples. As shown in Figure 4.5, from the RIXS plane it is not possible to spot the presence of features outside the diagonal line including the main edge. The choice of the selected emission energy for HERFD XANES spectrum is thus unique since no interesting feature lies out of the main edge diagonal. The chosen cut is shown in Figure 4.5 as a dashed red line.

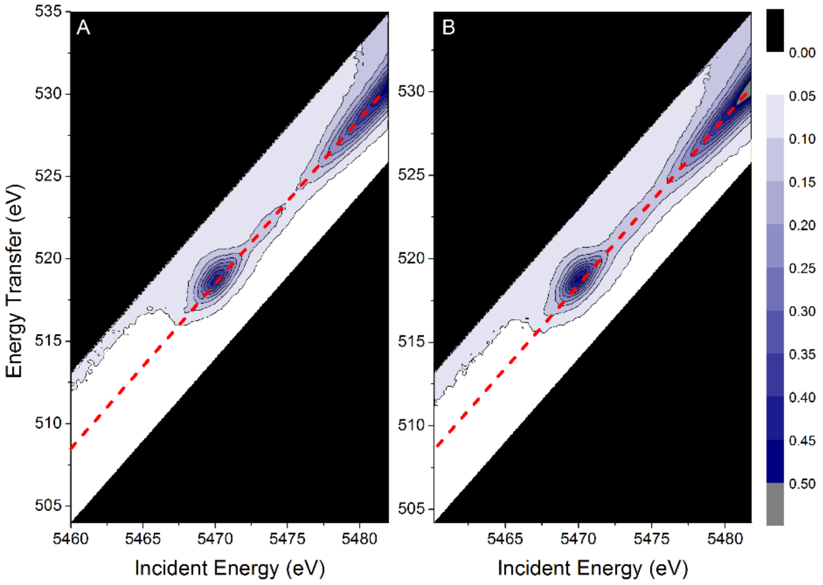

Figure 4.5: RIXS planes at V Kα emission lines for samples A (left) and B (right). The diagonal cut chosen to measure the HERFD XANES spectra in the differential illumination condition is shown as a red dashed line.

4.3.2 RESULTS OF THE DIFFERENTIAL ILLUMINATION HERFD XANES EXPERIMENT

4.3.2.1 EVALUATION OF THE DIFFERENTIAL SIGNAL

In this section, the data treatments used to refine the differential signal from the raw data-sets is carefully described. Differential spectra are defined in equation 4.1, where μ_E and μ_D indicate respectively the XANES spectra obtained with and without laser excitation.

$$\Delta\mu(\mathrm{E}) = \mu_E(E) - \mu_D(E) \tag{4.1}$$

μ_E and μ_D are obtained performing the following processing steps: normalization to the intensity of the incoming beam, averaging of the scans to increase the signal to noise ratio, subtraction of the pre – edge region (estimated with a linear fit in the regions 5450-5460 eV for V and 4950-4960 eV for Ti spectra) and normalization to the average value in the post – edge region (between 5015 and 5035 eV for Ti spectra and between 5520 and 5550 eV for V spectra). The whole procedure was performed using PyMCA.[125]

4.3.2.2 EXPERIMENTAL EVIDENCES

In Figure 4.6, the measured differential signals for both samples are shown. It is immediate to notice that although the different crystal structure between A and B the differential signal look very similar. Focusing on the main edge region of the absorption spectra as shown in Figure 4.7 it is possible to see rigid shifts at both Ti and V K edges. In particular, the shifts for the two edges are in opposite directions. This correlation between Ti and V was the starting point of the data analysis described below.

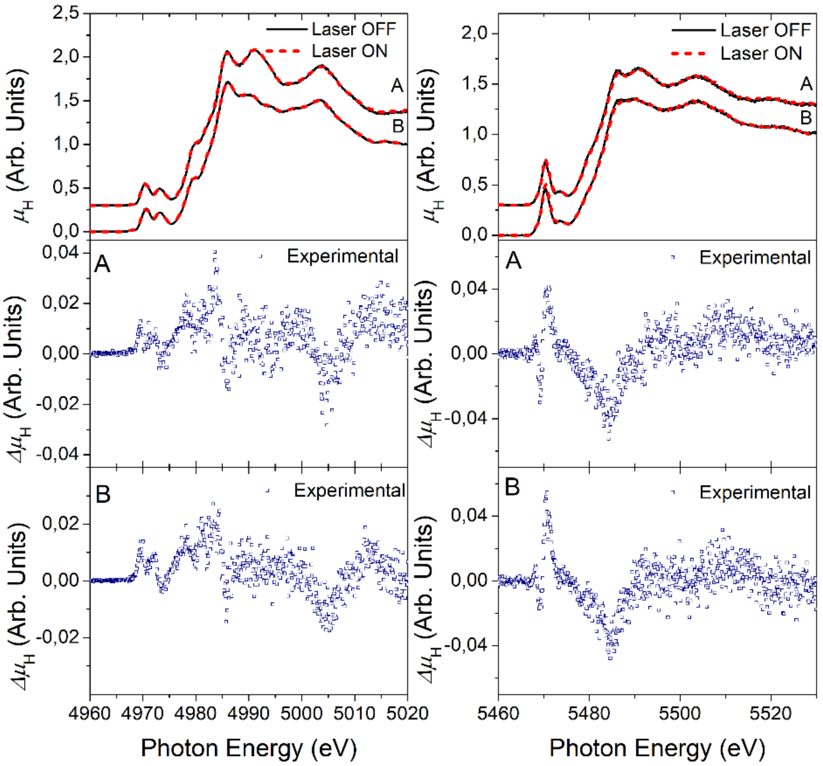

Figure 4.6: Differential HERFD-XANES signals for samples A and B.

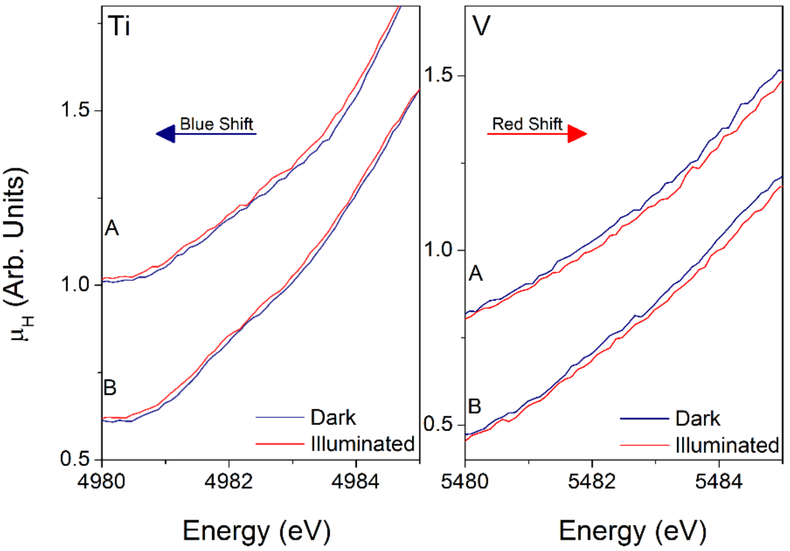

Figure 4.7: Zoom of the edge region of dark and illuminated HERFD spectra. At Ti K edge a blue-shift due to the laser excitation is apparent. At V K-edge, the shift is in the opposite direction

4.3.3 DATA INTERPRETATION

The small but visible shifts, shown above, suggested a possible interpretation of the experimental data. As shown below, rigid shifts of the main edge can be related to charge transfer phenomena involving the absorbing species. In this paragraph a function to fit the differential signal is also derived.

4.3.3.1 THE RIGID SHIFT ANALYSIS

Some photo-excitation phenomena, characterized by a charge transfer involving different atomic species, can be described as shown in Figure 4.8 where the model sample is composed by two atomic species (Z and Z_2). The laser excitation generates the migration of electrons coming from the Z atoms that can recombine with the photo-generated holes or get captured in localized orbitals leaving the system in a metastable state. In the particular case shown in Figure 4.8, electrons remain trapped in molecular orbitals localized around Z_2 atoms.

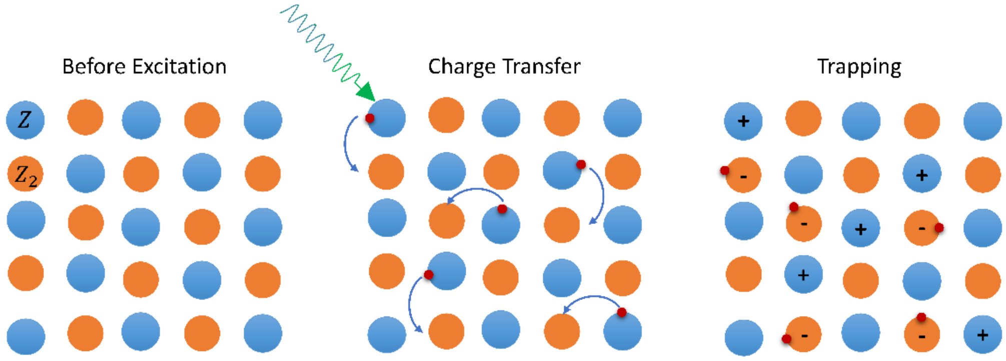

Figure 4.8: Atomistic description of a photo-induced charge exchange phenomenon. The green radiation, generates the migration of electrons (red circles) from one element to the other.

The charge transfer phenomenon generates changes in the electronic configuration of the involved atoms. In particular, the variation of the screening potential induces changes of the binding energy of core electrons for both injecting and trapping species. In this particular situation, the expected effects are shown in Figure 4.9. The screening potential contribution decreases for Z atoms injecting their electrons and increases for the trapping atoms Z_2. If the charge rearrangements are not associated to significant structural distortions the excited state spectra for the involved atoms will be just shifted copies of the unexcited ones. The shifts will be to higher energies for the spectra related to those species injecting charge carriers and to lower ones for the trapping ones.

For both injecting and acceptor species, only on a certain fraction α of atoms is influenced by the charge transfer. For this reason, the illuminated absorption spectrum μ_i can be written as the superposition of an excited component (identical to the dark spectrum μ_d but shifted by an energy ΔE) and the dark spectrum generated by the portion of unexcited atoms. In formulas, it can be written as shown below

$$\mu_i(E) = \alpha\, \mu_d(E - \Delta E) + (1 - \alpha)\mu_d(E) \qquad 4.2$$

The direct consequence of equation 4.2 is a simple expression for the differential signal $\Delta\mu$ (equation 4.3) depending only by the two parameters ΔE and α.

$$\Delta\mu(E) = \mu_i(E) - \mu_d(E) = \alpha\,(\mu_d(E-\Delta E) - \mu_d(E)) \tag{4.3}$$

Equation 4.3 can be used to calculate hypothetical signals to be compared with the measured differential spectra. It is also important to remember that the α parameter can be different for the different atomic species.

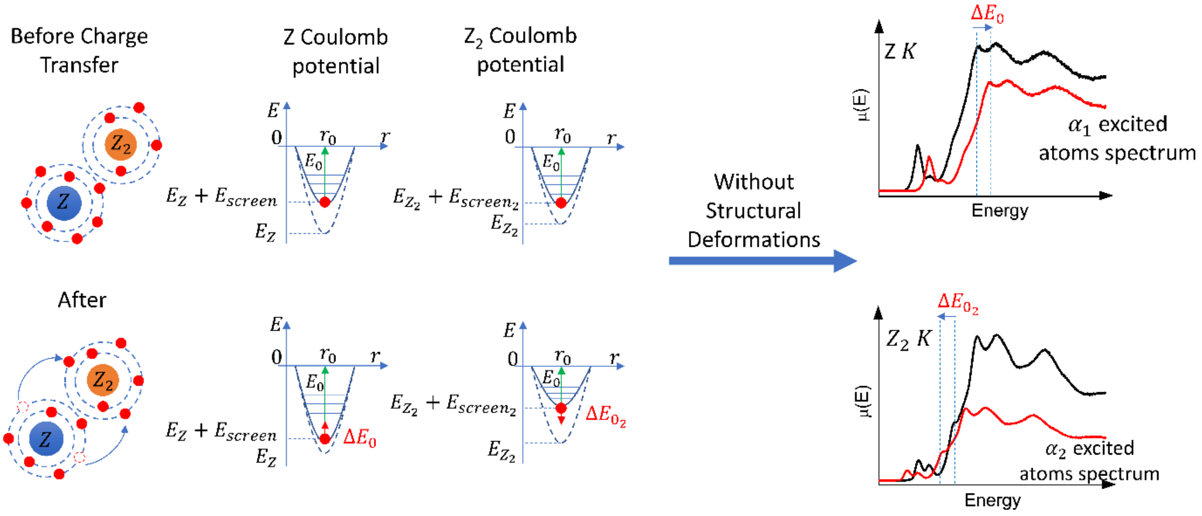

Figure 4.9: Effects on the main edge position of Z and Z2 absorption spectra after charge transfer

4.3.3.2 Fit of the Differential Spectra

To find the best values for the α and ΔE parameters of equation 4.3 a Python routine was implemented. The code generates a dense grid of $(\Delta E, \alpha)$ combinations. The range of possible ΔE values was set from -5 eV to 5 eV, while α can vary from 0 to 1. For each combination, a calculated spectrum is evaluated using equation 4.3. The best fit spectra were chosen minimizing the χ^2 merit function. The goodness of the fits was estimated using the incomplete gamma function $Q\left(\frac{N-M}{2}, \frac{\chi^2}{2}\right)$ depending on the values of the χ^2 function and the number of independent points $(N-M)$. According to the literature[126] a fit can be considered acceptable if the value of the this merit function becomes higher than 0.1. Plotting the values obtained for the Q function in a ΔE vs α plane it is possible to observe which are the combinations giving the most reliable fits. As shown in Figure 4.10 ΔE and α show a nonlinear correlation. For this reason, the best fit combination is not unique. However, it is clear that ΔE must be positive for V spectra and negative for Ti ones. A way to overcome the best fit degeneracy problem is to fix the value of one of the parameters and to refine the other.

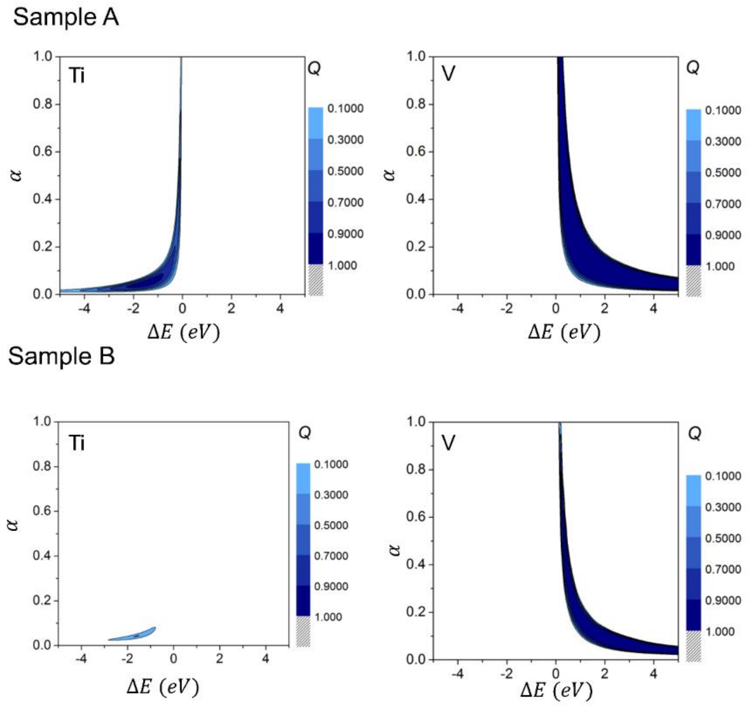

Figure 4.10: Q function values for all the considered combinations $(\Delta E, \alpha)$. For both samples, the best fit is not unique.

Reasonable values for ΔE can be obtained exploiting the differences in the main edge position of Ti and V oxides with different oxidation states of the cations. Charge transfer effects, described above are very similar to those generated by changes in the oxidation state described in section 1.1.1.2. For this reason, since V donates one of its electrons, this can be interpreted like an oxidation process. In bulk doped structures, the oxidation state of V cations according to FDMNES calculation is mainly 4+ but after the excitation the population of V^{5+} cations increases because of the charge exchange between V and Ti cations. For this reason, the ΔE_V parameter was set to the value defined in equation 4.4 where $\mathrm{E_0(V_2O_5)}$ and $\mathrm{E_0(V_2O_4)}$ are respectively the main edge positions in the V^{5+} and V^{4+} reference oxides spectra.

$$\mathrm{\Delta E_V = E_0(V_2O_5) - E_0(V_2O_4) = 1.0\ eV} \qquad 4.4$$

For Ti, the charge transfer can be described like an oxidation state transition from 4+ to 3+. The $\mathrm{\Delta E_{Ti}}$ can be thus evaluated using equation 4.5 where the main edge positions used where those of TiO_2 and Ti_2O_3.

$$\Delta E_{Ti} = E_0(Ti_2O_3) - E_0(TiO_2) = -2.0\ eV \qquad 4.5$$

With these settings for the ΔE parameters, it is possible to refine the fractions of excited atoms fitting the differential signals. Fit results are shown in Figure 4.11. All the differential signals can be well reproduced using fit signals generated using the rigid shift analysis. The refined values for the α parameters are in the same ranges for both samples. In particular the fraction of excited Ti atoms is 0.035 ± 0.015, while for V α is 0.2 ± 0.1. The ratio of these two values is very similar to that between the number of V and Ti atoms. For this reason, it is possible to conclude that charge injected from V dopants are trapped in localized defects near Ti cations.

Although the rigid shift gave an optimal description of the differential signals especially in the post-edge region, some small discrepancies can be observed in the pre-edge regions. This is not surprising since as discussed several times above, all the features appearing in this spectral range are related to transitions to empty bound levels. These last are usually molecular orbitals that can be dramatically modified by a change in the screening potential of the absorber. For this reason, the rigid shift can be only one of the possible changes induced by the laser excitation. In Figure 4.12 the pre-edge features at Ti and V K edge for sample B are shown. Focusing on the differential signal at V K edge it is possible to see a peak-derivative shape. This is clearly due to the rigid shift generated by the change in the screening potential. However, looking at the highest pre-edge peak, it is possible to see that its amplitude is clearly higher when the sample is excited. This can be originated by the combination of two effects. When one of the V electrons is removed the density of empty bound states must increase, generating a higher pre-edge feature. On the other hand, if the local distorted-octahedron symmetry is significantly changed after the charge transfer this amplitude enhancement can be also related to a less centro-symmetric structure surrounding the absorber as described in section 1.1.1.2. Looking at the Ti K edge spectrum, it is possible to see three peak-derivative features related to the rigid shift contribution. However, the presence of a positive maximum of the differential spectrum at the A_2 peak position suggest the photo generation of additional Ti^{3+} defective sites on the nanoparticle surface. This because in the literature this feature has been several times related with this kind of defects.[34,71]

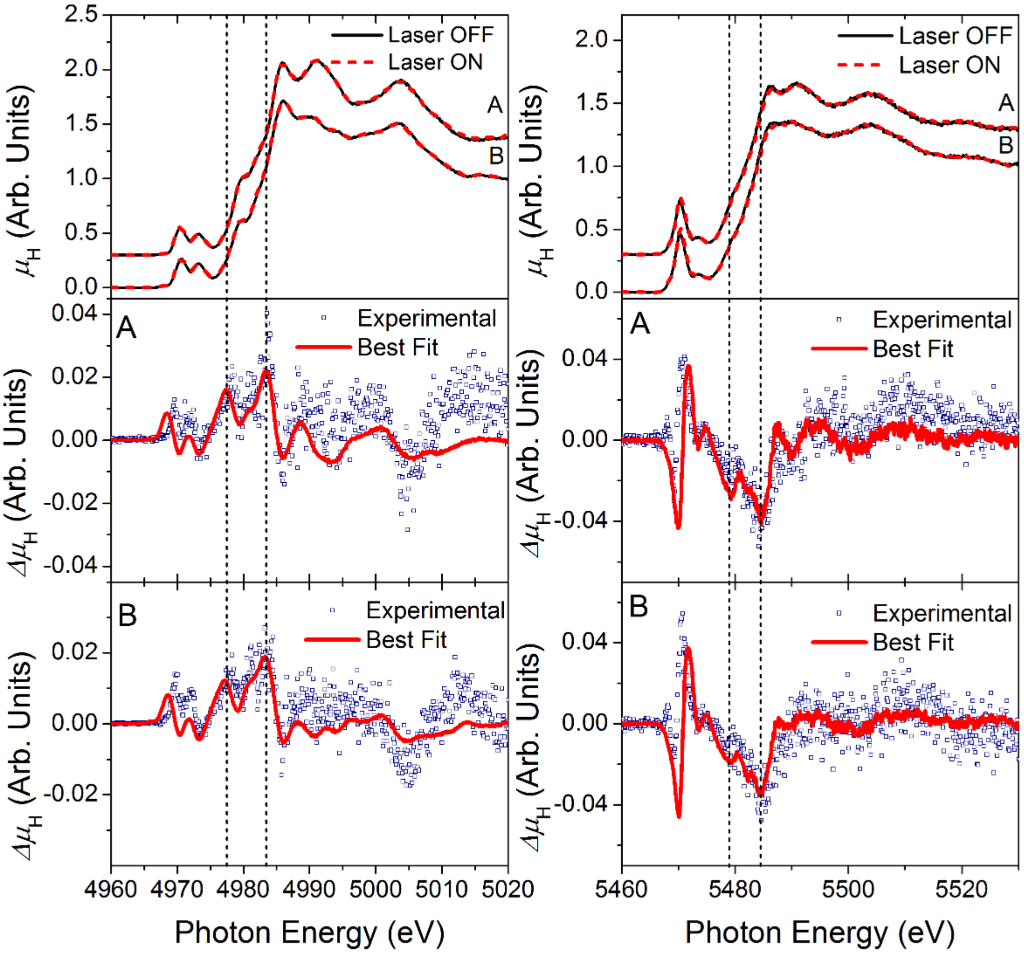

Figure 4.11: Fit of the differential signals with fixed values of ΔE

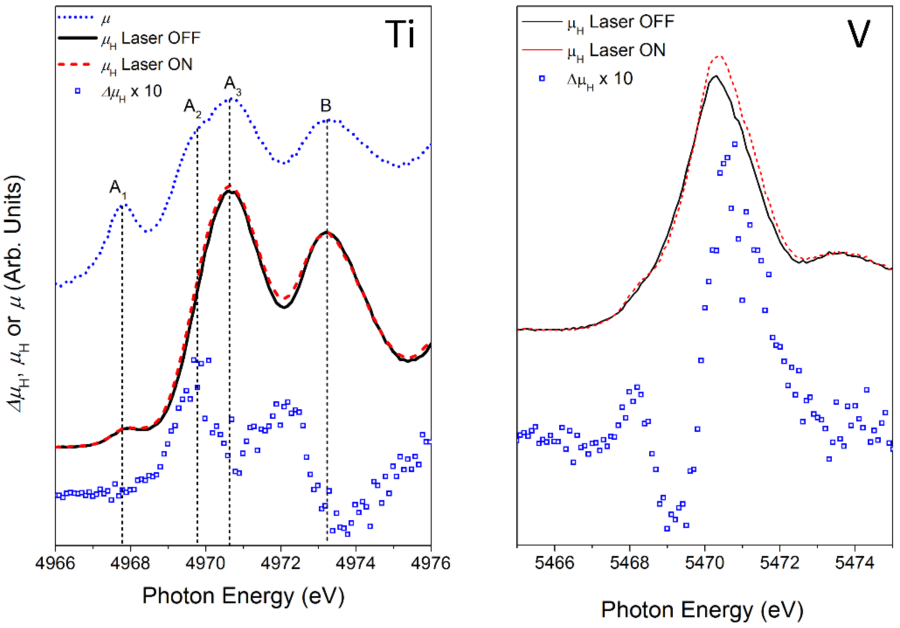

Figure 4.12: Zoom on the pre-edge differential signals

4.4 EXCITATION LIFETIME

An estimation of the excitation lifetime can be obtained using a simple two-level model in which V atoms can be found only in two states: the ground state (before charge transfer) and an excited one (after charge transfer). Assuming trapping to be a long living process it is possible to suppose that in case of continuous excitation the system will be in a steady state. In principle, the population of excited and non-excited atoms in these conditions will be a constant. Defining n_g and n_e respectively the ratio of V atoms in the ground and excited state it is possible to write the following set of equations:

$$\begin{cases} n_e + n_g = 1 \\ \dfrac{dn_e}{dt} = p_{ge}n_g - p_{eg}n_e = 0 \\ \dfrac{dn_g}{dt} = p_{eg}n_e - p_{ge}n_g = 0 \end{cases} \qquad 4.6$$

The quantities p_{eg} and p_{ge} are respectively the transition rates from the excited state to the ground and vice versa. The determination of the first of those probabilities is fundamental, because it is easy to understand that the lifetime τ_{eg} is equal to $1/p_{eg}$. The excitation rate p_{ge}, will be directly proportional to the incoming laser flux Φ multiplied times the absorption coefficient of V-doped compounds at 532 nm. The number of ground to excited transitions per V atom per unit times can thus be obtained using equation 4.7.

$$p_{ge} = \frac{\Phi\mu(532)}{\rho_V} \qquad 4.7$$

The values used for the parameters in the equation above are $4 \cdot 10^{19} \frac{ph}{s \cdot cm^2}$ for Φ, $9.6 \cdot 10^{20}\ cm^{-3}$ for ρ_V and $7.7 \cdot 10^{-3}\ cm^{-1}$ for $\mu(532)$. The last value was obtained from the diffuse reflectance spectra obtained from the measurements shown in section 3. The ratio of atoms in the ground state can be well approximated using the α_V parameter obtained from the fits described in the previous section. Solving the system with these parameters it is possible to find a value for the trapping lifetime τ_{eg} of around 0.8 ms, comparable with the lifetime of trapped charges in TiO_2 indicated by Tamaki et al.[113] This result indicates that V doping induces the activation under visible radiation of the same charge transfer processes activated in TiO_2 nanoparticles exposed to UV radiation. This could be a first indication that V doping can lead to an efficiency enhancement of the photo-catalytic properties of TiO_2 in the visible range.

CONCLUSIONS

In this thesis, a series of advanced methods were employed to study the local structure and physical phenomena underlying visible light absorption in promising photo-catalytic systems for energy and environmental applications.

Using the unique characteristics of XAFS it was possible to investigate in detail the local environment of low concentrated V and N dopants in TiO_2 nanoparicles and thin films. State of the art *ab initio* codes were used to simulate the local atomic structure of the dopants and the related XANES spectra. The substitutional behavior of V cations in V_{Ti} sites was identified in both nanoparticles and thin films, while N was found both in substitutional N_O sites and in interstitial dimer configurations.

As shown in section 3, V doping increases the optical absorption coefficient of TiO_2 in the visible range. The physical mechanism behind this enhancement was investigated using ultrafast optical transient absorption spectroscopy. Analyzing the transient signals measured exciting doped and undoped samples with visible and UV radiation it was possible to follow in real time those electron transitions triggered in the optical regime. In particular, it was possible to follow the time evolution of those photo-generated charges trapped in intra-gap levels localized in defective sites on the nanoparticle surface. The most interesting result of this study was that exciting in the visible range (530 nm), it is still possible to observe trapping of photo-generated electrons in V-doped samples, while undoped ones do not respond in that region. This experiment proves that V-doping is a valuable method to generate partially filled levels in the TiO_2 bandgap. These electrons injected by V cations can be easily promoted to the conduction band and trapped on the nanoparticle surface where the photo-catalytic reactions take place.

With a differential illumination HERFD XANES experiment the processes accompanying optical excitation of V-doped TiO2 samples were studied. Despite the lack of time resolution, this experiment exploits the element selectivity of XANES to follow those changes appearing in the local environment surrounding selected atomic species. In particular, it was possible to clearly identify a charge transfer phenomenon between V dopants and Ti cations. Under visible irradiation one of the V electrons is transferred to a Ti cation and remains trapped. The lifetime of this phenomenon is very long (around 0.8 ms), in full agreement with the observation made by Tamaki et al.[122] using other experimental techniques. This result, coupled with that of the ultrafast transient absorption spectroscopy experiment clearly identifiesthe role of V as electron injector, providing a physical understanding on the origin of the increased the photo-catalytic efficiency of TiO_2 in the visible range.

The results summarized above are significant steps forward for the identification of those physical mechanisms characterizing an efficient photo-catalyst

REFERENCES

1. Rossi, G., d'Acapito, F., Amidani, L., Boscherini, F. & Pedio, M. Local environment of metal ions in phthalocyanines: K-edge X-ray absorption spectra. *Phys. Chem. Chem. Phys.* (2016). doi:10.1039/C6CP04022E
2. Rossi, G. *et al.* Local Structure of V Dopants in TiO2 Nanoparticles: X-ray Absorption Spectroscopy, Including Ab-Initio and Full Potential Simulations. *J. Phys. Chem. C* **120,** 7457–7466 (2016).
3. Koura, Z. E. *et al.* XANES study of Vanadium and Nitrogen dopants in photocatalytic TiO 2 thin films. *Phys. Chem. Chem. Phys.* (2017). doi:10.1039/C7CP06742A
4. Rossi, G. *et al.* Element-specific channels for the photoexcitation of V-doped TiO_2 nanoparticles. *Phys. Rev. B* **96,** 045303 (2017).
5. Santomauro, F. G. *et al.* Localized holes and delocalized electrons in photoexcited inorganic perovskites: Watching each atomic actor by picosecond X-ray absorption spectroscopy. *Struct. Dyn.* **4,** 044002 (2016).
6. Sayers, D. E., Stern, E. A. & Lytle, F. W. New Technique for Investigating Noncrystalline Structures: Fourier Analysis of the Extended X-Ray—Absorption Fine Structure. *Phys. Rev. Lett.* **27,** 1204 (1971).
7. Glatzel, P. & Bergmann, U. High resolution 1s core hole X-ray spectroscopy in 3d transition metal complexes—electronic and structural information. *Coord. Chem. Rev.* **249,** 65–95 (2005).
8. Takeuchi, M. *et al.* Photocatalytic decomposition of NO under visible light irradiation on the Cr-ion-implanted TiO2 thin film photocatalyst. *Catal. Lett.* **67,** 135–137 (2000).
9. Bak, T., Nowotny, J., Rekas, M. & Sorrell, C. C. Photo-electrochemical hydrogen generation from water using solar energy. Materials-related aspects. *Int. J. Hydrog. Energy* **27,** 991–1022 (2002).
10. Patel, N. *et al.* Efficient Photocatalytic Degradation of Organic Water Pollutants Using V–N-Codoped TiO2 Thin Films. *Appl. Catal. B Environ.* **150–151,** 74–81 (2014).
11. *X-Ray Absorption Spectroscopy of Semiconductors | Claudia S. Schnohr | Springer*.
12. Lytle, F. W., Sayers, D. E. & Stern, E. A. Extended X-Ray-Absorption Fine-Structure Technique. II. Experimental Practice and Selected Results. *Phys. Rev. B* **11,** 4825–4835 (1975).
13. Fornasini, P. Introduction to X-Ray Absoprtion Spectroscopy. in *Synchrotron Radiation* (Springer, 2015).
14. Zabinsky, S. I., Rehr, J. J., Ankudinov, A., Albers, R. C. & Eller, M. J. Multiple-Scattering Calculations of X-Ray-Absorption Spectra. *Phys. Rev. B* **52,** 2995–3009 (1995).
15. Filipponi, A., Di Cicco, A. & Natoli, C. R. X-Ray-Absorption Spectroscopy and *n*-Body Distribution Functions in Condensed Matter. I. Theory. *Phys. Rev. B* **52,** 15122–15134 (1995).
16. Filipponi, A. & Di Cicco, A. X-Ray-Absorption Spectroscopy and *n*-Body Distribution Functions in Condensed Matter. II. Data Analysis and Applications. *Phys. Rev. B* **52,** 15135–15149 (1995).
17. Boland, J. J., Crane, S. E. & Baldeschwieler, J. D. Theory of extended x-ray absorption fine structure: Single and multiple scattering formalisms. *J. Chem. Phys.* **77,** 142–153 (1982).
18. Wyckoff, R. W. G. *Crystal Structures.* **1,** (1960).
19. Wong, J., Lytle, F. W., Messmer, R. P. & Maylotte, D. H. K-Edge Absorption Spectra of Selected Vanadium Compounds. *Phys. Rev. B* **30,** 5596–5610 (1984).

20. Yamamoto, T. Assignment of Pre-Edge Peaks in K-Edge X-Ray Absorption Spectra of 3d Transition Metal Compounds: Electric Dipole or Quadrupole? *X-Ray Spectrom.* **37,** 572–584 (2008).
21. Benfatto, M. & Meneghini, C. A Close Look into the Low Energy Region of the XAS Spectra: The XANES Region. in *Synchrotron Radiation* (Springer, 2015).
22. Waychunas, G. A. Synchrotron Radiation XANES Spectroscopy of Ti in Minerals: Effects of Ti Bonding Distances, Ti Valence, and Site Geometry on Absorption Edge Structure. *Am. Mineral.* **72,** 89–101 (1987).
23. Benfatto, M., Della Longa, S. & Natoli, C. R. The MXAN Procedure: a New Method for Analysing the XANES Spectra of Metallo-proteins to Obtain Structural Quantitative Information. *J. Synchrotron Radiat.* **10,** 51–57 (2003).
24. Bunău, O. & Joly, Y. Self-Consistent Aspects of X-Ray Absorption Calculations. *J. Phys. Condens. Matter* **21,** 345501 (2009).
25. Gougoussis, C., Calandra, M., Seitsonen, A. P. & Mauri, F. First-principles calculations of x-ray absorption in a scheme based on ultrasoft pseudopotentials: From α to high-T_c compounds. *Phys. Rev. B* **80,** 075102 (2009).
26. Ravel, B. & Newville, M. ATHENA, ARTEMIS, HEPHAESTUS: data analysis for X-ray absorption spectroscopy using IFEFFIT. *J. Synchrotron Radiat.* **12,** 537–541 (2005).
27. Newville, M. & IUCr. IFEFFIT : interactive XAFS analysis and FEFF fitting. *Journal of Synchrotron Radiation* (2001). Available at: http://scripts.iucr.org/cgi-bin/paper?ph5149. (Accessed: 9th March 2017)
28. Guda, A. A. *et al.* Finite difference method accelerated with sparse solvers for structural analysis of the metal-organic complexes. *J. Phys. Conf. Ser.* **712,** 012004 (2016).
29. Haskel, D. Local Structural Studies of Oriented High Temperature Superconducting Cuprates by Polarized XAFS Spectroscopy. (University of Washington, 1998).
30. Poiarkova, A. V. & Rehr, J. J. Multiple-Scattering X-Ray-Absorption Fine-Structure Debye-Waller Factor Calculations. *Phys. Rev. B* **59,** 948–957 (1999).
31. Kravtsova, A. N., Soldatov, A. V., Nachtegaal, M., Tew, M. W. & van Bokhoven, J. A. Influence of the muffin-tin approximation on the simulation of titanium K-edge X-ray absorption spectra of TiO2 (rutile and anatase phases). *Phys. B Condens. Matter* **405,** 724–726 (2010).
32. Joly, Y. X-ray absorption near-edge structure calculations beyond the muffin-tin approximation. *Phys. Rev. B* **63,** 125120 (2001).
33. Kotani, A. & Shin, S. Resonant inelastic x-ray scattering spectra for electrons in solids. *Rev. Mod. Phys.* **73,** 203–246 (2001).
34. Amidani, L. *et al.* Probing Long-Lived Plasmonic-Generated Charges in TiO2/Au by High-Resolution X-Ray Absorption Spectroscopy. *Angew. Chem. Int. Ed.* **54,** 5413–5416 (2015).
35. Glatzel, P., Sikora, M. & Fernández-García, M. Resonant X-ray Spectroscopy to Study K Absorption Pre-Edges in 3d Transition Metal Compounds. *Eur. Phys. J. Spec. Top.* **169,** 207–214 (2009).
36. Cabaret, D., Joly, Y., Renevier, H., Natoli, C. R. & IUCr. Pre-edge structure analysis of Ti K-edge polarized X-ray absorption spectra in TiO2 by full-potential XANES calculations. *Journal of Synchrotron Radiation* (1999). Available at: http://scripts.iucr.org/cgi-bin/paper?S0909049599000783. (Accessed: 9th June 2017)
37. Goulielmakis, E. *et al.* Real-time observation of valence electron motion. *Nature* **466,** 739–743 (2010).
38. Giannozzi, P. *et al.* QUANTUM ESPRESSO: a modular and open-source software project for quantum simulations of materials. *J. Phys. Condens. Matter* **21,** 395502 (2009).
39. Gonze, X. *et al.* ABINIT: First-principles approach to material and nanosystem properties. *Comput. Phys. Commun.* **180,** 2582–2615 (2009).

40. Kresse, G. & Furthmüller, J. Efficient iterative schemes for ab initio total-energy calculations using a plane-wave basis set. *Phys. Rev. B* **54,** 11169–11186 (1996).
41. Eschrig, H. *The Fundamentals of Density Functional Theory*. **32,** (Vieweg+Teubner Verlag, 1996).
42. Hohenberg, P. & Kohn, W. Inhomogeneous Electron Gas. *Phys. Rev.* **136,** B864–B871 (1964).
43. Kohn, W. & Sham, L. J. Self-Consistent Equations Including Exchange and Correlation Effects. *Phys. Rev.* **140,** A1133–A1138 (1965).
44. Perdew, J. P., Burke, K. & Ernzerhof, M. Generalized Gradient Approximation Made Simple. *Phys. Rev. Lett.* **77,** 3865–3868 (1996).
45. Lee, C., Yang, W. & Parr, R. G. Development of the Colle-Salvetti correlation-energy formula into a functional of the electron density. *Phys. Rev. B* **37,** 785–789 (1988).
46. Broyden, C. G. The Convergence of a Class of Double-rank Minimization Algorithms 1. General Considerations. *IMA J. Appl. Math.* **6,** 76–90 (1970).
47. Goldfarb, D. A family of variable-metric methods derived by variational means. *Math. Comput.* **24,** 23–26 (1970).
48. Fletcher, R. A new approach to variable metric algorithms. *Comput. J.* **13,** 317–322 (1970).
49. Shanno, D. F. Conditioning of quasi-Newton methods for function minimization. *Math. Comput.* **24,** 647–656 (1970).
50. Shanno, D. F. & Kettler, P. C. Optimal conditioning of quasi-Newton methods. *Math. Comput.* **24,** 657–664 (1970).
51. Fujishima, A., Zhang, X. & Tryk, D. A. TiO2 Photocatalysis and Related Surface Phenomena. *Surf. Sci. Rep.* **63,** 515–582 (2008).
52. Schultz, M. G., Diehl, T., Brasseur, G. P. & Zittel, W. Air Pollution and Climate-Forcing Impacts of a Global Hydrogen Economy. *Science* **302,** 624–627 (2003).
53. Kelly, N. A., Gibson, T. L., Cai, M., Spearot, J. A. & Ouwerkerk, D. B. Development of a renewable hydrogen economy: Optimization of existing technologies. *Int. J. Hydrog. Energy* **35,** 892–899 (2010).
54. Dresselhaus, M. S. & Thomas, I. L. Alternative energy technologies. *Nat. Lond.* **414,** 332–7 (2001).
55. Su, S. *et al.* Temporal trend and source apportionment of water pollution in different functional zones of Qiantang River, China. *Water Res.* **45,** 1781–1795 (2011).
56. Karn, S. K. & Harada, H. Surface Water Pollution in Three Urban Territories of Nepal, India, and Bangladesh. *Environ. Manage.* **28,** 483–496 (2001).
57. Shao, M., Tang, X., Zhang, Y. & Li, W. City clusters in China: air and surface water pollution. *Front. Ecol. Environ.* **4,** 353–361 (2006).
58. Acar, C. & Dincer, I. Comparative assessment of hydrogen production methods from renewable and non-renewable sources. *Int. J. Hydrog. Energy* **39,** 1–12 (2014).
59. Hashimoto, K., Irie, H. & Fujishima, A. TiO2 Photocatalysis: A Historical Overview and Future Prospects. *Jpn. J. Appl. Phys.* **44,** 8269 (2005).
60. Jaiswal, R., Patel, N., Kothari, D. C. & Miotello, A. Improved Visible Light Photocatalytic Activity of TiO2 Co-Doped with Vanadium and Nitrogen. *Appl. Catal. B Environ.* **126,** 47–54 (2012).
61. Nagaveni, K., Hegde, M. S. & Madras, G. Structure and Photocatalytic Activity of Ti1-xMxO2±δ (M = W, V, Ce, Zr, Fe, and Cu) Synthesized by Solution Combustion Method. *J. Phys. Chem. B* **108,** 20204–20212 (2004).
62. Umebayashi, T., Yamaki, T., Itoh, H. & Asai, K. Analysis of Electronic Structures of 3d Transition Metal-Doped TiO2 Based on Band Calculations. *J. Phys. Chem. Solids* **63,** 1909–1920 (2002).

63. Asahi, R., Morikawa, T., Ohwaki, T., Aoki, K. & Taga, Y. Visible-Light Photocatalysis in Nitrogen-Doped Titanium Oxides. *Science* **293,** 269–271 (2001).
64. Ohsaka, T. Temperature Dependence of the Raman Spectrum in Anatase TiO2. *J. Phys. Soc. Jpn.* **48,** 1661–1668 (1980).
65. Choi, H. C., Jung, Y. M. & Kim, S. B. Size Effects in the Raman Spectra of TiO2 Nanoparticles. *Vib. Spectrosc.* **37,** 33–38 (2005).
66. BM23 - XAS beamline. Available at: http://www.esrf.eu/UsersAndScience/Experiments/MEx/BM23. (Accessed: 4th December 2015)
67. ID26 - High-Brilliance X-ray Spectroscopy. Available at: http://www.esrf.eu/UsersAndScience/Experiments/EMD/ID26. (Accessed: 2nd September 2016)
68. Elettra Sincrotrone Trieste. Available at: http://www.elettra.eu/elettra-beamlines/bach.html. (Accessed: 4th December 2015)
69. Elettra Sincrotrone Trieste. Available at: https://www.elettra.trieste.it/it/lightsources/elettra/elettra-beamlines/bear/bear.html. (Accessed: 16th February 2017)
70. Ravel, B. & Newville, M. *ATHENA* , *ARTEMIS* , *HEPHAESTUS* : Data Analysis for X-Ray Absorption Spectroscopy Using *IFEFFIT*. *J. Synchrotron Radiat.* **12,** 537–541 (2005).
71. Rittmann-Frank, M. H. *et al.* Mapping of the Photoinduced Electron Traps in TiO2 by Picosecond X-Ray Absorption Spectroscopy. *Angew. Chem. Int. Ed.* **53,** 5858–5862 (2014).
72. Giannozzi, P. *et al.* QUANTUM ESPRESSO: a Modular and Open-Source Software Project for Quantum Simulations of Materials. *J. Phys. Condens. Matter* **21,** 395502 (2009).
73. Berti, M. *et al.* Formation and Dissolution of D-N Complexes in Dilute Nitrides. *Phys. Rev. B* **76,** 205323 (2007).
74. Ciatto, G. *et al.* Local Structure of Nitrogen-Hydrogen Complexes in Dilute Nitrides. *Phys. Rev. B* **79,** 165205 (2009).
75. Katsikini, M., Boscherini, F. & Paloura, E. C. Local Bonding Geometry of Oxygen Implanted in GaN: A Depth-Dependent Study. *J. Nanosci. Nanotechnol.* **10,** 6260–6265 (2010).
76. Boscherini, F., D'Acapito, F., Galata, S. F., Tsoutsou, D. & Dimoulas, A. Atomic Scale Mechanism for the Ge-Induced Stabilization of the Tetragonal, Very High-κ, Phase of ZrO2. *Appl. Phys. Lett.* **99,** 121909 (2011).
77. d'Acapito, F. Advanced Methods for the Analysis of X-Ray Absorption Spectroscopy Data Applied to Semiconductors. *Semicond. Sci. Technol.* **26,** 064004 (2011).
78. Amidani, L. *et al.* X-ray Absorption Spectra of $In_xGa_{1-x}N$ Alloys with Insight from Atom-Specific Simulations. *Phys. Rev. B* **86,** 155211 (2012).
79. De Luca, M. *et al.* Identification of Four-Hydrogen Complexes in In-Rich $In_xGa_{1-x}N$ (x>0.4) Alloys Using Photoluminescence, X-Ray Absorption, and Density Functional Theory. *Phys. Rev. B* **86,** 201202 (2012).
80. Amidani, L. *et al.* Connections Between Local and Macroscopic Properties in Solids: The Case of N in III-V-N Alloys. *Phys. Rev. B* **89,** 085301 (2014).
81. Kohlmeyer, A. O.pbe-van_ak.UPF. Available at: http://www.quantum-espresso.org/wp-content/uploads/upf_files/O.pbe-van_ak.UPF. (Accessed: 14th January 2016)
82. Kohlmeyer, A. Ti.pbe-sp_van_ak.UPF. Available at: http://www.quantum-espresso.org/pseudo/1.3/UPF/Ti.pbe-sp-van_ak.UPF. (Accessed: 14th January 2016)
83. Seng Wu, H. V.pbe-sp-van.UPF. Available at: http://www.quantum-espresso.org/wp-content/uploads/upf_files/V.pbe-sp-van.UPF. (Accessed: 14th January 2016)
84. Vanderbilt, D. Soft self-consistent pseudopotentials in a generalized eigenvalue formalism. *Phys. Rev. B* **41,** 7892–7895 (1990).

85. Perdew, J. P., Burke, K. & Ernzerhof, M. Generalized Gradient Approximation Made Simple. *Phys. Rev. Lett.* **77,** 3865–3868 (1996).
86. Avriel, M. *Nonlinear Programming: Analysis and Methods*. (2003).
87. Broyden, C. G. The Convergence of a Class of Double-rank Minimization Algorithms 1. General Considerations. *IMA J. Appl. Math.* **6,** 76–90 (1970).
88. PWscf User's Guide. Available at: http://www.quantum-espresso.org/wp-content/uploads/Doc/pw_user_guide.pdf.
89. Harris, J. Simplified Method for Calculating the Energy of Weakly Interacting Fragments. *Phys. Rev. B* **31,** 1770–1779 (1985).
90. Di Valentin, C. *et al.* N-doped TiO2: Theory and Experiment. *Chem. Phys.* **339,** 44–56 (2007).
91. Kucheyev, S. O. *et al.* Electronic Structure of Titania Aerogels from Soft X-Ray Absorption Spectroscopy. *Phys. Rev. B* **69,** 245102 (2004).
92. Hanley, T. L., Luca, V., Pickering, I. & Howe, R. F. Structure of Titania Sol−Gel Films: A Study by X-Ray Absorption Spectroscopy. *J. Phys. Chem. B* **106,** 1153–1160 (2002).
93. Luca, V., Djajanti, S. & Howe, R. F. Structural and Electronic Properties of Sol−Gel Titanium Oxides Studied by X-ray Absorption Spectroscopy. *J. Phys. Chem. B* **102,** 10650–10657 (1998).
94. Luca, V. Comparison of Size-Dependent Structural and Electronic Properties of Anatase and Rutile Nanoparticles. *J. Phys. Chem. C* **113,** 6367–6380 (2009).
95. Marchiori, C. *et al.* Unraveling the Cooperative Mechanism of Visible-Light Absorption in Bulk N,Nb Codoped TiO2 Powders of Nanomaterials. *J. Phys. Chem. C* **118,** 24152–24164 (2014).
96. Chen, L. X., Rajh, T., Wang, Z. & Thurnauer, M. C. XAFS Studies of Surface Structures of TiO2 Nanoparticles and Photocatalytic Reduction of Metal Ions. *J. Phys. Chem. B* **101,** 10688–10697 (1997).
97. Wu, Z. Y., Ouvrard, G., Gressier, P. & Natoli, C. R. Ti and O K edges for titanium oxides by multiple scattering calculations: Comparison to XAS and EELS spectra. *Phys. Rev. B* **55,** 10382–10391 (1997).
98. Mizoguchi, T. *et al.* Valence state of Ti in conductive nanowires in sapphire. *Phys. Rev. B* **70,** 153101 (2004).
99. Osorio-Guillén, J., Lany, S. & Zunger, A. Atomic Control of Conductivity Versus Ferromagnetism in Wide-Gap Oxides Via Selective Doping: V, Nb, Ta in Anatase TiO_2. *Phys. Rev. Lett.* **100,** 036601 (2008).
100. Kubacka, A., Fuerte, A., Martínez-Arias, A. & Fernández-García, M. Nanosized Ti−V Mixed Oxides: Effect of Doping Level in the Photo-Catalytic Degradation of Toluene Using Sunlight-Type Excitation. *Appl. Catal. B Environ.* **74,** 26–33 (2007).
101. Enhancement of room temperature ferromagnetism in N-doped TiO2−x rutile: Correlation with the local electronic properties. *Appl. Phys. Lett.* **97,** 012506 (2010).
102. El Koura, Z., Patel, N., Edla, R. & Miotello, A. Multilayer Films of Indium Tin Oxide/TiO 2 Codoped with Vanadium and Nitrogen for Efficient Photocatalytic Water Splitting. *Int. J. Nanotechnol.* **11,** 1017–1027 (2014).
103. Asahi, R. & Morikawa, T. Nitrogen complex species and its chemical nature in TiO2 for visible-light sensitized photocatalysis. *Chem. Phys.* **339,** 57–63 (2007).
104. Esaka, F. *et al.* Comparison of surface oxidation of titanium nitride and chromium nitride films studied by x-ray absorption and photoelectron spectroscopy. *J. Vac. Sci. Technol. Vac. Surf. Films* **15,** 2521–2528 (1997).
105. Nambu, A. *et al.* N doping of TiO2(110): Photoemission and density-functional studies. *J. Chem. Phys.* **125,** 094706 (2006).

106. Chen, H. *et al.* Reaction of NH3 with Titania: N-Doping of the Oxide and TiN Formation. *J. Phys. Chem. C* **111,** 1366–1372 (2007).
107. Fons, P. *et al.* Direct Observation of Nitrogen Location in Molecular Beam Epitaxy Grown Nitrogen-Doped ZnO. *Phys. Rev. Lett.* **96,** 045504 (2006).
108. Nobbs, J. H. Kubelka—Munk Theory and the Prediction of Reflectance. *Rev. Prog. Color. Relat. Top.* **15,** 66–75 (1985).
109. Tian, B. *et al.* Flame sprayed V-doped TiO2 nanoparticles with enhanced photocatalytic activity under visible light irradiation. *Chem. Eng. J.* **151,** 220–227 (2009).
110. Das, P. K., Mallik, A. K., Ganguly, R. & Santra, A. K. Synthesis and characterization of TiO2-water nanofluids with different surfactants. *Int. Commun. Heat Mass Transf.* **75,** 341–348 (2016).
111. Serpone, N., Lawless, D., Khairutdinov, R. & Pelizzetti, E. SUBNANOSECOND RELAXATION DYNAMICS IN TIO2 COLLOIDAL SOLS (PARTICLE SIZES RP=1.2-13.4 NM). RELEVANCE TO HETEROGENEOUS PHOTOCATALYSIS. *J. Phys. Chem.* **99,** 16655–16661 (1995).
112. Yoshihara, T. *et al.* Identification of Reactive Species in Photoexcited Nanocrystalline TiO2 Films by Wide-Wavelength-Range (400−2500 nm) Transient Absorption Spectroscopy. *J. Phys. Chem. B* **108,** 3817–3823 (2004).
113. Tamaki, Y. *et al.* Dynamics of Efficient Electron–Hole Separation in TiO2 Nanoparticles Revealed by Femtosecond Transient Absorption Spectroscopy Under the Weak-Excitation Condition. *Phys. Chem. Chem. Phys.* **9,** 1453–1460 (2007).
114. Bahnemann, D., Henglein, A., Lilie, J. & Spanhel, L. Flash photolysis observation of the absorption spectra of trapped positive holes and electrons in colloidal TiO2. *J. Phys. Chem.* **88,** 709–711 (1984).
115. Rothenberger, G., Moser, J., Graetzel, M., Serpone, N. & Sharma, D. K. Charge carrier trapping and recombination dynamics in small semiconductor particles. *J. Am. Chem. Soc.* **107,** 8054–9 (1985).
116. Linsebigler, A., Lu, G. & Yates, J. Photocatalysis on TiO2 Surfaces: Principles, Mechanisms, and Selected Results. *Chem. Rev.* **95,** 735–758 (1995).
117. Berger, T. *et al.* Light-Induced Charge Separation in Anatase TiO2 Particles. *J. Phys. Chem. B* **109,** 6061–6068 (2005).
118. Howe, R. F. & Gratzel, M. EPR observation of trapped electrons in colloidal titanium dioxide. *J. Phys. Chem.* **89,** 4495–9 (1985).
119. Sun, J. *et al.* Ultrafast carrier trapping of a metal-doped titanium dioxide semiconductor revealed by femtosecond transient absorption spectroscopy. *ACS Appl. Mater. Interfaces* **6,** 10022–10027 (2014).
120. Choi, W., Termin, A. & Hoffmann, M. R. The Role of Metal Ion Dopants in Quantum-Sized TiO2: Correlation between Photoreactivity and Charge Carrier Recombination Dynamics. *J. Phys. Chem.* **98,** 13669–13679 (1994).
121. Yoshihara, T. *et al.* Identification of Reactive Species in Photoexcited Nanocrystalline TiO2 Films by Wide-Wavelength-Range (400−2500 nm) Transient Absorption Spectroscopy. *J. Phys. Chem. B* **108,** 3817–3823 (2004).
122. Tamaki, Y. *et al.* Dynamics of Efficient Electron–Hole Separation in TiO2 Nanoparticles Revealed by Femtosecond Transient Absorption Spectroscopy Under the Weak-Excitation Condition. *Phys. Chem. Chem. Phys.* **9,** 1453–1460 (2007).
123. Lutterotti, L., Bortolotti, M., Ischia, G., Lonardelli, I. & Wenk, H.-R. Rietveld texture analysis from diffraction images. *Z. Krist. Suppl.* **2007,** 125–130 (2007).

124. Glatzel, P. & Bergmann, U. High resolution 1s core hole X-ray spectroscopy in 3d transition metal complexes—electronic and structural information. *Coord. Chem. Rev.* **249,** 65–95 (2005).
125. Solé, V. A., Papillon, E., Cotte, M., Walter, P. & Susini, J. A multiplatform code for the analysis of energy-dispersive X-ray fluorescence spectra. *Spectrochim. Acta Part B At. Spectrosc.* **62,** 63–68 (2007).
126. Press, W. H., Teukolsky, S. A., Vetterling, W. T. & Flannery, B. P. Chapter 15.2. in *Numerical Recipes in C* (Cambridge University Press, 2002).